Novel aspects in the crystallization of polybutene-1

By

Wei Wang

Tutor: Prof. Dario Cavallo

University of Genova

Doctoral School in Science and Technology of

Chemistry and Materials

(*XXXIV cycle*)

Contents

Chapter 1. Summary and outline

1.1 Summary

Semicrystalline polymers cover over two thirds of commercially produced polymeric materials, and have been widely applied to many areas of the modern society, including building and construction, electronics, packaging, etc. Understanding the behavior of polymer crystallization is of critical importance due to the significant impact of the crystallization process on the properties of materials. Polymorphism is the ability of a polymer, in analogy with low molecular mass substances, to crystallize in different modifications, characterized by different crystal structures (polymorphic forms). Much effort has been made to find proper methods to develop different crystal modifications for polymorphic polymers. However, it is still a challenge to control the polymorphic outcome of the crystallization process. Furthermore, semicrystalline polymers are composed of stacked crystalline lamellae and entangled amorphous polymeric chain segments in between them. The interaction between amorphous and crystalline phases plays an important role in determining final mechanical and transport properties. Despite this importance, the effect of polymorphism on the amorphous phase is not well clarified because of its complexity. In this thesis, one typical polymorphic polymer, polybutene-1 (PB-1), was selected for a detailed crystallization study.

Polybutene-1 is one of the most investigated polymorphic polymers. It has applications in pipes and films with a service life up to 50-100 years due to its excellent mechanical properties. In practice, among all crystalline polymorphisms within PB-1, Forms I and II are the most relevant modifications from the processing perspective. With the goal to establish a comprehensive understanding of the heterogeneous nucleation between these two modifications (cross-nucleation), we monitor the crystallization process of Form II induced by Form I crystals with different type of substrate (spherulitic, hedritic and fiber-like) using a direct investigation technique of optical microscopy. The different cross-nucleation efficiencies of Form II are tentatively attributed to differences in the Form I lamellar thickness, on the basis of an epitaxial crystallization and heterogeneous nucleation mechanism. A quantitative analysis of the induction time for nucleation determined the cross-nucleation energy barrier, which could be reasonably described by classical models. The results revealed that the rate determining step for PB-1 cross-nucleation is the process of the addition of several crystalline layers during the formation of critical nucleus. Furthermore, the hypothesized epitaxy in PB-1

Form II-on-Form I cross-nucleation is probed by employing in-situ nanofocused synchrotron X-ray diffraction. Comparing the two-dimensional diffraction patterns at the interface between the two modifications, a preferred mutual orientation of the two structure, with the $(200)_{II}$ plane aligned ~8.5º apart from the $(110)_{I}$ plane, is revealed. This demonstrates a parallel (110) plane between the two polymorphs during cross-nucleation. Then, both mismatches between the inter-chain distances and along the chain axes within (110) plane were considered and found to lay well-below the accepted mismatch criterium for epitaxy. This confirms that the cross-nucleation of Form II on Form I occurs at the (110) contact planes through epitaxial mechanism.

Next, an in-depth study of fiber-induced nucleation ability and crystalline morphology in polybutene-1/fiber composites is presented. Using different fibers as substrates, we could unveil the difference of Form II crystalline morphology: a transcrystalline layer (TCL) induced by PB-1 Form I fiber and hybrid shish–calabash structure (HSC) induced by other fibers, namely carbon, glass, PP, PLLA homocrystal and stereocomplex. Based on a quantitative analysis of the nucleation kinetics, it was found that the nucleation free energy barrier is affected by surface roughness, surface chemistry and specific surface-polymer interactions (epitaxy). In view of the number of potential nucleation sites correlating with the fiber surface roughness, it was demonstrated that TCL can be obtained when a sufficient amount of nucleation sites is available, notwithstanding the height of the nucleation free energy barrier.

Besides the phenomenon of heterogeneous nucleation, the three-phase structure is also influenced by crystal polymorphism. Therefore, in the last part of the thesis, we focused on the study of the rigid amorphous fraction (RAF) in both polymorphs, i.e., the part of amorphous chains constrained by direct coupling to the crystalline lamellae. Isochronous aging experiments with differential scanning calorimetry (DSC) on both crystalline phases are performed, in a wide temperature range between the glass transition of the mobile amorphous fraction and the onset of crystal melting. An endothermic peak above the aging temperature is typically observed. The trend of the recovered enthalpy calculated from the endothermic peak with temperature can be described by a bell-shaped curve, approaching zero recovered enthalpy at temperatures of 100-110 °C, and 40-50 °C for samples with Form I and Form II, respectively. These temperatures are thus identified as the upper limit of the glass transition of rigid amorphous fraction coupled with the two modifications. Overall, our results demonstrate that for PB-1, at least within the investigated temperature range, the endothermic peaks can be related to structural recovery of the RAF.

1.2 Outline

The aim of this thesis is to gain a deeper understanding on several issues related to crystallization of polybutene-1, which include cross-nucleation, fiber induced heterogeneous nucleation, and the rigid amorphous fraction. In particular, by means of differential scanning calorimetry (DSC), polarized light optical microscope (PLOM), and nanofocused synchrotron wide angle X-ray scattering (WAXS) techniques, we investigated the heterogeneous nucleation and the enthalpy relaxation of RAF.

The second chapter describes some general concepts on crystallization and rigid amorphous fraction. A brief introduction on polybutene-1 is also given.

The third chapter describes in detail the experimental materials and techniques that were used throughout this thesis to perform the measurements.

In the fourth chapter, the substrate-induced cross-nucleation behavior of PB-1 using seeds of Form I but possessing a different morphology (spherulitic, hedritic or fiber-like) is monitored. The mechanism for the differences in nucleation kinetics of different substrates toward Form II is discussed. The quantitative analysis of the induction time for nucleation is also proposed in combination with different models.

The fifth chapter explores the possible existence of epitaxy between Forms I and II modifications in PB-1 cross-nucleation by nanofocused synchrotron X-ray diffraction. The two-dimensional diffraction patterns at the interface of Form II-on-Form I cross-nucleation are analyzed. The calculations of mismatches along various crystallographic directions are presented, to prove validity of the epitaxial crystallization mechanism of Form II on Form I crystals.

The sixth chapter focuses on discussing fiber-induced nucleation ability and crystalline morphology in polybutene-1/fiber composites. The effect of fiber characteristics on heterogeneous nucleation kinetics are discussed. The density of nucleation sites along the fiber has been highlighted to distinguish the crystalline morphology of Form II on fibers.

The seventh chapter is dedicated to the influence of crystal polymorphism on the three-phase structure of PB-1, detected by calorimetry using the method of isochronous aging experiments. The influence of crystal modification of PB-1 on thermal properties of the RAF is explored. The nature of endothermic peak in aged PB-1 has been disclosed by using a multiple approach.

In the final chapter, a general conclusion of the work, together with possible outlooks, are provided.

Chapter 2. General introduction

2.1 The phenomenon of polymer crystallization

Polymer crystallization is a challenging subject of academic research that is very important for the plastics industry, as approximately 75% of all commercially available polymers are semicrystalline and their properties depend on their crystallinity degrees, melting temperatures and semicrystalline morphology. Polymer crystallization has been the subject of many important books and reviews over its 60 years history. [1-20]

The polymer can only partially crystallize when it is cooled below the equilibrium melting point, forming a two-phase structure with alternating crystalline and amorphous phases. This can be attributed to the presence of a large number of chain entanglements in the polymer melt, most of which cannot be disentangled and eliminated in the time given by the crystallization process and can only migrate to the amorphous zone, due to the low diffusion coefficients and high viscosities typical of long molecular chains' melts. The complicated morphologies which arise is organized in a hierarchical structure. During crystallization, the disordered polymer chains first form a stable conformation, conformationally ordered chain segments then arrange parallel to each other to form the smallest repeating unit of a unit cell at the 10^{-1}-10^{0} nm length scale, and further form crystalline lamella with folded chains at the 10^{1}-10^{2} nm length scale. Finally, the lamellae are used as structural units to further stack into micrometer or even larger scale spherical crystalline structures, that are spherulites, through isotropic arrangements, as shown in Figure 2.1.[13]

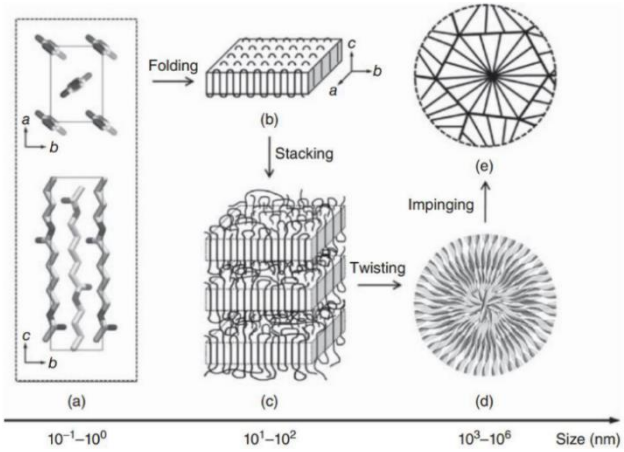

Figure 2.1 Scheme of the hierarchical structure of semicrystalline polymer. (a) aligned chains, (b) crystal lamella, (c) lamellar stacking morphology, and (d) spherulitic structure.[13]

The morphology of polymer crystals has been an important topic in polymer science for more than 60 years. While single crystals grown from solution show mono or multi-lamellar faceted shapes, polymer crystals obtained from the quiescent melt mainly display a spherulitic morphology, consisting of radically arranged folded chain lamellar stack structures. When polymers are crystallized under flows such as elongational and/or shear flows, the so-called shish-kebab structure is formed, which consists of long central fiber core (shish) surrounded by lamellar crystalline structure (kebab) periodically attached along the shish.[21-24] Embedded fibers or other solid surfaces in a polymer matrix may act as heterogeneous substrates and crystallization occurs along the interface with a high density of nuclei. These large number of nuclei will further hinder the lateral growth of each site, and force crystal growth in one direction, namely perpendicularly to the fiber nucleating surface, resulting in a columnar crystalline layer, known as transcrystallinity (TC) or transcrystalline layers (TCL).[25-29] Figure 2.2 shows micrographs of typical morphology of single crystal, spherulite, shish-kebab structure, and transcrystallinity.

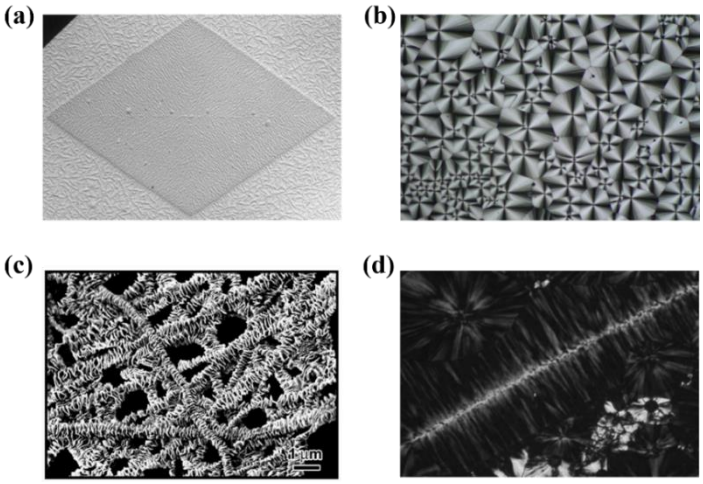

Figure 2.2 Micrograph of a typical morphology of (a) single crystal, (b) spherulite, (c) shish-kebab structure, and (d) transcrystallinity.

2.2 Theories of polymer crystallization

Polymer crystallization is a first order phase transition of the supercooled liquid, and in order for this thermodynamically favored transformation to occur, two separate processes are required, i.e., the stable phase has to nucleate and then grow within the metastable phase. Therefore, when isothermal crystallization happens slowly at high temperatures, one can observe a significantly long incubation period for crystal nucleation, followed by the process

of crystal growth.

2.2.1 Classical nucleation theory

Nucleation involves the attainment of a particular molecular chain arrangement in order to form the new phase. In the case of polymer crystallization from the melt, the chain segments must approach themselves to distances commensurate to those characteristics of the crystalline unit cell, and must possess the right conformation, as the crystal symmetry imposes. From a thermodynamic point of view, the chain segments with those attributes form a crystalline aggregate which varies the system free energy according to:

$$\Delta G = \Delta H - T\Delta S \tag{2.1}$$

where ΔH and ΔS are the enthalpy and entropy of crystallization respectively. The thermodynamic equilibrium condition between the melt and the crystals is verified when ΔG is equal to zero, i.e., when the temperature of the system is the melting temperature, T_m. Crystallization becomes possible as soon as ΔG assumes negative values.

Any crystal starts as a small crystal with a large specific surface area. Therefore, equation (2.1) can also be written by explicitly expressing the surface and volume contributions to the Gibbs free energy:

$$\Delta G = V\Delta g + \sum_i A_i \sigma_i \tag{2.2}$$

where V is the volume and A_i is the i-th surface of the aggregate, σ_i represents the (positive) surface free energy of the related surface, and Δg is the bulk free energy change per unit volume associated to the formation of a new crystal. At temperatures above T_m, crystallization is thermodynamically impossible, while below T_m it becomes possible, but its occurrence depends on the competition between these two energy terms. As such, the ΔG exhibits a maximum with respect to the crystalline aggregate size, as shown in Figure 2.3. The maximum in ΔG corresponds to the critical size that the aggregate must attain in order to become a nucleus. Clusters smaller than r^* are called subcritical nuclei or embryos, they are unstable and tend to disappear from the system, since their growth is linked to an increase of ΔG. Aggregates that exceed r^* are called supercritical nuclei as long as their ΔG is still positive: their growth to sizes exceeding the minimum stability requirement is thermodynamically favored. Nuclei with a negative ΔG are called stable nuclei or small crystals. The larger the critical nucleus size, the longer will be the time needed for the nucleation process.

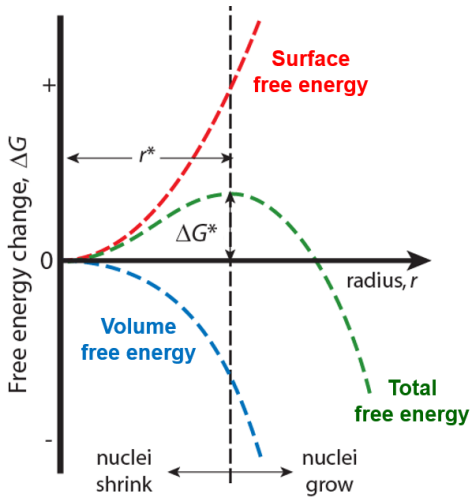

Figure 2.3 Schematic representation of the change in ΔG as a function of crystalline aggregate size, illustrating the nucleation process.

Various theories available to describe nucleation are based on phenomenological, kinetic, and microscopic approaches. The phenomenological models try to calculate the free energy formation of clusters based on macroscopic quantities. The kinetic theory of nucleation avoids the use of macroscopic surface tension; instead, it is based on molecular interactions.[30-32] Molecular approaches, which include Monte Carlo simulation and molecular dynamics (MD)[33-35] use first principles to calculate the free energy of cluster formation. The classical nucleation theory (CNT) is the first theoretical treatment based on a phenomenological approach to nucleation and dominated the field of nucleation studies for many years.

As the most common theoretical model, CNT is used to understand nucleation of a new thermodynamic phase such as a liquid or solid. The CNT stems from the work of Volmer and Weber, Becker and Döring, and Frenkel.[36, 37] It originally described the condensation of vapor to a liquid, under the assumption that fluctuations in the supercooled phase can overcome the nucleation barrier caused by the surface of the liquid. The theory can be extended to other equilibrium systems such as crystallization from melts and solutions. The probability of the presence of a nucleus of given size at constant volume and energy is, according to Boltzmann's law, a function of the change in entropy, proportional to $\exp(\Delta S/k)$. At constant pressure and temperature, the probability for the presence of a nucleus of given size is proportional to $\exp(-\Delta G/kT)$. The theory is approximate and gives reasonable prediction of nucleation rates, I^*:

$$I^* = (NkT/h)exp[-(\Delta G^* + \Delta U)/kT] \quad (2.3)$$

where h is Plank constant, N is the amount of uncrystallized units that can participate in the nucleation process, k is Boltzmann constant, ΔG^* is the critical free energy barrier for crystal

nucleation and ΔU is the activation energy for the diffusion of crystallizing elements across the phase boundary

Some of the simplifying assumptions of CNT are (a) the nucleus can be described with the same macroscopic properties (density, structure, composition) of the stable phase, (b) the nucleus is spherical and the interface between the nucleus and the solution is a sharp boundary, and (c) solid–liquid interface is approximated as planar, regardless of critical cluster size. This is known as capillary approximation and may be reasonable for large clusters, but for small clusters the surface is highly curved, and the approximation leads to large discrepancies. The assumption of spherical shape is also not generally valid, as for instance in the case of NaCl, which produces cubic-shaped nuclei. Also, if polymorphism is expected for a system, this may not necessarily nucleate in the stable form, but it can pass through a path by which the free energy barrier is minimized. This is not taken into account by CNT. Even though the theory is able to capture the underlying physics of the phenomenon and provide good qualitative interpretation of nucleation data, its failure to provide a correct quantitative description led to the unsuitability of CNT for a variety of systems. Another shortcoming of the theory is that it is unable to explain the vanishing nucleation barrier at high supercooling. In spite of various extensions and developments in theoretical approaches, CNT still serves as a platform to describe nucleation, since it is based on experimentally accessible information.

2.2.2 Primary nucleation

Primary nucleation, the first step of crystallization, can include two types of nucleation: homogeneous and heterogeneous nucleation. Homogeneous nucleation [38, 39] is a significantly studied phenomenon that occurs, when a system initially in a state of stable thermal equilibrium, becomes metastable as a result of thermal fluctuations, and there is no role of foreign surfaces. This type of nucleation is the dominant mechanism in the formation of microcrystalline ceramics, explosions occurring when a cold fluid contacts a hotter fluid, condensation on supersonic nozzles, and many other systems.[40-42] Usually large supersaturations or supercoolings are needed to initiate this type of nucleation.

Instead, nuclei induced at the interface of vessel walls, dust particles, and impurities are considered examples of heterogeneous nucleation, [5, 9, 43-46] which can occur at a lower supersaturation (or supercooling) compared to homogeneous nucleation. A more specific example of heterogeneous nucleation is the case of cross-nucleation, where a faster growing polymorph can nucleate heterogeneously on the surface of another one, without requiring any phase transition between them.

With respect to the formation of the spherical nucleus with a radius of r during the homogeneous nucleation process, the Gibbs free energy change ΔG after the formation of the spherical nucleus is given by

$$\Delta G = -\frac{4}{3}\pi r^3 \Delta g + 4\pi r^2 \sigma \tag{2.4}$$

where Δg and σ are the bulk free energy difference and the surface free energy between the nucleus and surrounding liquid, respectively. The surface and volumetric terms as well as ΔG versus radius of the nucleus are schematically illustrated in Figure 2.3, where the volumetric and surface terms in equation (2.4) show opposite trends. The radius r^* of the critical nucleus can be obtained when $d\Delta G/dr = 0$:

$$r^* = \frac{2\sigma}{\Delta g} = \frac{2\sigma T_m}{\Delta h^o \Delta T} \tag{2.5}$$

where Δh^0 is the enthalpy of crystallization at the equilibrium melting point T_m and ΔT is the supercooling degree ($\Delta T = T_m - T$). The related value of the critical free energy variation, $\Delta G(r^*)$, the free energy of the critical nucleus, can be computed as:

$$\Delta G^* = \frac{16}{3}\pi \frac{\sigma^3}{\Delta g^2} = \frac{16}{3}\pi \frac{\sigma^3 T_m^2}{(\Delta h^o)^2 (\Delta T)^2} \tag{2.6}$$

In the case of polymers, we must consider a different geometry for the nucleating crystal, given the fact that this is built by the successive addition of adjacent segments of polymer chains. The simplest choice is that of a prismatic nucleus with quadratic cross section. For this geometry, and taking into account chain folding, we have to use two different surface free-energies: that of the bases (σ_e) and of the lateral surfaces (σ) of the parallelepiped. Then, the equation for the change in the free energy of crystallization becomes:

$$\Delta G = 4al\sigma + 2a^2\sigma_e - a^2 l \Delta g \tag{2.7}$$

where a and l are the cluster dimensions. In general, σ_e is 5 to 20 times the value of σ. Also, this function has a maximum (ΔG^*) in correspondence of the critical dimensions a^* and l^*:

$$a^* = \frac{4\sigma T_m}{\Delta T \Delta h^o} \tag{2.8}$$

$$l^* = \frac{4\sigma_e T_m}{\Delta T \Delta h^o} \tag{2.9}$$

$$\Delta G^* = \frac{32\sigma\sigma_e T_m^2}{(\Delta h^o)^2 (\Delta T)^2} \tag{2.10}$$

Building upon earlier work of Volmer,[47] an extension of CNT to heterogeneous nucleation was proposed by Turnbull.[48, 49] In Turnbull's model, the nucleating cluster is assumed to be a hemispherical cap intersecting the substrate surface with a contact angle θ (see Figure 2.4). The equation for the work required to form the nucleating cluster within CNT is

$$\Delta G_{het} = V(R,\theta)\Delta g + A_1(R,\theta)\left(\sigma_{s,sub} - \sigma_{l,sub}\right) + A_2(R,\theta)\sigma_{sl} \tag{2.11}$$

where $V(R, \theta)$ is the volume of the cap, $A_1(R, \theta)$ and $A_2(R, \theta)$ are the areas of the cap-liquid and cap-substrate boundaries, respectively. The quantities $\sigma_{s,sub}$ and $\sigma_{l,sub}$ are the crystal-substrate and liquid-substrate surface free energies, respectively. Therefore, the heterogeneous nucleation barrier within Turnbull's CNT can be expressed as a fraction of the homogeneous nucleation barrier, but the radius r* of the critical nucleus is the same of that of homogeneous nucleation,

$$\Delta G^*_{het} = \Delta G^* f(\theta) = \Delta G^* \frac{(2+\cos\theta)(1-\cos\theta)^2}{4} \tag{2.12}$$

$$r^*_{het} = r^* = \frac{2\sigma_{sl}}{\Delta g} \tag{2.13}$$

where ΔG^* and r^* are the energy barrier and critical size for the homogeneous nucleation case and $f(\theta)$ is the shape factor.

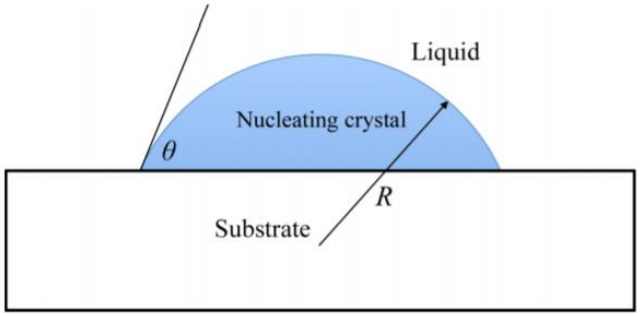

Figure 2.4 Hemispherical cap geometry for classical heterogeneous nucleation theory.

Another classical approach for polymers assumes the formation of prismatic embryos with rectangular cross section and height in the direction of the chain axis on a flat surface, as showed in Figure 2.5.

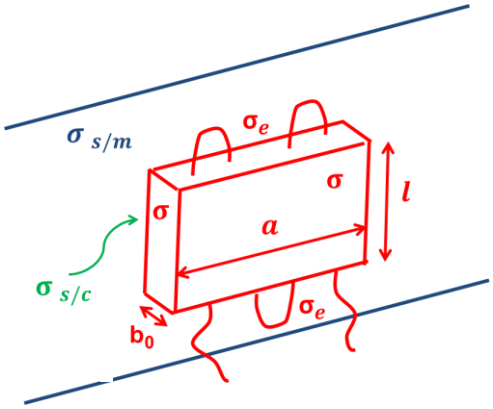

Figure 2.5 Prismatic geometry for classical heterogeneous nucleation theory. The blue lines represent the surface of the heterogeneous nucleus on which the embryo is formed.

The equation that describes this nucleation modality is simply a modification of the homogeneous nucleation case. The change in the Gibbs energy has the form:

$$\Delta G_{het} = -abl\Delta g + 2bl\sigma + al\Delta\sigma + 2ab\sigma_e \tag{2.14}$$

where σ is the free energy of the lateral surfaces in contact with the supercooled melt, σ_e is the free energy of the surfaces perpendicular to the chain direction and $\Delta\sigma$ is the interfacial free energy difference, given by:

$$\Delta\sigma = \sigma + \sigma_{s/c} - \sigma_{s/m} \tag{2.15}$$

In which $\sigma_{s/c}$ is the crystal-substrate interfacial energy and $\sigma_{s/m}$ is the melt-substrate interfacial energy. Therefore, $\Delta\sigma$ can be brought down to the surface tension properties of the substrate, polymer crystal and polymer melt. Thus, $\Delta\sigma$ is a convenient way to define the nucleating ability of the substrate toward the polymer melt. In fact, this parameter is related to the critical dimensions of the heterogeneous nucleus and the associated free energy barrier:

2.2.3 Crystal growth theory

In the last decades, polymer crystallization models have been investigated intensively since the discovery of the chain folding in polyethylene single crystal in 1957 by Till, Keller, and Fischer.[50-53] Up to now, the most successful and widely accepted theory to describe crystal growth was proposed by Hoffman and Lauritzen, now known as Hoffman–Lauritzen (HL) theory or the Lauritzen–Hoffman (LH) theory. This theory is based on the secondary nucleation at the lateral growth front of lamellar polymer crystals.[54-56] However, Sadler-Gilmer argued that the nucleation barrier is completely an “entropy barrier” without enthalpic contribution.[57, 58] Furthermore, other comprehensive approaches have been continuously

proposed to understand the polymer crystallization, such as the fine-grained model,[59] Point's multipath model,[60, 61] Sadler−Gilmer's model,[62] Hikosaka's sliding diffusion model,[63] Wunderlich's molecular nucleation model,[5] Hu's intramolecular nucleation model,[64] and Muthukumar's continuum model,[65] just to name a few.

As the polymer community is familiar with HL theory, we still want to highlight the key characteristics of this theory to be compared with the above theories. The HL theory is mainly based on the following assumptions: (1) the growth front is smooth; (2) the length of chain-folded crystal stems keeps constant during crystal growth. The energy barrier is gradually compensated by the free energy gain upon depositing neighbouring stems with a length slightly beyond a minimum lamellar thickness. The crystal grows in size involving two key processes: a molecular stem firstly lays down on the pre-existing surface provided by stable nuclei, secondly, other chain segments attach next to the first stem resulting in the lateral growth of the crystal, as shown in Figure 2.6.

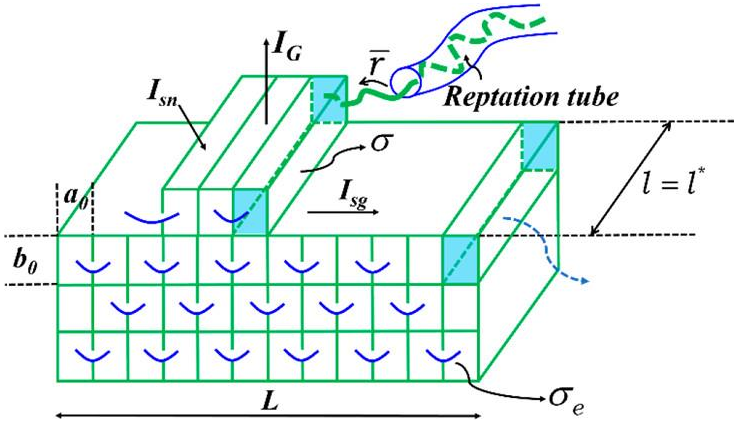

Figure 2.6 Model of secondary nucleation and growth proposed in the HL theory.[96]

HL theory describes the crystal growth by employing a surface nucleation rate I_{sn} and a substrate completion rate I_{sg}. During surface nucleation, the first chain stem, with length l corresponding to the thickness of the crystal substrate, deposits onto an atomically smooth growth front with a bulk energy gain of $a_0b_0l\Delta g$ and a penalty of $2b_0l\sigma$ due to the creation of two lateral surfaces, where a_0 and b_0 are the width and thickness of the stem, respectively, Δg is the free energy difference between crystal and polymer melt, and σ is the free energy of the lateral surface. The further deposition of other stems requires chains to fold back and forth with the same energy gain of $a_0b_0l\Delta g$ and a penalty of $2a_0b_0\sigma_e$ due to chain folding, with σ_e being the free energy of the folded-chain surface. This process eventually leads to the formation of

secondary nuclei on the surface with a nucleation rate of I_{sn}. Afterward, the rest of the growth front is covered by the following deposited polymer stems until it is fully covered with a substrate completion rate I_{sg}. Repeating this process leads to the growth of crystal layer by layer with a growth rate of G:

$$G = G_0 \exp\left(-\frac{U^*}{R(T - T_\infty)}\right) \exp\left(-\frac{K_g}{T\Delta T f}\right) \tag{2.16}$$

$$K_g = \frac{nb\sigma\sigma_e T_m}{\Delta h_f k_B} \tag{2.17}$$

where G_0 is the preexponential factor, U^* is the activation energy of the segmental jump, $\Delta T = T_m - T$ is the undercooling, $f = 2T/(T_m + T)$ is a correction factor, T_∞ is a hypothetical temperature where motion associated with viscous flow ceases and is usually taken 30 K below the glass transition temperature, T_g. K_g is the nucleation kinetics constant, b is the surface nucleus thickness, T_m is the equilibrium melting temperature, Δh_f is the heat of fusion per unit volume of crystal, k_B is the Boltzmann constant, and n takes the value 4 for crystallization regime I and III, and 2 for regime II.

2.3 Rigid amorphous fraction

Semicrystalline polymers have a metastable nanophase structure, which is determined by a competition among crystallization and vitrification. Early investigations of semicrystalline polymers based their description on a two-phase model, where the two phases, an amorphous and a crystalline one, have nanometer dimensions in one or more directions. More detailed analyses revealed that an intermediate fraction is present at the interface between the crystals and the surrounding amorphous phase. The intermediate fraction is non-crystalline, and includes portions of macromolecules whose mobility is hindered by the nearby crystalline structures. Thus, the amorphous parts can be subdivided into rigid amorphous fraction (RAF) and mobile amorphous fraction (MAF), depending on the degree of coupling with the crystal phase, which in turn affects chain mobility.[66] The MAF and RAF terms were first coined by Wunderlich while investigating the glass transition of poly(oxymethylene).[67] The mobile amorphous fraction is made of polymer chains that are decoupled from the crystals and mobilize at the glass transition temperature (T_g). The rigid amorphous fraction, instead, is highly coupled with the crystals, as it arises from the continuation of the partially crystallized macromolecules across the phase boundaries, being the polymer molecules much longer than the crystal nanophases.

A simplified and schematic representation of the arrangement of crystalline, rigid amorphous, and mobile amorphous fractions is shown in Figure 2.7. Crystalline domains made of ordered lamellae are surrounded by amorphous regions made of entangled chain segments. Amorphous and crystalline domains are connected by tie molecules, which link two nearby crystalline domains, and loose loops, which originate from the crystalline phase but protrude into the amorphous fraction. The RAF refers to the amorphous domains adjacent to the crystalline lamellae, where the covalent linkage of the crystalline and amorphous phases at the crystal surfaces results in a decrease in the number of micro-conformations that can be adopted by the amorphous segments, due to their progressive immobilization. The dimensions of the crystalline-amorphous transition layer, and the magnitude of immobilization of the amorphous phase, are controlled by the chain architecture, that is, by the inherent flexibility of the macromolecule, and by the structure of the crystal surfaces, which can be varied with thermal history.

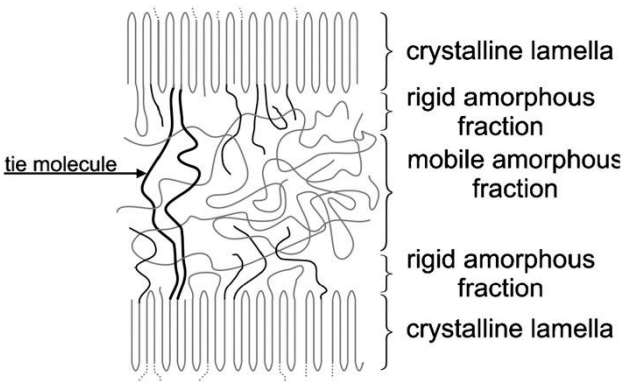

Figure 2.7 Schematic representation of the arrangement of crystalline, rigid amorphous, and mobile amorphous fractions.

The RAF has been discovered in almost all semicrystalline polymers,[66] as well as in a large array of interfacially-rich polymeric systems that exhibit alterations in dynamics and glass formation behavior.[68, 69] The rigid amorphous fraction has deep impact on properties of semicrystalline polymers, like mechanical response and gas permeability.[70-76] Considering that most large-volume commodity polymers are semicrystalline, improved understanding of the mechanism and rational control of the rigid amorphous fraction has the potential to yield enormous technological and economic benefits.

2.4 The crystallization behavior of polybutene-1

Polybutene-1 (PB-1) was first synthesized in 1954,[77] one year after polypropylene. It took another 10 years until Chemische Werke HÜLS, Germany, started the first industrial production in 1964 (capacity: ca. 3 kt/a). With the commercial name of Vestolen BT, it was introduced to the market soon afterward.

Polybutene exists in two isomeric forms depending on where the carbon-carbon double bond is positioned in the monomer molecule. If it is between the first and second carbon atoms in a linear molecule (butene-1), then the name of the resulting polymer is "polybutene-1" (PB-1). If it is a branched monomer molecule (i.e., the double bond is between the second and third carbon), then the resulting polymer is called polyisobutylene (PIB).

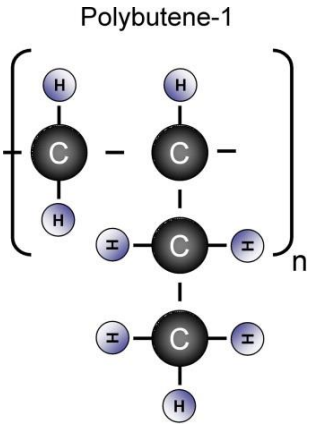

Figure 2.8 Polybutene-1 chemical structure.

The polymer we are concerned with is PB-1. In the past this polymer has been also referred to as polybutylene, PB, PB-1, and polybutene. PB-1 is obtained by polymerization of butene-1 with a stereo-specific Ziegler-Natta catalyst to create a linear, high molar mass, isotactic, semicrystalline polymer. PB-1 combines the typical properties of conventional polyolefins with some characteristics of technical polymers. In the chemical structure, PB-1 differs from polyethylene and polypropylene only by the number of carbon atoms in the monomer molecule (Figure 2.8).

PB-1 is a typical polymorphic semicrystalline polymer, which can form various helical conformations and pack into different types of unit cells depending on the solidification conditions. The known crystalline modifications are Forms I/I', II, and III, respectively.

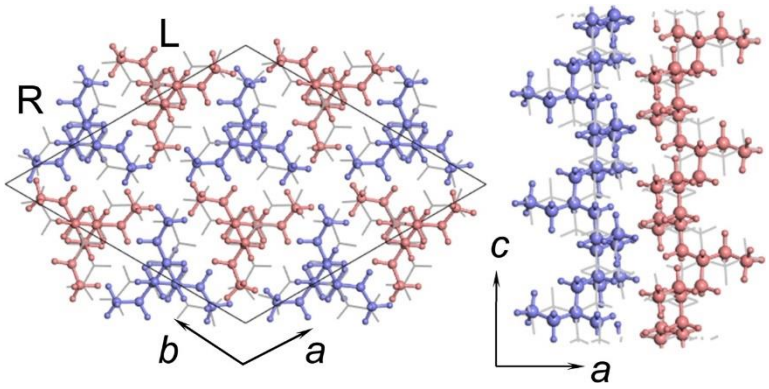

Figure 2.9 Crystal structure of PB-1 Form I.

The crystal structure of Form I is the stable crystal modification with the lowest free energy, exhibiting excellent mechanical properties over a wide temperature range between glass transition temperature and melting point, and it was analyzed by several research groups.[78-81] On the basis of the X-ray diffraction data, Natta et al. proposed a trigonal (hexagonal-type) unit cell in which the right-handed (3/1) helix (R) and the left-handed (3/1) helix (L) form a pair, and these pairs are packed together around the 3-fold rotation axis.[77] Two possibilities for the space group remained: *R3c* and $R\bar{3}c$. The number of monomeric units in the cell is 18, and the cell parameters are a = b = 17.7 Å, c = 6.5 Å. This has been continuously revised by later scholars. For example, recently Tashiro et al. used two-dimensional X-ray diffraction to measure a highly oriented sample of Form I and found that the molecular chains take the (3/1) helical conformation (see Figure 2.9). These chains were proposed to be packed in the trigonal unit cell with the parameters a = b = 17.53 Å and c = 6.48 Å in the space group $P\bar{3}$.[82] Form I' has the same crystal structure as Form I but it is obtained by direct crystallization from melt or solution and contains more defects. On the other hand, Form I is obtained by phase transition from the metastable Form II crystal. Hollland et al. found different diffraction patterns of Form I obtained by the two pathways, and concluded that the crystals obtained by phase transformation are a twinned form, while those obtained by direct crystallization are untwined.[83]

The crystal Form II is thermodynamically metastable and transforms spontaneously into the more stable crystal Form I when the sample is left at room temperature. Natta et al. analyzed the crystal structure of Form II for the first time and found a tetragonal structure with a 4/1 helical conformation of molecular chains, where the unit cell parameters are a = b = 7.49 Å and c = 6.85 Å. Further studies by Jones et al. revealed that the chain conformation of Form II is 11/3 helix in the tetragonal unit cell with parameters a = b = 14.85 Å and c = 20.6 Å.[84]

Recently, Tashiro et al. analysed the X-ray diffraction patterns of highly oriented Form II crystal at -140°C and found that the molecular chains take an (11/3) helical conformation and are packed in the tetragonal unit cell (a = b = 14.9 Å and c = 21.3 Å) within the space group $P\bar{4}b2$. The right-handed (or left-handed) chains are positioned at one site with statistical disorder of upward and downward directionality along the chain axis.[82]

The crystal Form III is mainly obtained from solution crystallization. Cojazzi et al first studied the crystal structure of Form III using debye-Scherrer powder diffraction. It was found that the molecular chains take the 4/1 helical conformation and are packed in an orthorhombic unit cell (space group $P2_12_12_1$) with parameters a = 12.38 ± 0.08 Å, b = 8.88 ± 0.06 Å and c = 7.56 ± 0.06 Å.[85]

In practice, among these structures, Forms I and II are the most processing-relevant modifications. The phase transition from Form II to Form I is completed in several days to weeks depending on the sample conditions and temperatures. This phase transition is also industrially important and many works on the topic were reported.[86-95] Once PB-1 sample is melted and made to a commercial product of a certain shape, the crystal Form II is crystallized at first in the product, as mentioned above. Since the unit cell size and shape between Forms I and II are different, a significantly large volume change or deformation of the product occurs after being stored at room temperature, as a consequence of the phase transition. In order to resolve such a practical problem, various solutions were proposed. One method is to introduce a comonomer into PB-1 chain, which accelerates the transition From II to I and stabilizes the shape of the product as quickly as possible. Other ideas to accelerate this transformation include for example, the use of high pressure,[86, 87] mechanical deformation,[88-91] shear,[92] or additives (nucleating agents).[93-95]

References

[1] R.J. Young, P.A. Lovell, Introduction to polymers, CRC press 2011.

[2] P.C. Hiemenz, T.P. Lodge, Polymer chemistry, CRC press 2007.

[3] U. Gedde, Polymer physics, Springer 1995.

[4] J.M. Schultz, Polymer crystallization: the development of crystalline order in thermoplastic polymers, Americation Chemical Society 2001.

[5] B. Wunderlich, Macromolecular Physics, Volume 2: Crystal nucleation, growth, annealing, Academic press 1973.

[6] B. Wunderlich, Macromolecular physics, Volume 1: Crystal structure morphology, defects,

Academic press 1973.

[7] B. Wunderlich, Macromolecular Physics, Volume 3: Crystal melting, Academic press 1980.

[8] L. Mandelkern, Crystallization of Polymers, Volume 1: Equilibrium concepts, Cambridge University press 2002.

[9] L. Mandelkern, Crystallization of Polymers, Volume 2: Kinetics and mechanisms, Cambridge University press 2004.

[10] D.C. Bassett, Principles of polymer morphology, CUP Archive 1981.

[11] A.E. Woodward, Atlas of polymer morphology, Oxford University press 1989.

[12] E. Piorkowska, G.C. Rutledge, Handbook of polymer crystallization, John Wiley & Sons 2013.

[13] Q. Guo, Polymer morphology: principles, characterization, and processing, John Wiley & Sons 2016.

[14] G.R. Strobl, The physics of polymers, Springer 1997.

[15] G. Reiter, J.U. Sommer, Polymer crystallization: obervations, concepts and interpretations, Springer Science & Business Media 2003.

[16] G. Reiter, G.R. Strobl, Progress in understanding of polymer crystallization, Springer 2007.

[17] S.Z. Cheng, Phase transitions in polymers: the role of metastable states, Elsevier 2008.

[18] C. De Rosa, F. Auriemma, Crystals and crystallinity in polymers: diffraction analysis of ordered and disordered crystals, John Wiley & Sons 2013.

[19] W. Hu, Polymer physics: a molecular approach, Springer Science & Business Media 2012.

[20] B. Lotz, T. Miyoshi, S.Z. Cheng, 50th anniversary perspective: Polymer crystals and crystallization: Personal journeys in a challenging research field, Macromolecules 50(16) (2017) 5995-6025.

[21] G. Strobl, Crystallization and melting of bulk polymers: New observations, conclusions and a thermodynamic scheme, Progress in polymer science 31(4) (2006) 398-442.

[22] H. Huo, S. Jiang, L. An, J. Feng, Influence of shear on crystallization behavior of the β phase in isotactic polypropylene with β-nucleating agent, Macromolecules 37(7) (2004) 2478-2483.

[23] L. Balzano, Z. Ma, D. Cavallo, T.B. van Erp, L. Fernandez-Ballester, G.W. Peters, Molecular aspects of the formation of shish-kebab in isotactic polypropylene, Macromolecules 49(10) (2016) 3799-3809.

[24] Z. Wang, Z. Ma, L. Li, Flow-induced crystallization of polymers: Molecular and thermodynamic considerations, Macromolecules 49(5) (2016) 1505-1517.

[25] C.M. Wu, M. Chen, J. Karger-Kocsis, Transcrystallization in syndiotactic polypropylene

induced by high-modulus carbon fibers, Polymer Bulletin 41(2) (1998) 239-245.

[26] N. Billon, C. Magnet, J. Haudin, D. Lefebvre, Transcrystallinity effects in thin polymer films. Experimental and theoretical approach, Colloid and Polymer Science 272(6) (1994) 633-654.

[27] D.T. Quillin, D.F. Caulfield, J.A. Koutsky, Crystallinity in the polypropylene/cellulose system. I. Nucleation and crystalline morphology, Journal of applied polymer science 50(7) (1993) 1187-1194.

[28] J. Thomason, A. Van Rooyen, Transcrystallized interphase in thermoplastic composites, Journal of materials science 27(4) (1992) 897-907.

[29] A. Misra, B. Deopura, S. Xavier, F. Hartley, R. Peters, Transcrystallinity in injection molded polypropylene glass fibre composites, Die Angewandte Makromolekulare Chemie: Applied Macromolecular Chemistry and Physics 113(1) (1983) 113-120.

[30] J.L. Katz, M.D. Donohue, A kinetic approach to homogeneous nucleation theory, Advances in Chemical Physics 40 (1979) 137-155.

[31] S.L. Girshick, C.P. Chiu, Kinetic nucleation theory: A new expression for the rate of homogeneous nucleation from an ideal supersaturated vapor, The Journal of Chemical Physics 93(2) (1990) 1273-1277.

[32] E. Ruckenstein, Y. Djikaev, Recent developments in the kinetic theory of nucleation, Advances in colloid and interface science 118(13) (2005) 51-72.

[33] M. Sekine, K. Yasuoka, T. Kinjo, M. Matsumoto, Liquid–vapor nucleation simulation of Lennard-Jones fluid by molecular dynamics method, Fluid dynamics research 40(7-8) (2008) 597-605.

[34] H.M. Shim, J.K. Kim, H.S. Kim, K.K. Koo, Molecular dynamics simulation on nucleation of ammonium perchlorate from an aqueous solution, Crystal growth & design 14(11) (2014) 5897-5903.

[35] J. Anwar, D. Zahn, Atomistisches Verständnis der Keimbildung und des Kristallwachstums durch molekulare Simulationen, Angewandte Chemie 123(9) (2011) 2042-2061.

[36] R. Becker, W. Döring, Kinetische behandlung der keimbildung in übersättigten dämpfen, Annalen der Physik 416(8) (1935) 719-752.

[37] M. Volmer, A. Weber, Keimbildung in übersättigten Gebilden, Zeitschrift für physikalische Chemie 119(1) (1926) 277-301.

[38] P. Wagner, R. Strey, Measurements of homogeneous nucleation rates for n-nonane vapor using a two-piston expansion chamber, The Journal of Chemical Physics 80(10) (1984) 5266-

5275.

[39] C.H. Hung, M.J. Krasnopoler, J.L. Katz, Condensation of a supersaturated vapor. VIII. The homogeneous nucleation of n-nonane, The Journal of Chemical Physics 90(3) (1989) 1856-1865.

[40] A.I. Berezhnoi, Glass-ceramics and Photo-sitalls, Springer 1970.

[41] R.C. Reid, Superheated Liquids: Liquids in the superheated state, far from being a laboratory curiosity, occur more often than thought and may cause industrial accidents, American Scientist 64(2) (1976) 146-156.

[42] P.P. Wegener, Nonequilibrium flow with condensation, Acta mechanica 21(1) (1975) 65-91.

[43] F. Price, Nucleation, marcel dekker 1969.

[44] R. Cormia, F. Price, D. Turnbull, Kinetics of crystal nucleation in polyethylene, The Journal of Chemical Physics 37(6) (1962) 1333-1340.

[45] A. Sharples, The formation of nuclei in crystallizing polymers, Polymer 3 (1962) 250-252.

[46] A. Sharples, Introduction to polymer crystallization, Edward Arnold 1966.

[47] M. Volmer, Kinetik der phasenbildung, Verlag Von Theodor Steinkopff 1939.

[48] D. Turnbull, Isothermal rate of solidification of small droplets of mercury and tin, The Journal of Chemical Physics 18(5) (1950) 768-769.

[49] D. Turnbull, Formation of crystal nuclei in liquid metals, Journal of Applied Physics 21(10) (1950) 1022-1028.

[50] P. Till Jr, The growth of single crystals of linear polyethylene, Journal of Polymer Science 24(106) (1957) 301-306.

[51] E. Fischer, Stufen-und spiralförmiges Kristallwachstum bei Hochpolymeren, Zeitschrift für Naturforschung A 12(9) (1957) 753-754.

[52] A. Keller, A. O'connor, Large periods in polyethylene: The origin of low-angle X-ray scattering, Nature 180(4597) (1957) 1289-1290.

[53] D. Bassett, F. Frank, A. Keller, Evidence for distinct sectors in polymer single crystals, Nature 184(4689) (1959) 810-811.

[54] J.D. Hoffman, J.I. Lauritzen Jr, Crystallization of bulk polymers with chain folding: theory of growth of lamellar spherulites, Journal of research of the National Bureau of Standards. Section A, Physics and chemistry 65(4) (1961) 297.

[55] J. Hoffman, Theoretical aspects of polymer crystallization with chain folds: bulk polymers, Polymer Engineering & Science 4(4) (1964) 315-362.

[56] J.D. Hoffman, R.L. Miller, Kinetic of crystallization from the melt and chain folding in

polyethylene fractions revisited: theory and experiment, Polymer 38(13) (1997) 3151-3212.
[57] D. Sadler, G. Gilmer, A model for chain folding in polymer crystals: rough growth faces are consistent with the observed growth rates, Polymer 25(10) (1984) 1446-1452.
[58] D.M. Sadler, Roughness of growth faces of polymer crystals: Evidence from morphology and implications for growth mechanisms and types of folding, Polymer 24(11) (1983) 1401-1409.
[59] F.C. Frank, M. Tosi, On the theory of polymer crystallization, Proceedings of the Royal Society of London. Series A. Mathematical and Physical Sciences 263(1314) (1961) 323-339.
[60] J.-J. Point, Reconsideration of kinetic theories of polymer crystal growth with chain folding, Faraday Discussions of the Chemical Society 68 (1979) 167-176.
[61] J. Point, A new theoretical approach of the secondary nucleation at high supercooling, Macromolecules 12(4) (1979) 770-775.
[62] D. Sadler, G. Gilmer, Rate-theory model of polymer crystallization, Physical review letters 56(25) (1986) 2708.
[63] M. Hikosaka, Unified theory of nucleation of folded-chain crystals and extended-chain crystals of linear-chain polymers, Polymer 28(8) (1987) 1257-1264.
[64] W. Hu, D. Frenkel, V.B. Mathot, Intramolecular nucleation model for polymer crystallization, Macromolecules 36(21) (2003) 8178-8183.
[65] M. Muthukumar, Nucleation in polymer crystallization, Advances in Chemical Physics 128 (2004) 1-64.
[66] B. Wunderlich, Reversible crystallization and the rigid–amorphous phase in semicrystalline macromolecules, Progress in polymer science 28(3) (2003) 383-450.
[67] H. Suzuki, J. Grebowicz, B. Wunderlich, Glass transition of poly (oxymethylene), British polymer journal 17(1) (1985) 1-3.
[68] J. Lee, J.H. Mangalara, D.S. Simmons, Correspondence between the rigid amorphous fraction and nanoconfinement effects on glass formation, Journal of Polymer Science Part B: Polymer Physics 55(12) (2017) 907-918.
[69] D. Cangialosi, A. Alegria, J. Colmenero, Effect of nanostructure on the thermal glass transition and physical aging in polymer materials, Progress in polymer science 54 (2016) 128-147.
[70] M.L. Di Lorenzo, M.C. Righetti, The three-phase structure of isotactic poly (1-butene), Polymer 49(5) (2008) 1323-1331.
[71] K.Y. Lin, M. Xanthos, K. Sirkar, Novel polypropylene microporous membranes via spherulitic deformation–Processing perspectives, Polymer 50(19) (2009) 4671-4682.

[72] S. Martin, M.T. Expósito, J.F. Vega, J. Martínez-Salazar, Microstructure and properties of branched polyethylene: Application of a three-phase structural model, Journal of applied polymer science 128(3) (2013) 1871-1878.

[73] H. Bai, F. Luo, T. Zhou, H. Deng, K. Wang, Q. Fu, New insight on the annealing induced microstructural changes and their roles in the toughening of β-form polypropylene, Polymer 52(10) (2011) 2351-2360.

[74] J. Lin, S. Shenogin, S. Nazarenko, Oxygen solubility and specific volume of rigid amorphous fraction in semicrystalline poly (ethylene terephthalate), Polymer 43(17) (2002) 4733-4743.

[75] M. Drieskens, R. Peeters, J. Mullens, D. Franco, P.J. Lemstra, D.G. Hristova-Bogaerds, Structure versus properties relationship of poly (lactic acid). I. Effect of crystallinity on barrier properties, Journal of Polymer Science Part B: Polymer Physics 47(22) (2009) 2247-2258.

[76] A. Guinault, C. Sollogoub, V. Ducruet, S. Domenek, Impact of crystallinity of poly (lactide) on helium and oxygen barrier properties, European Polymer Journal 48(4) (2012) 779-788.

[77] V.G. Natta, P. Corredini, I. Bassi, Über die Kristallstruktur des isotaktischen Poly-a-butens, Die Makromolekulare Chemie 21(3) (1956) 240-244.

[78] G. Natta, P. Pino, P. Corradini, F. Danusso, E. Mantica, G. Mazzanti, G. Moraglio, Crystalline high polymers of α-olefins, Journal of the American Chemical Society 77(6) (1955) 1708-1710.

[79] R.L. Miller, L.E. Nielsen, Crystallographic data for various polymers. II, Journal of Polymer Science 55(162) (1961) 643-656.

[80] K. Tashiro, H. Asanaga, K. Ishino, R. Tazaki, M. Kobayashi, Development of a new software for the X-ray structural analysis of polymer crystals by utilizing the X-ray imaging plate system, Journal of Polymer Science Part B: Polymer Physics 35(11) (1997) 1677-1700.

[81] G. Natta, The crystalline structure of several isotactic polymers of α-olefins, Rend. Fis. Acc. Lincei. 19 (1955) 404-411.

[82] K. Tashiro, J. Hu, H. Wang, M. Hanesaka, A. Saiani, Refinement of the crystal structures of forms I and II of isotactic polybutene-1 and a proposal of phase transition mechanism between them, Macromolecules 49(4) (2016) 1392-1404.

[83] V. Holland, R.L. Miller, Isotactic polybutene-1 single crystals: morphology, Journal of Applied Physics 35(11) (1964) 3241-3248.

[84] A.T. Jones, Polybutene-1 – type II crystalline form, Journal of Polymer Science Part B: Polymer Letters 1(8) (1963) 455-456.

[85] G. Cojazzi, V. Malta, G. Celotti, R. Zannetti, Crystal structure of form III of isotactic poly-

1-butene, Die Makromolekulare Chemie: Macromolecular Chemistry and Physics 177(3) (1976) 915-926.

[86] C.D. Armeniades, E. Baer, Effect of pressure on the polymorphism of melt crystallized polybutene-1, Journal of Macromolecular Science, Part B: Physics 1(2) (1967) 309-334.

[87] J. Shi, P. Wu, L. Li, T. Liu, L. Zhao, Crystalline transformation of isotactic polybutene-1 in supercritical CO2 studied by in-situ fourier transform infrared spectroscopy, Polymer 50(23) (2009) 5598-5604.

[88] A. Tanaka, N. Sugimoto, T. Asada, S. Onogi, Orientation and crystal transformation in polybutene-1 under stress relaxation, Polymer Journal 7(5) (1975) 529-537.

[89] T. Hsu, P. Geil, Deformation and stress-induced transformation of polybutene-1, Journal of Macromolecular Science, Part B: Physics 28(1) (1989) 69-95.

[90] K. Nakamura, T. Aoike, K. Usaka, T. Kanamoto, Phase transformation in poly (1-butene) upon drawing, Macromolecules 32(15) (1999) 4975-4982.

[91] W. Wang, C. Shao, L. Zheng, B. Wang, L. Pan, G. Ma, Y. Li, Y. Wang, C. Liu, Z. Ma, Stretching-induced phase transition of the butene-1/ethylene random copolymer: Orientation and kinetics, Journal of Polymer Science Part B: Polymer Physics 57(2) (2019) 116-126.

[92] K.-H. Lee, C.M. Snively, S. Givens, D.B. Chase, J.F. Rabolt, Time-dependent transformation of an electrospun isotactic poly (1-butene) fibrous membrane, Macromolecules 40(7) (2007) 2590-2595.

[93] V. Causin, C. Marega, A. Marigo, G. Ferrara, G. Idiyatullina, F. Fantinel, Morphology, structure and properties of a poly (1-butene)/montmorillonite nanocomposite, Polymer 47(13) (2006) 4773-4780.

[94] S.D. Wanjale, J.P. Jog, Crystallization and phase transformation kinetics of poly (1-butene)/MWCNT nanocomposites, Polymer 47(18) (2006) 6414-6421.

[95] C. Marega, V. Causin, R. Neppalli, R. Saini, G. Ferrara, A. Marigo, The effect of a synthetic double layer hydroxide on the rate of II→ I phase transformation of poly (1-butene), Express Polymer Letters 12 (2011) 1050-1061.

[96] X. Tang, W. Chen, L. Li, The tough journey of polymer crystallization: battling with chain flexibility and connectivity, Macromolecules 52(10) (2019) 3575-3591.

Chapter 3. Materials and techniques

3.1 Materials

Two commercial grade isotactic PB-1 samples with different molar mass were kindly provided by LyondellBasell. The details of the polymer samples are listed in Table 3.1.

Table 3.1 Characterization of the polybutene-1 (PB-1) samples

Trade name	melt flow rate (MFR) (190 °C/2.16)	M_w (kg/mol)	M_w/M_n
PB0110M	0.4	850	6.8
PB0300M	4	295	4.6

3.2 Experimental techniques

3.2.1 Polarized light optical microscopy

When light enters an isotropic medium, it is refracted at a constant angle and passes through the medium at a single velocity. However, when light enters an anisotropic crystal, it is refracted into two rays, each polarized with the vibration directions oriented at right angles (mutually perpendicular) to one another and traveling at different velocities. This phenomenon is termed double refraction or birefringence, and is exhibited to a greater or lesser degree in all anisotropic crystals.

Polarized light optical microscopy (PLOM) provides a unique window into the internal structure of crystals of crystalline polymers. With the orthogonal field of two polarizing filters (“crossed polars”), many properties can be deduced: shape, size and number of crystals, extinction angle, sign of the birefringence/degree of birefringence, among others.

In this thesis, the morphology and the nucleation behavior were observed in situ by a Leica DMLP optical microscope under crossed polarizers, equipped with a computer-controlled digital camera (Optika B5). The thermal treatments were applied by a calibrated Mettler Toledo FP-82HT hot-stage.

3.2.2 Wide-angle X-ray diffraction

The Wide-angle X-ray diffraction (WAXD) or Wide-angle X-ray scattering (WAXS) is an x-ray technique that is often used to determine the crystalline structure of different materials. This technique specifically refers to the analysis of Bragg peaks scattered to wide angles ($2\theta > 1^{o}$), which implies by Bragg's law that they are caused by subnanometer–sized structures.

The law states that when the X-ray is incident onto a crystal surface, its angle of incidence, θ, will reflect back with a same angle of scattering, θ. And, when the path difference, d is equal to an integer number, n, of the wavelength λ, a constructive interference will occur. In other words, Bragg's law provides the condition for a plane wave to be diffracted by a family of lattice planes, as is show in equation (3.1)

$$2dsin\theta = n\lambda \tag{3.1}$$

where d is the interplanar spacing (path difference), θ the angle between the wave vector of the incident plane wave and the lattice planes (the angle between incident ray and the scatter plane), λ is the wavelength and n is an integer, the order of the diffraction.

Classical small-angle X-ray scattering (SAXS) and X-ray diffraction (XRD) studies are well established tools for the characterization of crystalline structure of polymers. High signal levels are achieved in particular with synchrotron radiation, but still largely rely on macroscopic ensemble-averaging. Local distributions of structural properties cannot be accessed with such an approach. Thus, the drive towards smaller beam sizes for diffraction experiments is mainly motivated by the possibility of probing the structure of hierarchically organized materials at increasingly smaller scales. Under the practical aspects having a smaller beam allows smaller sample volumes to be studied with better signal-to-noise statistics. It also supports scanning studies at higher spatial resolutions, allowing diffraction to be employed much like other scanning-based imaging tools (e.g. SEM, STM).

In Chapter 5, scanning nano-diffraction measurements were performed at beamline ID13 of the European Synchrotron Radiation Facility. The measurements were performed in transmission geometry with the sample surface normal to the X-ray beam. The region of interest was selected with help of a retractable on-axis optical microscope. The focal point of this microscope is pre-aligned with the focal point of the beam, and thus allows the accurate positioning of the desired sample locations in the working point of the nano-diffraction setup.

The focal spot size of the beam at a sample position of 200 × 200 nm² (full width at half-maximum, FWHM) was achieved by focusing the monochromatic X-ray beam with a set of silicon-based compound refractive lenses optimized for a photon energy of 14.85 keV. The wavelength of the beam used in this experiment was 0.83491 Å. 2D diffractograms were

collected using a hybrid photon counting area detector (EigerX 4M, Dectris) with a pixel size of 75 μm. The detector was placed approximately 25.3 cm downstream the sample position. To reduce parasitic scattering from the air, a flight tube filled with Helium was placed in between the sample and the detector. The diffraction geometry including the sample detector distance and orientation was calibrated using Fit2D and α-alumina as a reference standard.

Finally, an area of 30 × 60 μm^2 for a cross-nucleated sample, in the form of a free-standing polymer film, was in situ mapped, using a step size of 0.5 μm between each collected pattern. As a compromise between the optimal diffraction signal and minimal beam damage of the polymer film, an acquisition time of 500 ms per frame was used.

3.2.3 Atomic force microscopy

Atomic force microscopy (AFM) is a high-resolution scanning probe microscope with a resolution of fractions of nanometers, which has more than 1000 times higher resolution compared to the classical optical microscope. AFM contains a micro- and nanoscale cantilever with a silicon or silicon nitride sharp tip (probe) at its end, that enables us to perceive the shape of a surface in three-dimensional detail down to the nanometer scale. CNTs can be attached to the tip of the cantilever to make a sharper tip to increase the image resolution of the surfaces at the Angstrom level. Usually, three different AFM modes can be employed in an AFM unit, including contact mode, non-contact mode, and tapping mode.

In Chapter 6, the tapping mode has been employed using ICON AFM from Bruker equipped with Nanoscope V controller for the quantitative analysis of investigated fibers' topography. TESP-V2 tip (nominal radius: 10 nm and cantilever length: 125 μm) with frequency of ~320 kHz was used to carry out 512 scan lines at scan rates of 0.4-0.7 Hz. A second-order flatten function was employed for the extraction of each AFM height profile. Additionally, the root mean square roughness (rms or R_q) has been determined using 10 independent zones from 5 μm × 5 μm AFM height images of fiber surface. The AFM images were analyzed by NanoScope Analysis software version 1.90.

3.2.4 Differential scanning calorimetry

Differential scanning calorimetry (DSC) is a thermal analysis technique in which the difference in the amount of heat required to vary the temperature of a sample and that of a reference is measured as a function of temperature or time, while the sample is exposed to a controlled temperature program. Both the sample and reference are maintained at nearly the same temperature throughout the experiment. It is a very powerful technique to evaluate

material properties such as glass transition temperature, melting, crystallization, specific heat capacity, cure process, purity, oxidation behavior, and thermal stability.

In Chapter 7, thermal analyses of the samples were carried out by means of a differential scanning calorimeter (DSC-250) equipped with a refrigerating cooling system RCS90 from TA Instruments. Dry nitrogen was used as purge gas at a rate of 50 mL/min. The temperature was calibrated with the onset of the melting transition peak for high purity indium, which was used also for energy calibration.

Chapter 4. Cross-nucleation in seeded crystallization of isotactic polybutene-1

4.1 Introduction

It is well known that many semicrystalline polymers exhibit pronounced polymorphisms,[1-3] which show a strong influence on their properties. For example, isotactic polypropylene (iPP) exhibits at least three different crystal modifications, designated as α, β, and γ forms depending on the processing conditions, the chemical structure of the macromolecule and the presence of specific additives.[4-6] An earlier-nucleating crystalline polymorph can nucleate another crystalline polymorph of higher or lower thermodynamic stability, without undergoing any polymorphic transformation. This phenomenon has been named cross-nucleation and occurs on crystals sharing the same composition (although with different structure) rather than on foreign particles.[7-12] Cross-nucleation between polymorphs is important for the industrial control of polymorphism and the fundamental understanding of nucleation, and it has been mainly described as a particular case of heterogeneous nucleation.

Particular attention has been paid in the past decades to heterogeneous nucleation of polymer crystals on foreign surfaces of nucleating agents (NAs) or fiber composites. An interfacial free energy difference parameter, $\Delta\sigma$, resulting from the formation of the crystalline layer onto the heterogeneous substrate, is often used for comparing the nucleating ability of different substrates and understanding the nucleation process on the surfaces of the heterogeneities. For example, Wang et al. studied the nucleation kinetic of iPP on the surface of different kinds of fiber and determined different values of $\Delta\sigma$ for each system.[13-15] Kawamoto et al. investigated the effect of the epitaxy of a NA on nucleation of polypropylene based on kinetic study. It was found that nucleation rate at constant undercooling increased by 60 times with decreasing $\Delta\sigma/\sigma$ from 0.23 to 0.13, which confirms that $\Delta\sigma$ is extremely sensitive for detecting the nucleating ability of a substrate.[16] For what concerns cross-nucleation, although the kinetics of the process has already been studied for several systems,[17-20] a detailed description based on $\Delta\sigma$ calculation was not extensively applied.

Moreover, the effect of the substrate morphology on cross-nucleation is still poorly understood. Chen et al. studied cross-nucleation between the polymorph of “ROY” molecule, finding a meaningful effect of the nature of the seed surface on cross-nucleation rate, by

comparing baked and unbaked samples. [8] Tao et al. revealed that different faces of a single-crystalline seed differed in their ability to cross-nucleate. In particular, using an elongated β-phase crystal of D-Mannitol in contact with the undercooled melt, cross-nucleation of the α-phase occurred immediately if the seeds was placed side-on, while the parent β-polymorph could grow to some extent before cross-nucleation happened, in case of end-on seed orientation.[11]

For such a study in polymorphic polymers, PB-1 is an ideal system because it exhibits several polymorphs of known structures and known thermodynamic relations. In fact, this polymer can crystallize in Forms I/I', II, and III.[21, 22] It is well established that the Form II, commonly produced by melt crystallization, is the kinetically favored modification, but it is metastable from the thermodynamic point of view. Form II has a tetragonal unit cell with 11/3 helical conformations.[23-26] Since the nucleation of the stable Form I occurs much more rarely in bulk crystallization than that of the predominant Form II, it can only be obtained through solid-solid transition from Form II. However, Form I', described as a defective Form I with lower melting temperature, can be formed through special crystallization procedures, such as solution crystallization,[27] blending with isotactic polypropylene,[28] or copolymerization with other monomers.[29-31] Actually, quiescent aging at room temperature of Form II samples is generally used for generating trigonal Form I, where the molecular conformation of the chains is that of a 3/1 helix.[32-37]

Given that the spherulitic seed of Form I in contact with PB-1 melt has proven to efficiently cross-nucleate the metastable polymorph,[18, 38] in this chapter we aim at gaining some insights on the role of the substrate type on cross-nucleation. For this purpose, a polarized optical microscopy measurement is employed to achieve a time resolution sufficient to resolve the phenomena studied.

4.2 Experimental

4.2.1 Sample preparation

The polymer studied in the present work is a butene-1 homopolymer (PB-1) with commercial-grade name of PB0110M. The details of this polymer were listed in Table 3.1. Granules of PB-1 were used without any further treatment to make thin films, 30-50 μm thick, by compression-molding at a temperature of 180 °C. PB-1 fibers used in this chapter were lab-spun using a capillary rheometer (RH7, Bohlin) at the Institute of Chemistry of the Chinese

Academy of Science in Beijing, by the group of Prof. Dujin Wang. The temperature of the barrel was 180 °C and the rotation speed of the collector was set to 200 rpm.

To prepare the substrates of interest characterized by different morphologies, the thin film samples were heated up to 180 °C in a Mettler FP90 hot-stage, kept at this temperature for 5 minutes to erase the previous processing history, and further cooled to the crystallization temperature. Temperatures of 90 and 108 °C were selected, in order to obtain a spherulitic and a hedritic morphology, respectively.[39] After an appropriate crystallization time of approximately 4 and 270 min at low and high temperature, respectively, morphologies of similar size were reached in the two cases. Then the samples were quickly cooled down to room temperature and aged for more than one month to completely transform the original Form II crystals into Form I. It should be noted that, according to previously adopted procedures for cross-nucleation studies in PB-1, a dual morphology is produced.[18, 38, 40] Indeed, low melting temperature crystals of Form I, formed during quenching to room temperature, are essential for having molten PB-1 in contact with crystalline Form I seeds (with higher melting temperature).[17, 18]

4.2.2 PLOM analysis

For the in-situ PLOM characterization during isothermal crystallization, the employed technique was described in section 3.2.1. To investigate the nucleation on the substrates of spherulite and hedrite, the Form I films were heated to different melting temperatures (T_h) at 20 °C/min, and kept for 5 minutes to melt completely Form II crystals or Form I crystals with lower thermal stability, and subsequently quenched to T_c for performing the isothermal crystallization (Figure 4.1a).

For the experiments with the fiber substrate, these thin PB-1 films were first heated to 180 °C and kept at this temperature for 5 minutes to erase the previous processing history, then they were cooled down to different melting temperatures (T_h). The PB-1 fibers, containing Form I crystals, were then manually introduced in the film at this temperature. After a second annealing step at T_h, to relax the induced stresses, the samples were cooled down to the selected crystallization temperature (T_c) (Figure 4.1b). The described thermal protocols are presented in Figure 4.1.

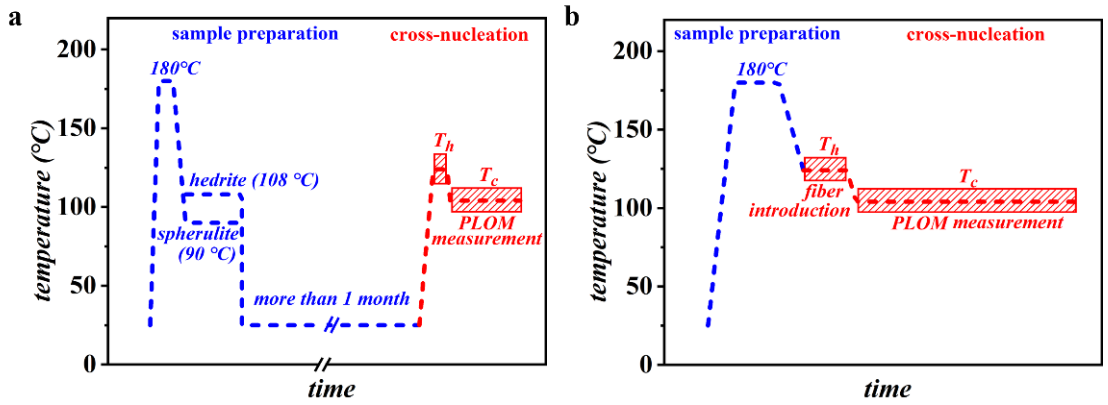

Figure 4.1 Thermal programs applied for (a) obtaining the spherulite and the hedrite substrates and performing the cross-nucleation experiments on them, and for (b) executing cross-nucleation on the PB-1 fibers.

4.3 Results

4.3.1 Determination of nucleation induction time via light intensity measurements

Figure 4.2 shows an example of the time-resolved images obtained during isothermal crystallization, and explains the method used for induction time determination. Nucleation of Form II crystals occurs at every place on the side of the original Form I spherulite, forming a sort of crystalline "corona" around it (Figure 4.2a). In order to accurately detect the induction time, that is, the time at which the Form II cross-nuclei have reached a critical size and the crystalline growth proceeds, the increase of the light intensity in the sample due to the formation of birefringent Form II crystals is exploited. A circular "Region of Interest", centered in the middle of the nucleating spherulite, is selected on the image analysis software, and the mean light intensity in the selected area is then calculated for each acquired frame. By plotting this intensity as a function of time (Figure 4.2b), it is possible to unambiguously determine the time at which it starts to increase from its initial value, that is, the induction time. Further details on the analysis method can be found in our recent work.[41] The exact value of the induction time is determined by the intersection point between two fitting lines: one in the time region of the initial plateau value and the second in the first growth step part. An example of the analyzed data is reported in Figure 4.2b.

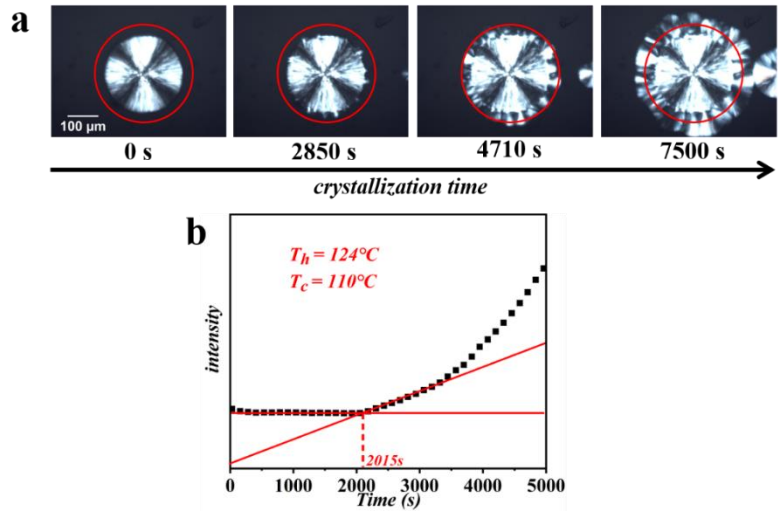

Figure 4.2 (a) Polarized optical micrographs of PB-1 nucleated on the surface of the spherulitic seed of Form I, at different times during crystallization at 110 °C. (b) Corresponding evolution of light intensity in the selected area (highlighted with a red circle in (a)), as a function of time.

4.3.2 Cross-nucleation of PB-1 Form II on Form I seeds with different morphology

Figure 4.3 shows some representative optical micrographs of PB-1 crystallized on the surface of Form I substrates with different morphologies: spherulite, hedrite and fiber. All the samples were crystallized isothermally at 105 °C, after melting the original Form II/Form I crystals at 124 °C. The thermal treatment at relatively high temperature ensures that the remaining seeds are composed of Form I only, while any crystalline memory of possible residual Form II crystals (i.e., self-nucleation) is erased.[40] In all the three morphologies, a clear transcrystalline layer (TCL), indicative of a very high "linear density" of nucleation sites, develops with time. The TCL[13, 14, 42, 43] is a consequence of lack of lateral separation between the individual growing spherulites on the nucleating surface, causing the crystals to grow exclusively perpendicularly to it. It is apparent that the nucleating efficiency of the three substrates is particularly high, however, some subtle difference among the three can be captured. In fact, while individual splaying spherulites can be somehow recognized in Figures 4.3a,b (with spherulitic or hedritic Form I seeds), this is not the case for the crystals nucleating on the fiber surface, due to the extremely high nucleation density.

However, the different cross-nucleating ability of the various substrates can be more clearly deduced by comparing the time evolution of the morphology, at the same crystallization temperature. The second column of Figure 4.3 reports for each case the time at which the first cross-nucleation event could be observed (highlighted by the red circles). It can be seen that a

substantially shorter time is required for cross-nucleation to occur on the fiber substrate, with respect to the spherulitic or hedritic ones. In the last images of Figures 4.3a-c, the TCL has grown to a similar thickness in all the three morphologies, being the growth rate the same in the three experiments, the earlier onset of growth, that is, shorter induction time, for the fiber sample is confirmed.

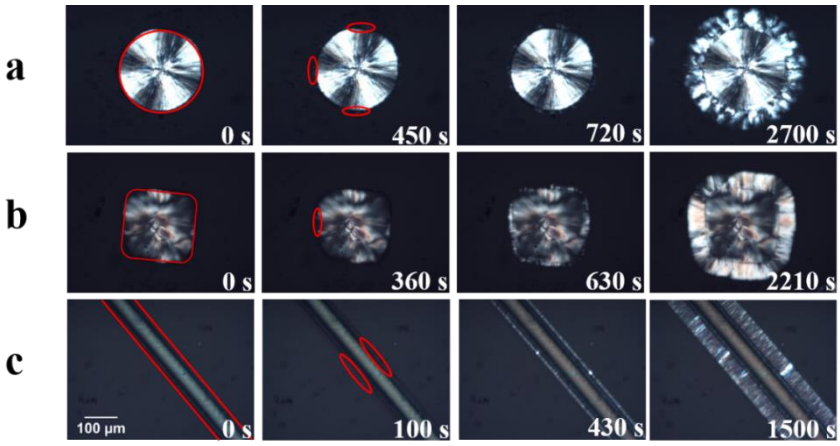

Figure 4.3 Polarized optical micrographs of PB-1Form II nucleated on the surface of (a) spherulitic, (b) hedritic and (c) fibrous Form I substrates for different indicated crystallization times at 105°C.

During primary nucleation, a particular molecular arrangement must be fulfilled to allow the formation of the new phase. In the case of polymer crystallization from the melt, the chain segments must approach themselves to distances commensurate to those characteristics of the crystalline unit cell and must possess the right conformation, as the crystal symmetry imposes. The chain segments with those attributes form a crystalline aggregate which varies the system free energy ΔG. Considering for the sake of simplicity a spherical nucleus of radius r, a maximum in $\Delta G(r)$ exists which corresponds to the critical size (r^*) that the new crystal must attain in order to be able to spontaneously grow into a crystal. Clusters smaller than r^* are called subcritical nuclei or embryos, they are unstable and tend to disappear from the system. Aggregates that exceed r^* are called supercritical nuclei and can continue to grow because their growth is thermodynamically favored.[44]

As the magnitude of the energy barrier for nucleation depends inversely on the undercooling, that is, on the distance between the crystallization and melting temperature, experiments were performed at different crystallization temperatures. Figure 4.4a reports the example of evolution of light intensity, extracted from the optical micrographs, as a function

of time during crystallization at different temperatures for the fibrous Form I substrate. The time of formation of the critical nuclei, represented by the light intensity induction time, gets shorter and shorter with decreasing T_c for any of the considered substrates. In particular while the differences between spherulitic and hedritic Form I seeds are relatively small (data are reported in Appendix A1), the high cross-nucleation efficiency of the Form I fiber is apparent by comparing the time scale of the x-axis (Figure 4.4a). A clearer comparison between the three seeds is offered in Figure 4.4b, which considers the increase in transmitted light at the same crystallization temperature for the three different systems. The chosen condition is the same reported in the micrographs of Figure 4.3. A difference of about a factor 0.8 in the induction time can be already appreciated between the spherulitic or hedritic seeds, while Form I fibers substrate can nucleate Form II about two to three times faster than Form I spherulite.

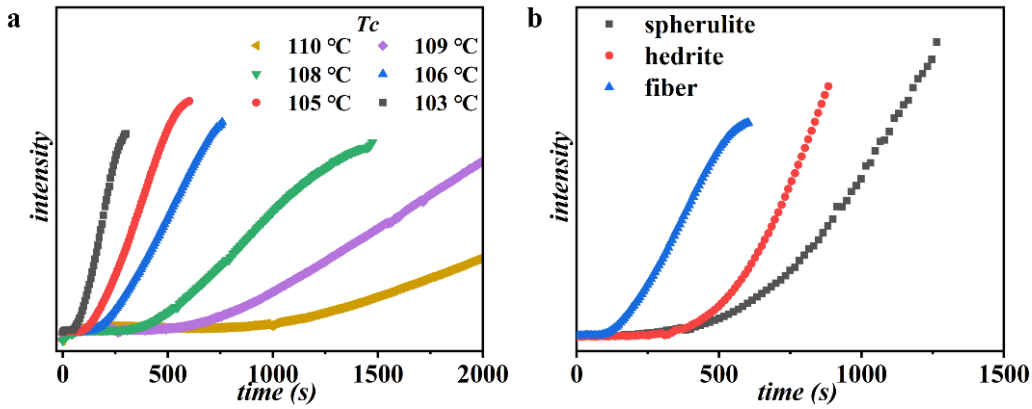

Figure 4.4 (a) Evolution of light intensity as a function of crystallization time during isothermal crystallization at different temperatures for the fiber Form I substrate. (b) Comparison of light intensity vs time for the different Form I substrates crystallizing at 105 °C.

In order to apply a model-based comparison of the cross-nucleation ability associated to different Form I morphologies, the values of the determined induction times as a function of temperature are reported in Figure 4.5. The order of efficiency deduced from Figures 4.3, 4.4 and Appendix A1, that is, fiber > hedrite > spherulite, is confirmed in the whole range of explored undercooling. As expected, a strong dependence of nucleation kinetics on the crystallization temperature is observed, with induction times increasing exponentially approaching the melting point of Form II.

It should be pointed out that both spherulitic and hedritic Form I substrates were prepared in-situ in the sample, by melt crystallization, while fibrous Form I seed was introduced into the matrix melt manually. The insertion process necessarily involved shear stresses applied to the

PB-1 melt. Given the fact that flow-induced nucleation in fiber-pulling experiments is well documented, and is known to have long-lasting effects,[45] the evaluation of its importance in the present case is mandatory, in order to understand whether a fiber-like Form I really possesses the highest cross-nucleation efficiency.

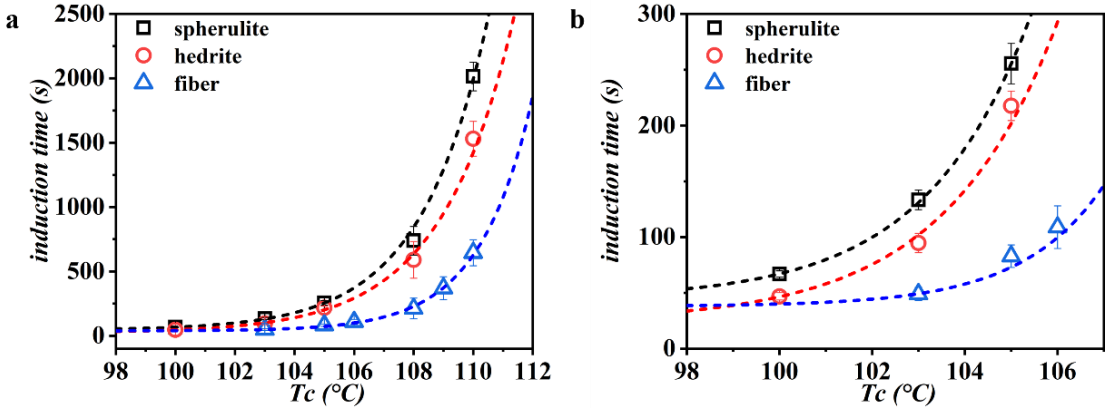

Figure 4.5 (a) Induction time for the cross-nucleation of Form II on Form I as a function of T_c for Form I seeds with different morphologies. (b) Magnification of the low crystallization temperature region.

The annealing times were varied in a wide range, according to the known long lifetime of PB-1 flow-induced precursors.[45] Appendix A2 reveals that the change of the induction time, with melt annealing time, if any, is safely negligible and cannot account for the large difference observed for the case between the nucleation time of Form II at the interface with the fiber and with the hedrite of Form I (around 140 s).

To further confirm that nucleation of Form II on top of Form I fibers is not dominated by shear-induced effects, the same experiment, including the fiber introduction step, using a completely different fiber, made of isotactic polypropylene (iPP), was performed. Since the elastic moduli and size of the two fibers are not largely different, similar shear stresses are expected to be generated by the fiber introduction procedure in the two cases. The induction times observed for nucleation on iPP and Form I PB-1 fibers are compared in Appendix A3. Very different nucleation kinetics of Form II are observed on the two fibers. In particular nucleation on iPP fiber occurs more slowly than cross-nucleation on Form I PB-1 fiber. This observation further supports our previous conclusion: the effect of shear-induced nucleation due to the sample preparation procedure is not meaningful. In the opposite case, a similar kinetic of nucleation would be observed for the two fibers. Thus, the observed faster nucleation promoted by the Form I PB-1 fiber, with respect to the other PB-1 substrates made of the same

crystalline polymorph but possessing different morphologies, is confirmed.

4.3.3 Crystal growth of PB-1 Form II on Form I seeds with different morphology

In order to exclude any possible difference between the growth rates of Form II crystals in the different samples, and in view of obtaining surface energy data for the subsequent estimation of the nucleation barrier, the growth kinetics in the different samples was determined by following the time dependence of the TCL thickness.

Appendix A4 shows the thickness of the TCLs of Form II growing at the interface of the Form I seeds with different morphologies, measured via PLOM, as a function of crystallization time for various crystallization temperatures. The increase in size is linear with time, which allows an easy calculation of the growth rate from the slope of the fitting lines. As expected, the crystal growth rate of PB-1 Form II increases with decreasing the isothermal crystallization temperature. This change is more marked in the temperature range 103 °C to 110 °C. The derived crystal growth rates are thus analyzed according to the classical Lauritzen-Hoffman theory. The growth rate (G) can be expressed by a function of the undercooling ΔT in a linearized form, according to:

$$\ln G = \ln G_0 - \frac{U^*}{R(T - T_\infty)} - \frac{\beta b_0 \sigma \sigma_e T_m}{k \Delta h_0} \frac{1}{T \Delta T f} \tag{4.1}$$

The constants that appear in equation (4.1) are: G_0 is a temperature-independent parameter. U^* is the activation energy related to the transport of chain segments across the phase boundary, R is the gas constant, T_∞ is the temperature below which all motions associated with viscous flow cease, β is a constant characterizing the regime of growth , b_0 is the thickness of each newly formed layer, σ and σ_e are the lateral and fold surface energies, respectively; T_m is the equilibrium melting temperature, k is the Boltmann constant, Δh_0 is the melting enthalpy and f is a correction factor which takes into account the change of melting enthalpy with crystallization temperature.

Appendix A5 shows the trend of $\log G + U^*/R(T-T_\infty)$ as a function of $1/(T\Delta T f)$. The linear fit of the growth rate data with the L-H model with a single slope in the whole undercooling range implies that only one regime is active between 100 °C and 110 °C. This corresponds to regime I, in agreement with the results of Monasse and Haudin.[46] On the other hand, it is apparent that the TCL of PB-1 Form II grows in the melt with the same rate, independently from the exact substrate on which it nucleates. Therefore, it can be concluded that the observed differences in the kinetics of light intensity evolution among the different Form I seeds, are not

related to the growth stage, but can correctly be attributed to the cross-nucleation kinetics only.

Muchova et.al[47] has developed a microscopic method to monitor the early stages of the spherulite growth of polypropylene. They found that there are two relations between the derivative of the light intensity (φ) with respect to the time:

$$\frac{d\varphi}{dt} = KZv^4(t - t_i)^3 \tag{4.2}$$

$$\frac{d\varphi}{dt} = KZv^2(t - t_i) \tag{4.3}$$

where v is the linear growth rate, which is constant at a given crystallization temperature, Z is the number of growing spherulites, K is a constant which involves the dependence of the transmitted light intensity on the difference in the refractive indices of the ordinary and extraordinary beams, t is the time and t_i is the induction time. The first equation describes the derivative of the light intensity when the spherulites growth can be considered three-dimensional (3D), while the second relation refers to the case of two-dimensional (2D) growth. Representative examples of the evolution of the time derivative of light intensity with respect to time for the different Form I substrates are shown in Appendix A6. In all the cases, after the initial transient a clear linear region of the data can be identified, confirming the adequacy of equation (4.3), that is, the growth of PB-1 Form II on the different substrates can be considered 2D. Similar conclusions on this method have been recently drawn by analyzing the light intensity arising from the development of PP transcrystalline layers at the interface with solid NAs.[41]

The relationship between the growth rate values of the TCL, calculated through the thickness vs. time measurements and the light intensity method, has been further explored. Figure 4.6 shows the growth rate values calculated at different T_c from TCL thickness analysis (Appendix A4), as a function of the parameter Av, defined as the square root of the fitting slope of the linear part in the plot of the light intensity method (Appendix A6). From equation (4.3), we can derive that A is a constant equal to $(KZ)^{1/2}$. If the applied model is correct, a linear relationship between these two independently derived quantities should be obtained. As can be seen in Figure 4.6, the growth rate data for all the different substrates fall on the same line. Therefore, we can conclude that this model for the data analysis is validated, analogously to our previous work on heterogeneous nucleation of polypropylene,[41] and that the parameters K and Z are independent from the morphology of the Form I seeds.

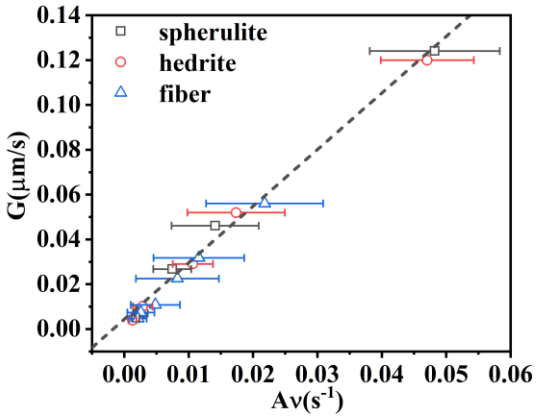

Figure 4.6 Growth rate (G) values at different T_c calculated from TCL thickness in time experiments as a function of the parameter Av (see text) obtained through the light intensity method. Data for the different PB-1 substrates are reported and the dashed line represents the best linear fit to the whole data set.

4.3.4 Model analysis for cross-nucleation of PB-1 Form II on Form I seeds

In the presence of heterogeneous substrates in contact with the polymer melt, there is the availability of solid surfaces on which the embryos can form. Several different types of heterogeneity (extraneous solids, cavities, already formed crystal surfaces, etc.) can enhance the formation of stable embryos and have important implications for polymer crystallization. One classical approach assumes the formation of prismatic embryos with a rectangular cross-section of size a and b, and height (l) in the direction of the chain axis on a flat surface. In this case, the change in the Gibbs energy has the form:

$$\Delta G_{het} = -abl\Delta g + 2bl\sigma + al\Delta\sigma + 2ab\sigma_e \tag{4.4}$$

Where σ is the free energy of the lateral surfaces in contact with the undercooled melt, σ_e is the free energy of the surfaces perpendicular to the chain direction and $\Delta\sigma$ is the interfacial free energy difference, given by:

$$\Delta\sigma = \sigma + \sigma_{s/c} - \sigma_{s/m} \tag{4.5}$$

in which $\sigma_{s/c}$ is the crystal-substrate interfacial energy and $\sigma_{s/m}$ is the melt-substrate interfacial energy. Therefore, $\Delta\sigma$ can be brought down to the surface tension properties of the substrate, polymer crystal, and polymer melt. Thus, $\Delta\sigma$ is a convenient way to define the nucleating ability of the substrate toward the polymer melt. The lower its value, the lower the nucleation energy barrier, resulting in a faster nucleation.

Ishida et al. have proposed a model according to which the formation of the first layer of

crystalline segments on the foreign substance is responsible of the attainment of the nucleus critical size, within the induction time t_i.[48] Thus, $\Delta\sigma$ can be obtained from the variation of the nucleation rate I with crystallization temperature by determining the product $\sigma\sigma_e\Delta\sigma$:

$$I = I_0 exp\left(-\frac{U^*}{R(T-T_\infty)}\right) exp\left(-\frac{16\sigma\sigma_e\Delta\sigma T_m^2}{kTf^2\Delta T^2\Delta h_0^2}\right) \quad (4.6)$$

where I_0 is a temperature-independent frequency term, and the other symbols have been previously defined.

By plotting $lnI+U^*/R(T-T_\infty)$ versus $1/T(\Delta Tf)^2$, a linear fitting can be obtained and the slope (K_i) of the line is proportional to $\sigma\sigma_e\Delta\sigma$. In order to determine $\Delta\sigma$, one also needs to measure the growth rate at different crystallization temperatures and determine the value of the $\sigma\sigma_e$ product from its temperature variation. In fact, according to L-H growth model (equation (4.1)), a plot of $lnG+U^*/R(T-T_\infty)$ versus $1/T\Delta Tf$ yields a straight line with a slope K_g, proportional to $\sigma\sigma_e$. From these two separate sets of experiments, $\Delta\sigma$ is obtained. Assuming from the literature an activation energy U^* of 6.28 kJ/mol, a bulk enthalpy of fusion Δh_0 of the Form II of 56 J/cm^3 and a molecular stem width b_0 of 7.45×10^{-8} cm,[49] three very close values of the term $\sigma\sigma_e$ has been calculated for cross-nucleation on spherulitic, hedritic and fibrous Form I seeds: 56.07, 56.63 and 53.41 erg^2 cm^{-4}, respectively.

However, as mentioned earlier, the nucleation density could not be easily counted when transcrystallization was formed at the substrate boundary in composites with very high nucleating efficiency, as in the case of PE/PE composites.[48] Thus, nucleation induction time data were used, under the assumption that the product between nucleation rate and induction time at a given temperature is constant:

$$I(T)t_i(T) = Constant \quad (4.7)$$

Therefore, by relating the nucleation rate and the induction time an efficient way to obtain $\Delta\sigma$ is provided.

In Figure 4.7 Ishida's model is applied to the measured cross-nucleation induction times for PB-1 nucleated onto different Form I seeds. A good linearity of the data is observed, allowing us to perform a linear fitting and derive the slope K_i, that is. calculate the quantity $\sigma\sigma_e\Delta\sigma$. Combining it with the $\sigma\sigma_e$ calculated from K_g obtained from the Lauritzen–Hoffman plot (Appendix A5), an estimate of $\Delta\sigma$ for the spherulite, the hedrite and the fiber substrate can be derived: 0.294, 0.301 and 0.291 erg cm^{-2}, respectively.

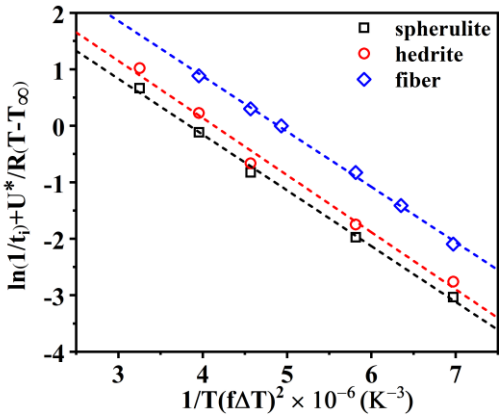

Figure 4.7 Plot of $ln(1/t_i)+U^*/R(T-T_\infty)$ versus $1/T(\Delta Tf)^2$ for nucleation of PB-1 Form II on various Form I seeds.

As judging from the obtained values, the model of Ishida is not capable of capturing significant differences between the nucleating efficiency of the different substrates. In fact, the lines of Figure 4.7 are practically parallel to each other, indicating that the same cross-nucleation barrier would be obtained for the different Form I seeds. Clearly this conclusion cannot account for the differences experimentally observed in the induction time values of each system, given the negligible difference in the growth rate.

On the other hand, a more detailed model for the heterogeneous nucleation was proposed by Muchova et al. It consisted in the sum of two qualitatively different steps for the formation of critical nucleus:[47, 50] the formation of the first layer of segments on the foreign substance, that occurs within a time t_h, and the formation of further layers until the growth of a nucleus of critical size is completed, within a time t_s. Thus, the overall induction time of the process is given by the sum of these two individual steps, that is, $t_i = t_h + t_s$. The two components of the induction time can be expressed by these relations:

$$t_h = A_1 exp\left(\frac{16\sigma\sigma_e\Delta\sigma T_m^2}{kTf^2\Delta T^2\Delta h_0^2}\right) exp\left(\frac{U^*}{R(T-T_\infty)}\right) \tag{4.8}$$

$$t_s = A_2\left(\frac{2\Delta\sigma T_m}{\Delta h_0\Delta T b_0}\right) exp\left(\frac{4\sigma\sigma_e b_0 T_m}{kT\Delta h_0 f\Delta T}\right) exp\left(\frac{U^*}{R(T-T_\infty)}\right) \tag{4.9}$$

where A_1 and A_2 are proportionality constants. It should be noted that t_h describe exactly Ishida's model.

It is known that the size of the critical nuclei increases with crystallization temperature. At high temperatures of crystallization, the number of the folding segment layers is considerable, and the time of the formation of the first layer (t_h) becomes negligible in

comparison with the time in which further layers are formed. In this case, equation $t_i = t_h + t_s$ for the induction time can be simplified to $t_i \approx t_s$, and the equation of the induction time can be rewritten into a logarithmic form:

$$ln(t_i \Delta T) - \frac{U^*}{R(T - T_\infty)} = ln\left(\frac{C \Delta\sigma T_m}{\Delta h_0 b_0}\right) + \frac{4\sigma\sigma_e b_0 T_m}{k \Delta h_0} \frac{1}{Tf\Delta T} \quad (4.10)$$

where the influence of the transport term is included in the constant C. According to equation (4.10), the dependence of $ln(t_i\Delta T)\text{-}U^*/R(T\text{-}T_\infty)$ on $1/Tf\Delta T$ is a straight line with intercept Q on the y-axis, equals to:

$$Q = ln\left(\frac{C \Delta\sigma T_m}{\Delta h_0 b_0}\right) \quad (4.11)$$

As can be noticed, Q includes the interfacial free energy difference ($\Delta\sigma$).

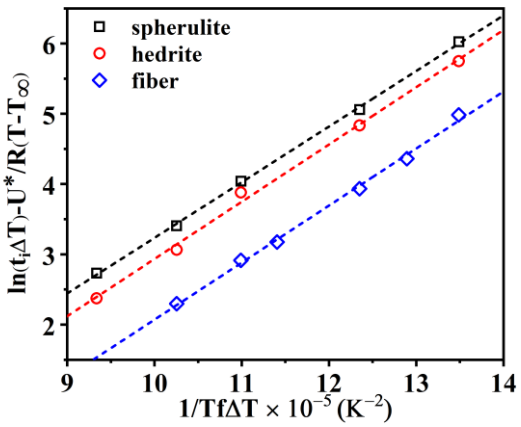

Figure 4.8 Plot of $ln(t_i\Delta T)\text{-}U^*/R(T\text{-}T_\infty)$ vs $1/T\Delta Tf$, according to Muchova's model at high temperatures, for cross-nucleation of PB-1 Form II on different Form I seeds.

Figure 4.8 shows the evolution of $ln(t_i\Delta T)\text{-}U^*/R(T\text{-}T_\infty)$ as a function of $1/Tf\Delta T$ for PB-1 matrix crystallized in contact with Form I seeds with different morphologies. The analysis of the cross-nucleation induction time data with a model which expresses the nucleation barrier taking into account the formation of several crystalline layers, up to the attainment of critical dimensions, can correctly capture the different nucleating ability of the various substrates. In fact, the lines display a different intercept with the y-axis, given by different $\Delta\sigma$. However, its absolute value cannot be obtained due to the unknown constant C.

Therefore, in order to correctly quantify the nucleating activity of each substrate, a new approach, consisting in the use of the sum of equations (4.8) and (4.9) to fit the experimental induction time data, is required. In this way a better identification of the crystallization

temperature window in which each one of Muchova's models (t_h and t_s) is valid, can be obtained. The model describing the total induction time as the sum of the individual steps is referred as "detailed model" in the following.

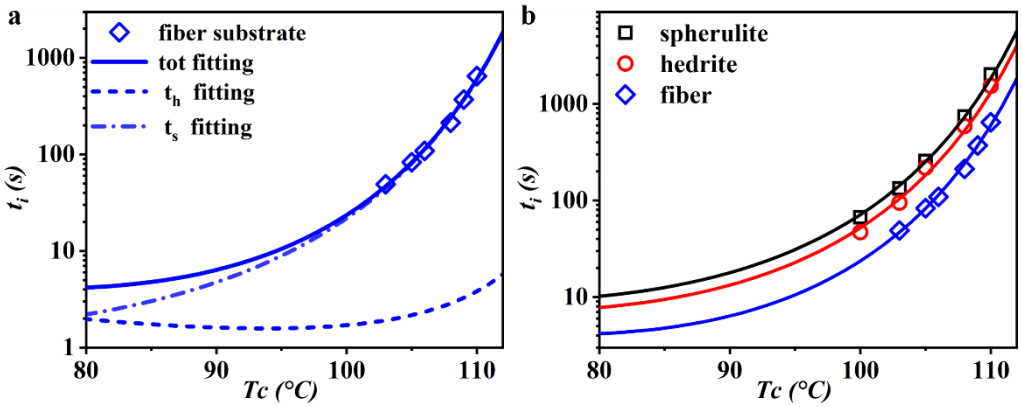

Figure 4.9 (a) Selected induction time data of fiber Form I substrate and corresponding fitting according to the detailed (total time) model. The dashed curves represent the contributions of the first and further layers formation (t_h and t_s models). (b) Plot of the induction time data as a function of crystallization temperature for the different Form I seeds with varying morphology, together with the functions obtained from the fitting of the detailed model for the induction time.

Indeed, the description of the total induction time by the detailed model allows us to estimate in which range of temperature each step is dominant and what is its exact contribution to the overall induction time at a given crystallization temperature. In Figure 4.9a and Appendix A7, the contributions of first and further layers models to the detailed model are shown for PB-1 with Form I fiber seed. It is clear that the contribution of the further layer model (t_s) is much larger than that of the first layer model (t_h) at higher temperatures (> 100 °C). This means that the data in the test temperature range follow very closely the trend described by the t_s model alone, that is, the rate determining step in the attainment of the nucleus critical size is the addition of several crystalline layers. On the contrary, for lower crystallization temperatures (< 87 °C), the formation of the first crystalline layer is enough for the nucleus to attain the critical size.

Figure 4.9b shows the curves obtained by fitting the experimental induction time data with the detailed model equation for the three PB-1 Form I substrates. The parameter A_1 from equation (4.8) was obtained using crystallization induction time data of bulk PB-1, given that nucleation is likely controlled by the formation of the first layer onto substrates of low

nucleation efficiency and at high undercooling.[41] A value of 0.005 s could be determined and used in the subsequent fit of the data of interest for all the substrates. The resulting values of the unknown parameters from the sum of equations (4.8) and (4.9) (A_2, $\Delta\sigma_{spherulite}$, $\Delta\sigma_{hedrite}$ *and* $\Delta\sigma_{fiber}$) are 0.002 s, 0.295 erg cm^{-2}, 0.225 erg cm^{-2} and 0.105 erg cm^{-2}, respectively. Therefore, the $\Delta\sigma$ values obtained for the three substrates agree with the experimental trend of nucleation kinetics.

Given the results discussed above, it can be concluded that the kinetic of nucleation cannot be estimated by modeling a single step only, but rather by considering the two steps simultaneously. Appendix A8 shows the plot of the curves relative to the first layer model (t_h) and the further layer model (t_s) obtained during the fitting of the detailed model for the different Form I seeds with varying morphologies. Within the range of experimental temperature, the differences between t_h and t_s curves at the same crystallization temperature increases in the order: fiber > hedrite > spherulite. This order mirrors the influence of the formation of the first crystalline layer on the nucleation barrier, that is, the lower the $\Delta\sigma$, the less important becomes the first step in determining the overall induction time. In view of interpreting the observed effect of seed's morphology on cross-nucleation it is worth to briefly consider the absolute values of the obtained free energy difference parameters. For all the considered substrates, extremely low values of $\Delta\sigma$ were found, in comparison to the systems for which most of the literature data are available, that is, polymer/fiber composites, with values ranging from 4 to 20 erg cm^{-2}.[42, 51] On the other hand, such low values are comparable to those obtained in particular cases, such as those of ultrahigh molecular weight polyethylene fibers in polyethylene or polycaprolactone matrices,[48, 52] for which epitaxial nucleation is obvious or well known.[53] Thus, particularly favorable interactions between crystallizing Form II and Form I seeds must be in place. It is conceivable that cross-nucleation in PB-1 is governed by either "true" crystallographic epitaxy between the two structures, or at least by a "soft epitaxy" mechanism related to a matching between the topographical details of parent and daughter crystals at the nanoscale.

4.4 Discussions

Through the above study of the cross-nucleation of PB-1 Form II on Form I substrates, it has been shown that the nucleation activities are significantly affected by the substrate type of seed. Given that all the substrates and the crystallizing polymer have exactly the same chemistry, the different nucleating efficiencies should be attributed to peculiar physical

interactions rather than chemical ones. The crystalline substrate possesses a multi length-scale structure ranging from molecular to mesoscopic scale. It is not yet clear which one of these length scales has the largest impact on cross-nucleation.

In most cases of nucleation induced by the presence of solid fibers in composites, the fiber surface topography was proposed to have a determining role in nucleation kinetics. This was mainly attributed to two reasons. On one hand, thermal stresses from temperature change at the coarser fiber interface might induce local orientation of polymer chain segments, providing efficient seeds for nucleation. With respect to the smooth surface, such thermal stresses are expected to be larger at deep "valleys".[54] On the other hand, for forming a viable nucleus, the free-energy barrier is always larger on a flat surface than that in a groove, due to the possibility of secondary or tertiary nucleation.[42] In the present case, the surface topography of the used seeds with different morphologies is not easily accessible, especially for spherulitic and hedritic seeds, since they are embedded in the crystallizing PB-1 itself. Furthermore, it is difficult to explain the effect of surface topography on the nucleation by considering the degree of roughness alone.[51] Dalnoki-Veress et al.[55] studied the role of the interface in inducing crystal nucleation by using isotactic polystyrene (i-PS) as a substrate for crystallizing PEO droplets. They found a larger surface roughness and a higher nucleation temperature for i-PS film isothermally crystallized at 175 °C with respect to the same film crystallized at 185 °C. However, these results are not in agreement with the ones presented hereby, since cross-nucleation kinetic onto Form I spherulite, formed during isothermal crystallization at 90°C, is slower than that on Form I hedrite (isothermally crystallized at 108°C). Therefore, assuming a similar dependence of the crystalline seed roughness in the two cases, other different factors should be considered in order to explain the cross-nucleation efficiency of the different PB-1 Form I substrates.

On the other hand, the role of molecular epitaxy should not be overlooked. For instance, Damman et al.[56] showed that molecular epitaxy played a greater role in the enhancement of nucleation of a small molecule, in comparison to surface topography. In the case of cross-nucleation between polymorphs, the role of epitaxy is controversial. For example, in the solution crystallization of a steroid, cross-nucleation of the metastable polymorph on the stable one can occur both with and without preferred mutual orientation between the two structures, depending on the solvent mixture.[57, 58] In polymers, cross-nucleation of the monoclinic phase on trigonal crystals via epitaxial mechanism has been highlighted in single crystals,[59] but not in melt-crystallization.[60, 61] Focusing on the cross-nucleation of PB-1 Form II on Form I, the existence of a specific epitaxial relationship between the two polymorphs has not

been disclosed yet.

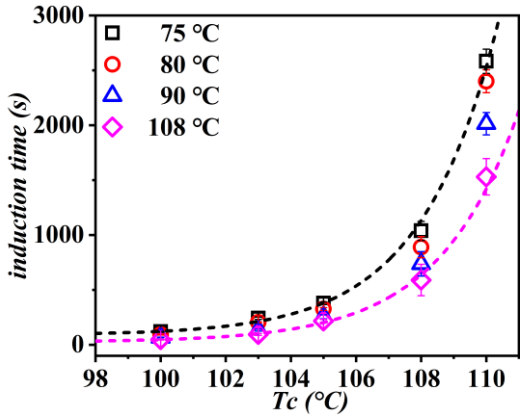

Figure 4.10 Induction time for Form II on Form I cross-nucleation as a function of T_c for the spherulitic Form I seeds crystallized at different temperatures.

For the sake of the following discussion, we assume that a preferred mutual orientation of the chains in the two structures (PB-1 Form I and Form II) must exist at the cross-nucleation point. This can result from a strict crystallographic epitaxy or from a more general "soft epitaxy" mechanism. Several cases of epitaxy between semicrystalline polymers have been studied in the literature.[62, 63] It has been recognized that, since the crystalline substrate has itself a lamellar morphology, the requirement of lattice match between the two structures is not enough to allow the occurrence of epitaxy. In fact, because of the limited dimensions of the substrate crystals, a matching between the lamellar sizes of the two polymers must also exist.[64] A paradigmatic example of this constraint is found in the system isotactic polypropylene/polyethylene. Epitaxy of the crystallizing polyethylene onto the semicrystalline polypropylene substrate can only occur for crystallization temperatures below 123 °C.[65, 66] Therefore, it is of interest to test the possible dependence of PB-1 Form II cross-nucleation kinetics on the lamellar thickness of Form I seeds. Figure 4.10 shows the induction time of cross-nucleation for Form II on spherulitic Form I seeds originally crystallized at different temperatures, as a function of the cross-nucleation temperature. Data for the hedritic morphology (sample crystallized at 108 °C) are included as well. As can be seen, the induction time clearly decreases, and thus the efficiency of cross-nucleation increases, with increasing the spherulite substrate preparation temperature, in the whole range of explored supercooling. Since it is generally known that lamellar thickness is proportional to the crystallization temperature, it can be deduced that the nucleating ability of the substrates depends on the Form I seed's lamellar thickness, rather than on the specific orientation of the Form I lamellae (edge

on vs. flat on in spherulitic or hedritic seeds, respectively).

Given the above findings and the apparent analogy between polymer-polymer epitaxy and cross-nucleation, we can tentatively interpret the effect of seed morphology on nucleation on the basis of the "template model" proposed by Philips and colleagues to link epitaxy and secondary nucleation.[64] In this model, the author recognized that for the epitaxial deposition of a polymer onto another one, the crystal dimension of the substrate in the direction characteristic of the lattice match must be larger than the critical stem length of the crystallizing polymer's secondary nucleus. The proposed scheme is adapted to the present case of PB-1, as sketched in Figure 4.11.

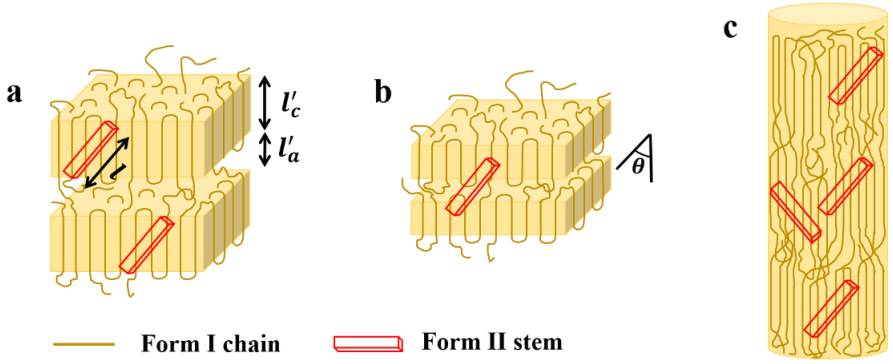

Figure 4.11 Schematic illustration of the cross-nucleation of PB-1 Form II on the surface of (a) hedritic, (b) spherulitic and (c) fibrous Form I substrates. For the sake of clarity, the flat-on (hedrite) and edge-on (spehrulite) lamellae are both represented with the chain axis in the vertical direction. l'_c and l'_a represent the thicknesses of the crystalline lamella and of the amorphous layer, respectively.

Considering a given crystallization temperature, the critical stem length of the Form II secondary nucleus is indicated as l, while the generic Form I seed is characterized by a crystalline lamellar thickness and amorphous layer thickness l'_c and l'_a, respectively. The deposition of Form II stems occurs at an angle θ with respect to the lamellar normal of the Form I substrate crystal, as dictated by the epitaxial lattice matching (unknown at present). Therefore, it is possible to infer variations in the free energy barrier for cross-nucleation on different substrates, by comparing the magnitude of l'_c and l in the lattice matching direction, depending on seed's formation temperature and actual crystallization temperature.

Given the defined angle between the polymorphs' chain directions, the maximum parent crystal dimension available is $l'_c/\cos(\theta)$. If the critical stem length of Form II at the

crystallization temperature is shorter than $l_c'/\cos(\theta)$, a nucleus is easily generated onto the surfaces of Form I crystalline substrate. This is certainly valid for the hedritic morphology (Figure 4.11a), since the seed is originally crystallized at 108 °C, at the high end of the investigated cross-nucleation temperature range (100-110 °C). Thus, the lamellar thickness of the Form I seed is expected to be typically larger than the critical stem length of the cross-nucleating Form II.

On the contrary, when l is larger than $l_c'/\cos(\theta)$, a portion of the deposited macromolecular chain segment will lay on the amorphous phase. For that part of the nucleus, no decrease in free energy associated with the formation of the related crystal volume is expected, while a lateral surface free energy penalty is still generated. This implies that the nucleation energy barrier will be increased by an amount proportional to $(l - l_c'/\cos(\theta))$, and up to a maximum value proportional to $(l - l_a'/\cos(\theta))$ when the secondary nucleus is formed on two adjacent lamellae of the seed.[64] This condition is likely to be encountered in the case of the spherulitic Form I seed, since the parent polymorph lamellar thickness is smaller than that of cross-nucleating Form II crystals (Figure 4.11b). This is because the temperature used to prepare the spherulitic substrates ranges between 75 and 90 °C, at least from 10 to 20 °C lower than the temperatures used for the cross-nucleation experiments. Therefore, the kinetics of cross-nucleation on the surface of spherulitic Form I substrate is slower with respect to the one on the hedrite, due to the higher nucleation energy barrier., Furthermore, within the spherulitic seeds crystallized at different temperatures, the increase in nucleation barrier due to mismatch between From II and Form I lamellae will be the highest for the lowest seed's lamellar thickness.

While this model is rather intuitively applicable when both the parent and daughter polymorphs exhibit a lamellar structure, such as in the case of PB-1 Form II spherulites nucleating on Form I spherulites or hedrites, the situation is not straightforward for the cross-nucleation on the Form I fibrous seeds. In fact, semicrystalline fibers are composed of several long fibrils constituted of smaller oriented crystallites interconnected via tie-chain in the amorphous phase (Figure 4.11c). The size of these crystalline blocks along the polymer chain direction might be comparable to the lamellar thickness of the hedrite sample, as judged by the similar melting temperatures recorded by differential scanning calorimetry (see Appendix A9). However, under the assumption that the same cross-nucleation model would indifferently apply to both morphologies, it must be deduced that the specific arrangement of crystalline and amorphous Form I chains at the nanoscale in the fiber sample is more favorable to cross-

nucleation. We can speculate that the very similar lamellar thickness between the crystallizing Form II and the hedritic Form I seed would still result in a certain energy penalty to the nucleus formation, due to the high probability of Form II stem deposition onto the chain folding region. On the other hand, the lack of perfect lateral correlation between the crystallite position in the fibers likely ensue the availability of a larger Form I crystalline substrate along the matching direction with the cross-nucleating Form II (as schematized in Figure 4.11c). Moreover, the preferential extended chain polymer conformation in the fibrillar crystals, with a reduced presence of chain folds at the lamellar edges, might possibly cause a less severe energy penalty for the depositing Form II stem, with respect to the hedritic chain folded morphology.

In conclusion, the cross-nucleation of PB-1 Form II onto Form I substrates must involve the necessary requirements for the formation of a Form II secondary nucleus of critical size. The differences in cross-nucleation rate among the seeds with different morphologies can be ascribed to the different crystal dimensions of the Form I substrates in comparison to the lamellar thickness of the nucleated Form II, projected along a certain direction. This mechanism has been rigorously applied in the literature[65, 66] to the epitaxy between different polymer pairs. This result suggests that it might also describe the case of PB-1 cross-nucleation, although a detailed epitaxial relationship between Form I and Form II is still not known.

4.5 Conclusion

In the present work, the cross-nucleation behavior of Form II on seeds of Form I possessing different morphologies was investigated. It was found that the cross-nucleation ability of Form I seeds toward Form II varies with substrates. In particular, the cross-nucleation efficiency decreases in the order: fiber > hedrite > spherulite. Based on a quantitative analysis of the induction time, the cross-nucleation energy barrier was successfully determined, revealing that the rate determining step in the attainment of the nucleus critical size for cross-nucleation is the addition of several crystalline layers, rather than the formation of the first crystalline layer on the substrate. The observed different cross-nucleation efficiencies of the seeds are attributed to differences in the Form I lamellar thickness, and to its mismatch with the Form II cross-nucleus critical size. This is in agreement with a previously developed model which describes polymer-polymer epitaxy and suggests that a defined mutual orientation between the two polymorphs' structures might be required at the cross-nucleation point.

References

[1] F. Danusso, Macromolecular polymorphism and stereoregular synthetic polymers, Polymer 8 (1967) 281-320.

[2] P. Pan, Y. Inoue, Polymorphism and isomorphism in biodegradable polyesters, Progress in Polymer Science 34(7) (2009) 605-640.

[3] A. Halperin, M. Tirrell, T. Lodge, Macromolecules: Synthesis, Order and Advanced Properties, Advances in Polymer Science 100, Springer 1992.

[4] A.T. Jones, J.M. Aizlewood, D. Beckett, Crystalline forms of isotactic polypropylene, Die Makromolekulare Chemie: Macromolecular Chemistry and Physics 75(1) (1964) 134-158.

[5] S. Brückner, S.V. Meille, V. Petraccone, B. Pirozzi, Polymorphism in isotactic polypropylene, Progress in Polymer Science 16(2-3) (1991) 361-404.

[6] B. Lotz, J. Wittmann, A. Lovinger, Structure and morphology of poly (propylenes): a molecular analysis, Polymer 37(22) (1996) 4979-4992.

[7] D. Cavallo, G.C. Alfonso, Concomitant crystallization and cross-nucleation in polymorphic polymers, Polymer Crystallization II, Springer 2015.

[8] S. Chen, H. Xi, L. Yu, Cross-nucleation between ROY polymorphs, Journal of the American Chemical Society 127(49) (2005) 17439-17444.

[9] C. Desgranges, J. Delhommelle, Molecular mechanism for the cross-nucleation between polymorphs, Journal of the American Chemical Society 128(32) (2006) 10368-10369.

[10] L. Yu, Nucleation of one polymorph by another, Journal of the American Chemical Society 125(21) (2003) 6380-6381.

[11] J. Tao, K.J. Jones, L. Yu, Cross-nucleation between D-mannitol polymorphs in seeded crystallization, Crystal growth & design 7(12) (2007) 2410-2414.

[12] Y. Nozue, S. Seno, T. Nagamatsu, S. Hosoda, Y. Shinohara, Y. Amemiya, E. Berda, G. Rojas, K. Wagener, Cross nucleation in polyethylene with precisely spaced ethyl branches, ACS Macro Letters 1(6) (2012) 772-775.

[13] C. Wang, Y.J. Wu, C.Y. Fang, C.W. Tsai, Electrospun nanofiber-reinforced polypropylene composites: nucleating ability of nanofibers, Composites Science and Technology 126 (2016) 1-8.

[14] C. Wang, L. Hwang, Transcrystallization of PTFE fiber/PP composites (I) crystallization kinetics and morphology, Journal of Polymer Science Part B: Polymer Physics 34(1) (1996) 47-56.

[15] C. Wang, C. Liu, Transcrystallization of polypropylene on carbon fibres, Polymer 38(18)

(1997) 4715-4718.

[16] T. Urushihara, K. Okada, K. Watanabe, A. Toda, N. Kawamoto, M. Hikosaka, Acceleration mechanism in critical nucleation of polymers by epitaxy of nucleating agent, Polymer journal 41(3) (2009) 228.

[17] D. Cavallo, F. Galli, L. Yu, G.C. Alfonso, Cross-Nucleation between Concomitantly Crystallizing α-and γ-Phases in Polypivalolactone: Secondary Nucleation of One Polymorph on Another, Crystal growth & design 17(5) (2017) 2639-2645.

[18] D. Cavallo, L. Gardella, G. Portale, A.J. Müller, G.C. Alfonso, Kinetics of cross-nucleation in isotactic poly (1-butene), Macromolecules 47(2) (2014) 870-873.

[19] J. Tao, L. Yu, Kinetics of cross-nucleation between polymorphs, The Journal of Physical Chemistry B 110(14) (2006) 7098-7101.

[20] S. Looijmans, A. Menyhard, G.W. Peters, G.C. Alfonso, D. Cavallo, Anomalous temperature dependence of isotactic polypropylene α-on-β cross-nucleation kinetics, Crystal growth & design 17(9) (2017) 4936-4943.

[21] G. Natta, P. Pino, P. Corradini, F. Danusso, E. Mantica, G. Mazzanti, G. Moraglio, Crystalline high polymers of α-olefins, Journal of the American Chemical Society 77(6) (1955) 1708-1710.

[22] R. Xin, J. Zhang, X. Sun, H. Li, Z. Ren, S. Yan, Polymorphic behavior and phase transition of poly (1-butene) and its copolymers, Polymers 10(5) (2018) 556.

[23] A.T. Jones, Polybutene-1–type II crystalline form, Journal of Polymer Science Part B: Polymer Letters 1(8) (1963) 455-456.

[24] V. Holland, R.L. Miller, Isotactic polybutene-1 single crystals: morphology, Journal of Applied Physics 35(11) (1964) 3241-3248.

[25] K. Tashiro, J. Hu, H. Wang, M. Hanesaka, A. Saiani, Refinement of the crystal structures of forms I and II of isotactic polybutene-1 and a proposal of phase transition mechanism between them, Macromolecules 49(4) (2016) 1392-1404.

[26] F. Danusso, G. Gianotti, Isotactic polybutene-1: Formation and transformation of modification 2, Die Makromolekulare Chemie: Macromolecular Chemistry and Physics 88(1) (1965) 149-158.

[27] A. Woodward, D. Morrow, Annealing of polybutene-1 single crystals, Journal of Polymer Science Part A-2: Polymer Physics 6(12) (1968) 1987-1997.

[28] Z. Wang, X. Dong, G. Liu, Q. Xing, D. Cavallo, Q. Jiang, A.J. Müller, D. Wang, Interfacial nucleation in iPP/PB-1 blends promotes the formation of polybutene-1 trigonal crystals, Polymer 138 (2018) 396-406.

[29] I. Stolte, R. Androsch, Comparative study of the kinetics of non-isothermal melt solidification of random copolymers of butene-1 with either ethylene or propylene, Colloid and Polymer Science 292(7) (2014) 1639-1647.

[30] I. Stolte, D. Cavallo, G.C. Alfonso, G. Portale, M. van Drongelen, R. Androsch, Form I′ crystal formation in random butene-1/propylene copolymers as revealed by real-time X-ray scattering using synchrotron radiation and fast scanning chip calorimetry, European polymer journal 60 (2014) 22-32.

[31] I. Stolte, M. Fischer, R. Roth, S. Borreck, R. Androsch, Morphology of form I′ crystals of polybutene-1 formed on melt-crystallization, Polymer 63 (2015) 30-33.

[32] W. Wang, L. Zheng, L. Liu, W. Li, Y. Li, Z. Ma, Stretching behavior of the butene-1/ethylene random copolymer: A direct correspondence between triggering of II-I phase transition and mechanical yielding, Polymer Crystallization 2(2) (2019) e10052.

[33] L. Zheng, L. Liu, C. Shao, W. Wang, B. Wang, L. Pan, Y. Li, Z. Ma, Phase transition from tetragonal form II to hexagonal form I of butene-1/4-methyl-1-pentene random copolymers: Molecular factor versus stretching stimuli, Macromolecules 52(3) (2019) 1188-1199.

[34] W. Wang, C. Shao, L. Zheng, B. Wang, L. Pan, G. Ma, Y. Li, Y. Wang, C. Liu, Z. Ma, Stretching-induced phase transition of the butene-1/ethylene random copolymer: Orientation and kinetics, Journal of Polymer Science Part B: Polymer Physics 57(2) (2019) 116-126.

[35] F. Azzurri, A. Flores, G. Alfonso, F. Baltá Calleja, Polymorphism of isotactic poly (1-butene) as revealed by microindentation hardness. 1. Kinetics of the transformation, Macromolecules 35(24) (2002) 9069-9073.

[36] Y.-t. Wang, P.-r. Liu, Y. Lu, Y.-f. Men, Mechanism of polymorph selection during crystallization of random butene-1/ethylene copolymer, Chinese Journal of Polymer Science 34(8) (2016) 1014-1020.

[37] Y. Qiao, Q. Wang, Y. Men, Kinetics of nucleation and growth of form II to I polymorphic transition in polybutene-1 as revealed by stepwise annealing, Macromolecules 49(14) (2016) 5126-5136.

[38] D. Cavallo, L. Gardella, G. Portale, A.J. Müller, G.C. Alfonso, On cross-and self-nucleation in seeded crystallization of isotactic poly (1-butene), Polymer 54(17) (2013) 4637-4644.

[39] Q. Fu, B. Heck, G. Strobl, Y. Thomann, A temperature-and molar mass-dependent change in the crystallization mechanism of poly (1-butene): Transition from chain-folded to chain-extended crystallization?, Macromolecules 34(8) (2001) 2502-2511.

[40] B. Wang, A. Menyhard, G.C. Alfonso, A.J. Müller, D. Cavallo, Differential scanning

calorimetry study of cross-nucleation between polymorphs in isotactic poly (1-butene), Polymer International 68(2) (2019) 257-262.

[41] E. Carmeli, B. Wang, P. Moretti, D. Tranchida, D. Cavallo, Estimating the Nucleation Ability of Various Surfaces Towards Isotactic Polypropylene via Light Intensity Induction Time Measurements, Entropy 21(11) (2019) 1068.

[42] C. Wang, F.H. Liu, W.H. Huang, Electrospun-fiber induced transcrystallization of isotactic polypropylene matrix, Polymer 52(5) (2011) 1326-1336.

[43] C. Wang, C.Y. Fang, C.Y. Wang, Electrospun poly (butylene terephthalate) fibers: Entanglement density effect on fiber diameter and fiber nucleating ability towards isotactic polypropylene, Polymer 72 (2015) 21-29.

[44] B. Wunderlich, Macromolecular Physics, Volume 2: Crystal nucleation, growth, annealing, Academic press 1973.

[45] F. Azzurri, G.C. Alfonso, Lifetime of shear-induced crystal nucleation precursors, Macromolecules 38(5) (2005) 1723-1728.

[46] B. Monasse, J.M. Haudin, Morphologies and regimes of growth of polybutene crystals in phase II, Makromolekulare Chemie. Macromolecular Symposia, Wiley Online Library 1988.

[47] M. Muchova, F. Lednický, Induction time as a measure for heterogeneous spherulite nucleation: Quantitative evaluation of early-stage growth kinetics, Journal of Macromolecular Science, Part B: Physics 34(1-2) (1995) 55-73.

[48] H. Ishida, P. Bussi, Induction time approach to surface induced crystallization in polyethylene/poly (ε-caprolactone) melt, Journal of Materials Science 26(23) (1991) 6373-6382.

[49] I. Stolte, R. Androsch, M.L. Di Lorenzo, Spherulite growth rate and fold surface free energy of the form II mesophase in isotactic polybutene-1 and random butene-1/ethylene copolymers, Colloid and Polymer Science 292(6) (2014) 1479-1485.

[50] M. Muchova, F. Lednický, Investigation of heterogeneous nucleation by the induction time of crystallization: 2. Comparison of the theory and experimental measurement, Polymer 37(14) (1996) 3037-3043.

[51] B. Wang, T. Wen, X. Zhang, A. Tercjak, X. Dong, A.J. Müller, D. Wang, D. Cavallo, Nucleation of Poly (lactide) on the Surface of Different Fibers, Macromolecules 52(16) (2019) 6274-6284.

[52] H. Ishida, P. Bussi, Surface induced crystallization in ultrahigh-modulus polyethylene fiber-reinforced polyethylene composites, Macromolecules 24(12) (1991) 3569-3577.

[53] H. Chang, J. Zhang, L. Li, Z. Wang, C. Yang, I. Takahashi, Y. Ozaki, S. Yan, A study on

the epitaxial ordering process of the polycaprolactone on the highly oriented polyethylene substrate, Macromolecules 43(1) (2009) 362-366.

[54] C. Wang, C.R. Liu, Transcrystallization of polypropylene composites: nucleating ability of fibres, Polymer 40(2) (1999) 289-298.

[55] J.L. Carvalho, K. Dalnoki-Veress, Homogeneous bulk, surface, and edge nucleation in crystalline nanodroplets, Physical review letters 105(23) (2010) 237801.

[56] P. Damman, S. Coppée, V.M. Geskin, R. Lazzaroni, What is the mechanism of oriented crystal growth on rubbed polymer substrates? Topography vs epitaxy, Journal of the American Chemical Society 124(51) (2002) 15166-15167.

[57] C. Stoica, P. Tinnemans, H. Meekes, E. Vlieg, P. Van Hoof, F. Kaspersen, Epitaxial 2D nucleation of metastable polymorphs: A 2D version of Ostwald's rule of stages, Crystal growth & design 5(3) (2005) 975-981.

[58] C. Stoica, P. Verwer, H. Meekes, E. Vlieg, P. Van Hoof, F. Kaspersen, Heterogeneous 2D nucleation of the stable polymorphic form on the metastable form, Journal of Crystal Growth 275(12) (2005) e1727-e1731.

[59] B. Lotz, α and β phases of isotactic polypropylene: a case of growth kineticsphase reentrency'in polymer crystallization, Polymer 39(19) (1998) 4561-4567.

[60] H. Li, X. Sun, S. Yan, J.M. Schultz, Initial stage of iPP β to α growth transition induced by stepwise crystallization, Macromolecules 41(13) (2008) 5062-5064.

[61] J. Wang, Z. Ren, X. Sun, H. Li, S. Yan, The βα growth transition of isotactic polypropylene during stepwise crystallization at elevated temperature, Colloid and Polymer Science 293(10) (2015) 2823-2830.

[62] A. Thierry, B. Lotz, Epitaxial crystallization of polymers: Means and issues, John Wiley & Sons2013.

[63] R. Xin, J. Zhang, X. Sun, H. Li, Z. Qiu, S. Yan, Epitaxial effects on polymer crystallization, Polymer Crystallization II, Springer 2015.

[64] A.J. Greso, P.J. Phillips, The role of secondary nucleation in epitaxial growth: the template model, Polymer 35(16) (1994) 3373-3376.

[65] S. Yan, D. Yang, J. Petermann, Controlling factors for the occurrence of heteroepitaxy of polyethylene on highly oriented isotactic polypropylene, Polymer 39(19) (1998) 4569-4578.

[66] J. Petermann, Y. Xu, The origin of heteroepitaxy in the system of uniaxially oriented isotactic polypropylene and polyethylene, Journal of Materials Science 26(5) (1991) 1211-1215.

Chapter 5. Evidence of epitaxy for polybutene-1 cross-nucleation in seeded crystallization

5.1 Introduction

Crystallization, both in small molecules and polymers, generally proceeds by two consecutive events, that is, nucleation and crystal growth.[1-4] The nucleation is the process of generation of a new phase, and it can be categorized as homogeneous, when it occurs in the bulk of the mother phase, or heterogeneous in the presence of foreign surfaces.[5-7] Epitaxy, a special form of heterogeneous nucleation, occurs when a crystal nucleates on top of the surface of another crystal, according to strictly defined mutual crystallographic orientations. [3, 8, 9] When restrictive relationships of the crystallographic arrangement between the substrate and the depositing molecule exist, the epitaxially nucleated crystal will show some specific crystal structure and orientation,[8] resulting in particular properties and crystalline morphologies.[10-15] In polymers, epitaxial crystallization is extensively documented both on solid substrates and between two polymers with different chemical structures, and it is used in order to obtain desired modifications or molecular chain orientations.[3, 12, 13, 16-23]

Most of the small organic molecules are likely to form polymorphs, whose crystallization is often not easy to control due to the relatively weak and nondirectional intermolecular interactions in the solid state.[24] Thus, cross-nucleation, that is, the nucleation of one polymorph on another (thus occurring within the same substance), is quite frequently encountered in these systems. Epitaxy has been shown to play a role in cross-nucleation of several, but not all, molecular crystal polymorphs.[8, 25-29] For example, Park et al. discovered that a new metastable packing polymorph (K) of donepezil can be obtained by epitaxial growth on substrate crystals of the more stable form F.[29]

Although cross-nucleation is encountered in several polymorphic polymers as well,[30-36] whether epitaxy plays a prominent part in it is still unclear. The case of isotactic polypropylene is emblematic, because an epitaxial relationship for α-phase single crystals nucleating at the surface of a β-phase crystal has been proposed by Lotz,[37] but it has been shown not to hold in bulk samples.[38]

Of particular interest, also for its cross-nucleation behavior, is polybutene-1, which exhibits pronounced polymorphism that can be distinguished by the chain conformation and

packing mode of chain stems.[39] Different helical conformations, that is, the 3/1, 11/3, and 4/1 helixes, can pack into trigonal (Form I), tetragonal (Form II), and orthorhombic (Form III) unit cells.[40, 41] Among them, the Form I unit cell parameters are a = b = 17.5 Å, c (chain axis) = 6.477 Å, and γ = 120° (with space group $P\bar{3}$), while Form II exhibits a tetragonal unit cell with the parameters a = b = 14.9 Å and c = 21.3 Å (with space group $P\bar{4}b2$).[42-44]

Our previous work (see Chapter 4) has revealed that the cross-nucleation efficiency of Form II on Form I substrates increases with the thickening of Form I lamellae, a fact that was interpreted as a possible hint of an epitaxial relationship between the two structures.[35] Therefore, we now aim to further explore and resolve this issue by employing a nanofocused synchrotron X-ray beam on a cross-nucleated PB-1 sample.

5.2 Experimental

5.2.1 Sample preparation

A commercial isotactic polybutene-1, PB0110M, was employed in this work and its molecular characteristics were given in Table 3.1. The PB-1 pellets were first compressed into films with a thickness of about 0.30 mm in the melt state. Then, the thin film was heated to 180 °C in a Mettler hot-stage, kept at this temperature for 5 min to erase thermal history, and further cooled to 108 °C for isothermal crystallization for 4 h to obtain an hedrite of Form II.[35] The sample was then quickly quenched to room temperature causing the formation of numerous smaller crystals with low melting temperature. Finally, the sample was stored at room temperature for more than 1 month to completely transform the original Form II hedritic crystals into Form I. Before the synchrotron X-ray experiments, the sample was treated in a hot-stage: the small crystals of Form I were molten, keeping intact the large hedrite, and cross-nucleation was carried out at 90 °C. The final sample to be measured at the synchrotron consisted of Form II spherulites nucleated at the edges of the Form I hedrite. The choice of the two crystallization temperatures (108 °C for the substrate and 90 °C for the cross-nucleated morphology) ensured that the lamellar thickness of the resulting Form I is larger than that of the cross-nucleated Form II.

5.2.2 WAXD analysis

To access the local distributions of structural properties on the interface between the parent and daughter polymorphs, nanofocused synchrotron X-ray diffraction was employed (see section 3.2.2).

5.3 Results and discussions

5.3.1 Morphology after cross-nucleation

At first, the appearance of cross-nucleated spherulitic Form II (daughter polymorph) on the Form I hedritic substrate (parent polymorph) after isothermal crystallization at 90 °C is shown in Figure 5.1. The two polymorphs can be easily distinguished by optical microscopy due to their different morphologies. The square-shaped Form I crystal (hedrite) has a polygonal appearance, where the chain axis stands perpendicularly to the hedrite surface. During its crystallization in Form II, the *a/b* directions were found to be parallel to the edges of the hedrite.[42] Thus, the hedrite in Form I exhibited a single-crystal-like texture, where all the lamellar crystals are oriented uniformly in the same direction, however, without exhibiting a long-range order across the lamellar stacks as it was shown for the case of banded polymer spherulites for crystals, with high and low lattice symmetry, using X-ray nano-diffraction.[45, 46]

After the solid-state phase transition into the more stable Form I, the $(110)_I$ reflection shows a 12-fold symmetry indicating the coexistence and/or twinning of a hexagonal crystal lattice where the $(110)_I$ reflections are offset by ±15 and ±45° with respect to the normal of the hedrite growth face.[43]

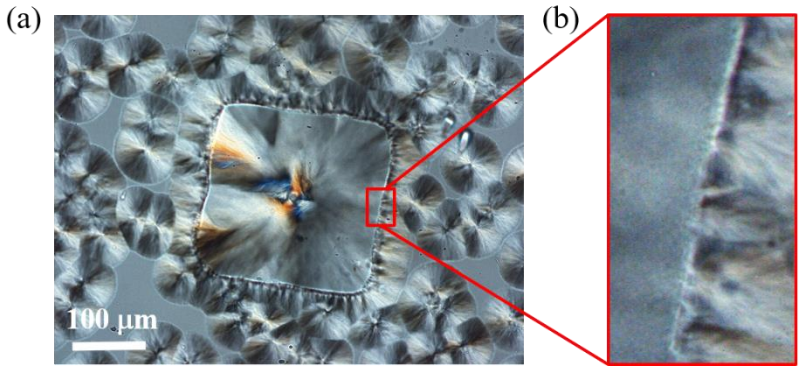

Figure 5.1 Optical micrograph (a) and a partially enlarged micrograph (b) of cross-nucleation of Form II on the Form I substrate at 90 °C.

At temperatures below 98 °C, PB-1 tends to crystallize into spherulites of Form II. The partial magnification of panel (a) of Figure 5.1 reveals that the origin of Form II nuclei around the parent polymorph occurs on the lateral surface of the Form I crystal. Form II further branches and grows until collision of adjacent crystals, eventually leading to a transcrystalline

layer near the interface, due to the relatively high number of nucleation sites.

After cross-nucleation was finished, the sample was probed by nanofocused X-ray WAXD. The two-dimensional (2D) diffraction pattern and the corresponding one-dimensional (1D) WAXD curve of the whole region of Figure 5.1b, obtained from the sum of each individual WAXD in the different spots, are reported in Figure 5.2. The purpose is structural identification and demonstrating the presence of the different polymorphs, as well as detecting possible overall orientation. The X-ray beam was incident perpendicularly to the sample's wide surface.

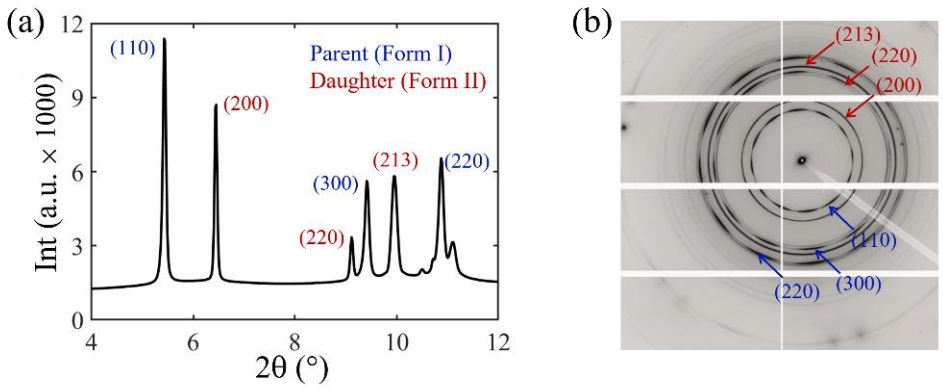

Figure 5.2 (a) One-dimensional (1D) WAXD curve and (b) corresponding two-dimensional (2D) diffraction pattern of the cross-nucleated PB-1 sample for the whole scanned area.

Taking into account the used wavelength, the distinct diffraction peaks observed at 2θ = 5.4, 9.4, and 10.9° correspond to the crystallographic planes of $(110)_I$, $(300)_I$, and $(220)_I$ of Form I, respectively. On the other hand, the diffraction signals of Form II characteristic $(200)_{II}$, $(220)_{II}$, and $(213)_{II}$ reflections are at 2θ = 6.5, 9.1, and 9.9°, respectively. From the diffraction peaks presented in Figure 5.2a, the crystals obtained through cross-nucleation can be identified as the Form II, due to the corresponding d-spacings identical to previous literature.[31, 32, 35] Moreover we could also neglect a meaningful extent of phase transition from Form II to Form I either during cross-nucleation or synchrotron measurement at room temperature. Besides being expected by the inherently slow transition kinetics, this is also deduced from the 2D WAXD pattern in Figure 5.2b. In fact, the azimuthal distributions of the diffraction intensity from the whole scanned area are almost isotropic for Form II, but they concentrated in relatively narrow arcs for Form I, indicating that Form II crystals are isotropically oriented on average, and the Form I substrate shows an anisotropic structure. The 2D patterns agree with the morphology observed by optical microscopy, in particular they confirm the single-crystal-like texture of the Form I hedrite and the spherulitic structure of Form II, with lamellar stacks

oriented in different directions. We address the two polymorphs as parent (Form I) and daughter (Form II) phases, respectively, to indicate the direction of cross-nucleation.

5.3.2 Space-resolved diffraction analysis

After having examined the overall WAXD of the selected area, thanks to the nanofocused WAXD scans, we can turn to the spatially resolved diffraction results. Figures 5.3a, b shows the optical micrograph and a map of the integrated intensity of the $(110)_I$ plane of Form I in the same area of the sample, respectively. Therewith, it is easy to judge the correspondence between the different morphology and the location of the two polymorphs. In fact, the intensity of Form I characteristic peaks displays a sudden drop at the interface with Form II spherulites, resulting in a clearly defined and relatively sharp boundary between the parent and daughter polymorphs. Hence, four locations across the interface are selected, as indicated by the black circles in panels a and b of Figure 5.3, for comparing the crystalline orientation of both polymorphs.

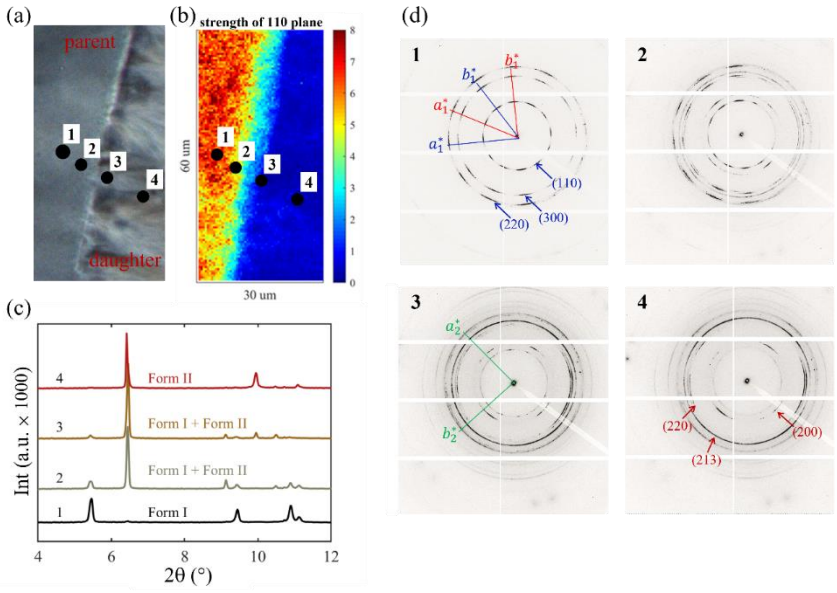

Figure 5.3 Cross-nucleated morphology between the parent and daughter phases showed in (a) the optical micrograph and (b) in the map of the diffraction intensity of the $(110)_I$ plane of Form I. A line scan across the interface of cross-nucleation is also shown. (c) WAXD curves of PB-1 obtained at the locations indicated in the line scan; (d) Corresponding two-dimensional (2D) diffraction patterns at the different positions.

For each indicated measurement position, the collected corresponding 1D and 2D WAXD

signals are presented in Figures 5.3c, d. The morphology at position 1 is exclusively composed of Form I (Figure 5.3c). This is in line with the expectation for cross-nucleation of PB-1 with the tetragonal modification nucleating on the surface of the pre-existing trigonal modification. At positions 2 and 3, both Form I and Form II shows distinct diffraction peaks, with Form I being the minority phase. This allows identifying a narrow region of the interface in which the two structures coexist, which possibly corresponds to the region where the nucleation event occurred. At position 4, well away from the interface, only Form II can be found.

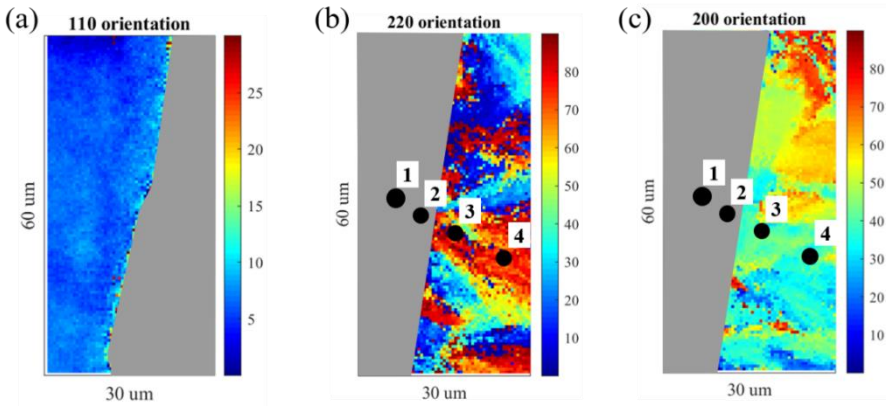

Figure 5.4 Map of the orientation in the analyzed area of the planes (a) $(110)_{I}$, (b) $(220)_{II}$, and (c) $(200)_{II}$, where various colors represent different orientation angles with respect to the horizontal direction in the detector plane. Gray areas indicate the absence of the diffraction from the specific plane, due to the polymorphic composition.

The lamellar orientation at different positions across the interface can be determined by the 2D patterns presented in Figure 5.4. It should be noted that the hedritic trigonal modification consists of flat-on lamellae with a single-crystal-like arrangement, as previously discussed in a similar microbeam diffraction study.[42] In Figures 5.2b and 5.3d, all the reflections belong to the *hk0* diffractions, corresponding to the [001]-zone X-ray diffraction pattern, which is typical for the Form I hedrite as the same diffraction pattern was obtained in Ref. [42]. The patterns exhibit a 12-fold symmetry. This is because the trigonal Form I was obtained by solid-state transformation of tetragonal Form II with a common diagonal (110) direction. Therefore, the 12 arcs pattern of the $(110)_{I}$ peak of Form I can be attributed to the twinned structure caused by the perpendicular deformation of Form II unit cells along the (110) or $(1\bar{1}0)$ planes during the phase transition. Based on the analysis of the Form I unit cell proposed by Tashiro et al., the a^* and b^* axes could be labeled as the $(110)_{I}$ reflection and they are separated by an angle of 60°, as shown by the red and blue lines in Figure 5.3d. Moreover, the $(110)_{I}$ planes of Form

I show an angle of ±15° with respect to the normal of the Form II hedrite growth face. Regarding the daughter Form II crystal, the b_2^* axis is perpendicular to the a_2^* axis as deduced by the position of the $(200)_{II}$ reflection (position 3 in Figure 5.3d) although it shows azimuthal broadening in the quadrant.[42]

Next, the orientations of Form I and Form II crystals were spatially resolved by considering the azimuthal distribution of the reflections. Figure 5.4 reports the azimuthal angles at which the first maximum in intensity is recorded for a specific plane, with 0° being the horizontal direction in the detector plane. In Figure 5.4a, the color of the area at different positions is very homogeneous, indicating that the orientation of Form I crystals within the hedrite exhibits an extremely narrow distribution with a FWHM of about 5°. On the other hand, the Form II crystals possess a spherulitic morphology, where the lamellar crystals grow along the radial direction synchronously with branching. The various orientations of $(220)_{II}$ and $(200)_{II}$ of Form II planes at different positions, as shown in Figures 5.4b, c, mean that by proceeding further away from the interface, the crystallites orient into various directions, which complies with the nature of spherulites. Checking carefully the map of $(200)_{II}$ and $(220)_{II}$ orientations, we notice that some parts near the nucleating interface show a similar orientation, with either the same or complementary azimuth according to the azimuthal symmetry of the particular diffraction peak. In order to look for a nucleation site, we combine the optical micrograph and the orientation map, and select positions 1-4 because they are located along the same radial direction of the Form II lamellae. Therefore, the part between positions 2 and 3 should be representative of one or few nucleation sites. Under this assumption, a possible epitaxial relationship between the two polymorphs can be then investigated, by considering the mutual orientations of the lattices in the area.

Figure 5.5a displays the 2D diffraction pattern of a small area of 0.5 × 4 μm^2 between positions 2 and 3. Compared to the diffraction of the $(110)_I$ plane at position 1 for Form I, the azimuthal distribution of the $(110)_I$ reflection at the interface is the same, meaning that the orientation of lamellae inside and at the interface of the Form I hedrite remains consistent. For Form II, the orientation has not changed largely, but the diffraction signal is enhanced due to the averaging of multiple patterns, at the expenses of a slight azimuthal broadening. The corresponding azimuthal intensity plots of $(110)_I$ and $(200)_{II}$ planes are shown in Figure 5.5b. The $(200)_{II}$ reflection displays 4 maxima spaced by 90°, with the first one located at a 45.7° angle. For Form I, the positions of the $(110)_I$ maxima correspond to 12 azimuthal angles, where the difference of the adjacent peaks is 30°. The first maximum is located at about 5°, while the

one nearest to the first peak of $(200)_{II}$ is found at ca. 35.7°.

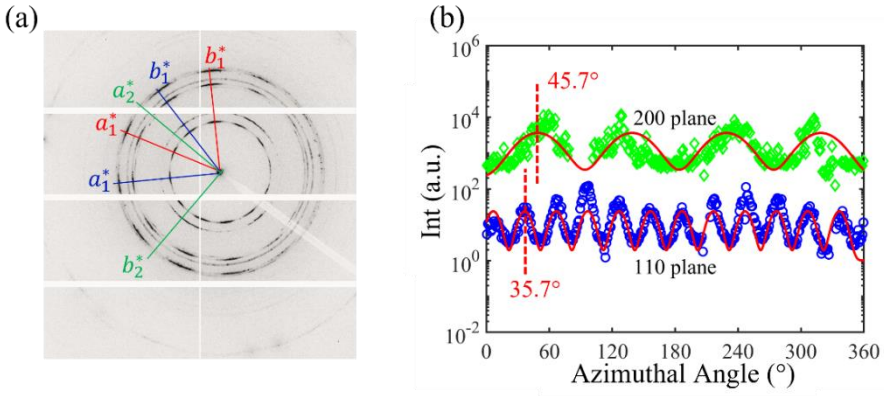

Figure 5.5 (a) Average two-dimensional diffraction pattern of the area (8 patterns, 0.5 × 4 μm^2) between positions 2 and 3. (b) Azimuthal intensity distribution of the characteristic diffractions of $(110)_I$ and $(200)_{II}$. The red lines represent a Gaussian fitting of the original data.

5.3.3 Proof of epitaxial relationship between the two polymorphs in PB-1

To show that the orientation of the planes of the parent Form I and daughter Form II crystals is a general observation, the orientation of the accumulated pattern, which corresponds to the sum of the patterns of the whole scanned area as shown in Figure 5.2b, was also analyzed. As shown in Appendix B1, the $(110)_I$ reflection of Form I shows a perfect 12-fold symmetry. Interestingly, the $(200)_{II}$ reflection of Form II exhibits a notable 4-fold symmetry (Appendix B2). The azimuthal of maxima (y) and sequence (x) of the peaks have the relationship (see Appendix B3 and B4):

$$y = 30 * x - 23.6 \qquad (110)_I$$

$$y = 90 * x - 45.1 \qquad (200)_{II}$$

The angle between the nearest maximum of $(200)_{II}$ and $(110)_I$ is ~8.5º. Considering the unit cell symmetry relationships, the angle between $(110)_{II}$ and $(200)_{II}$ of Form II is 45°. Therefore, it can be calculated that the $(110)_{II}$ plane of Form II has an average angle of ~6.5° with the $(110)_I$ plane of Form I, i.e., 45°-8.5°-30° (12-fold symmetry of Form I). In other words, the planes are practically parallel with each other. This indicates that the daughter Form II crystal exhibits a preferred orientation when nucleated at the Form I interface.

It is now interesting to discuss the potential epitaxial relationship between the two polymorphs. As stated above, during the Form II-to-I transformation, the (110) plane is in

common between the two structures. A schematic of the two structures and of the possible epitaxial arrangement is shown in Figure 5.6. The interchain distances within the (110) plane for the two polymorphs are almost identical: 10.1 Å for Form I and 10.5 Å for Form II. The mismatch is:

$$\frac{d_{\text{form II}} - d_{\text{form I}}}{d_{\text{form I}}} = \frac{10.5 - 10.1}{10.1} \times 100\% = 3.9\%$$

This value is well below the accepted mismatch criterium for epitaxial crystallization (15%). As a comparison, the mismatch in the a or b axis between Form I and Form II is larger than 15%.

$$\frac{a_{\text{form II}} - a_{\text{form I}}}{a_{\text{form I}}} = \frac{17.5 - 14.9}{14.9} \times 100\% = 17.4\%$$

Therefore, epitaxy is unlikely to occur along these directions.

After having considered the spacing matching perpendicular to the chain direction, we now turn the attention to the one along the chain axes. Both Form II and Form I possess helical chain conformations, 11/3 and 3/1, respectively. As such, the matching along the chain direction can be regarded as the fitting of two screws along the respective threads. The crest of the Form II screw should fit in the root of the Form I screw. Therefore, the dimension of interest is the distance between one helical turn, which can be calculated dividing the c-axis by the number of turns of the helix in the unit cell

$$\frac{c_{\text{Form II}}/3 - c_{\text{Form I}}/1}{c_{\text{Form I}}/1} = \frac{7.1 - 6.47}{6.47} \times 100\% = 9.7\%$$

In view of the above reasoning, it is highly probable that cross-nucleation of Form II on Form I occurs at the (110) contact planes.

The scheme of Figure 5.6 represents the epitaxial relationship at the molecular level, without taking into account the actual surface state, that is, roughness of Form I crystals, which might have been generated in the hedrite during Form II to Form I transformation. For the sake of simplicity, a reasonable assumption is that the surface can be considered molecularly flat, at least on the length scale of the nucleus size.

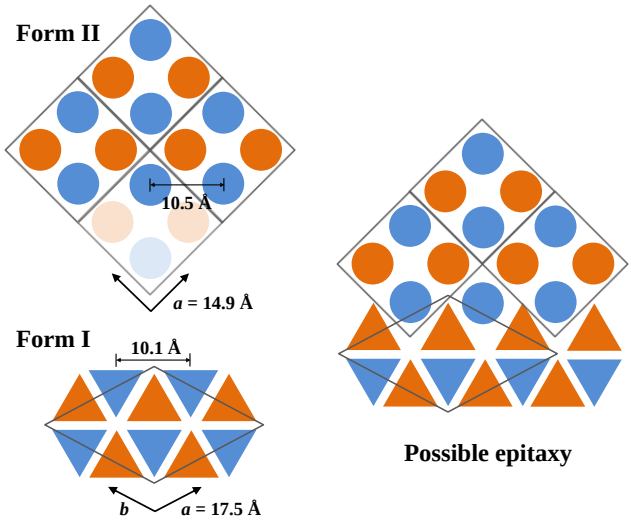

Figure 5.6 Schematic of the unit cells of Form II and Form I and the possible epitaxial relationship between them.

5.4 Conclusion

In summary, the cross-nucleation behavior of Form II on the surface of Form I in PB-1 has been studied by nanofocused synchrotron X-ray diffraction. A clearly defined boundary between the parent and daughter polymorphs and specific nucleation sites were found, through determining the content and orientation of both modifications with WAXD. The lattice orientation of the Form II lamellae formed on the interface is fixed, with their $(200)_{II}$ plane aligned ~8.5° apart from the $(110)_{I}$ plane of Form I. These results suggest that the two structures are in contact, in the cross-nucleation region, via their (110) planes, in which the mismatch of the interchain distances between the two modifications is about 4% only, and the one along the chain axes is less than 10%. Notably, this plane is the same as the $(110)_{I}$ plane generated during the solid-state Form II to Form I transition. The obtained results confirmed the capacity of PB-1 Form I hedrites to induce epitaxial crystallization of Form II.

References

[1] S. Zhang, Z. Wang, B. Guo, J. Xu, Secondary nucleation in polymer crystallization: A kinetic view, Polymer Crystallization 4(3) (2021) e10173.

[2] S. Agrawal, A. Paterson, Secondary nucleation: mechanisms and models, Chemical Engineering Communications 202(5) (2015) 698-706.

[3] X. Sun, S. Yan, Polymer Morphology: Principles, Characterization, and Processing, John

Wiley & Sons 2016.

[4] H. Li, S. Yan, Surface-induced polymer crystallization and the resultant structures and morphologies, Macromolecules 44(3) (2011) 417-428.

[5] X. Liu, Heterogeneous nucleation or homogeneous nucleation?, The Journal of Chemical Physics 112(22) (2000) 9949-9955.

[6] R.P. Sear, Heterogeneous and homogeneous nucleation compared: Rapid nucleation on microscopic impurities, The Journal of Physical Chemistry B 110(10) (2006) 4985-4989.

[7] H. Duran, M. Steinhart, H.J.r. Butt, G. Floudas, From heterogeneous to homogeneous nucleation of isotactic poly (propylene) confined to nanoporous alumina, Nano Letters 11(4) (2011) 1671-1675.

[8] E.H. Lee, S.X. Boerrigter, S.R. Byrn, Epitaxy of a structurally related compound on the (100) faces of flufenamic acid form I and III single crystals, Crystal growth & design 10(2) (2010) 518-527.

[9] I. Bonev, On the terminology of the phenomena of mutual crystal orientation, Acta Crystallographica Section A: Crystal Physics, Diffraction, Theoretical and General Crystallography 28(6) (1972) 508-512.

[10] S. Kopp, J. Wittmann, B. Lotz, Epitaxial crystallization and crystalline polymorphism of poly (1-butene): form I, Polymer 35(5) (1994) 916-924.

[11] S. Kopp, J. Wittmann, B. Lotz, Epitaxial crystallization and crystalline polymorphism of poly (1-butene): forms III and II, Polymer 35(5) (1994) 908-915.

[12] Y. Li, Z. Guo, M. Xue, S. Yan, Epitaxial recrystallization of iPBu in form II on an oriented iPS film initially induced by oriented form I iPBu, Macromolecules 52(11) (2019) 4232-4239.

[13] C. Tu, S. Jiang, H. Li, S. Yan, Origin of epitaxial cold crystallization of poly (L-lactic acid) on highly oriented polyethylene substrate, Macromolecules 46(13) (2013) 5215-5222.

[14] P. Krogstrup, N. Ziino, W. Chang, S. Albrecht, M. Madsen, E. Johnson, J. Nygård, C.M. Marcus, T. Jespersen, Epitaxy of semiconductor–superconductor nanowires, Nature materials 14(4) (2015) 400-406.

[15] U.W. Pohl, Epitaxy of semiconductors, Springer 2020.

[16] H. Zhou, S. Jiang, S. Yan, Epitaxial crystallization of poly (3-hexylthiophene) on a highly oriented polyethylene thin film from solution, The Journal of Physical Chemistry B 115(46) (2011) 13449-13454.

[17] Z. Guo, R. Xin, J. Hu, Y. Li, X. Sun, S. Yan, Direct high-temperature form I crystallization of isotactic poly (1-butene) assisted by oriented isotactic polypropylene, Macromolecules 52(24) (2019) 9657-9664.

[18] L. Li, J. Hu, Y. Li, Q. Huang, X. Sun, S. Yan, Evidence for the soft and hard epitaxies of poly (L-lactic acid) on an oriented polyethylene substrate and their dependence on the crystallization temperature, Macromolecules 53(5) (2020) 1745-1751.

[19] J. Petermann, Y. Xu, J. Loos, D. Yang, Epitaxial crystallization of syndiotactic polypropylene on uniaxially oriented polyethylene, Polymer 33(5) (1992) 1096-1098.

[20] D. Fenwick, P. Smith, J. Wittmann, Epitaxial and graphoepitaxial growth of materials on highly orientated PTFE substrates, Journal of materials science 31(1) (1996) 128-131.

[21] B. Lotz, J. Wittmann, Structural relationships in blends of isotactic polypropylene and polymers with aliphatic sequences, Journal of Polymer Science Part B: Polymer Physics 24(7) (1986) 1559-1575.

[22] T. Takahashi, F. Teraoka, I. Tsujmoto, Epitaxial crystallization of crystalline polymers on the surface of drawn polytetrafluoroethylene, Journal of Macromolecular Science, Part B: Physics 12(3) (1976) 303-315.

[23] S. Kopp, J. Wittmann, B. Lotz, Epitaxy and Crystal Polymorphism of Isotactic Polybutene-1, Crystallization of Polymers, Springer1993, pp. 625-629.

[24] S.J. Bonafede, M.D. Ward, Selective nucleation and growth of an organic polymorph by ledge-directed epitaxy on a molecular crystal substrate, Journal of the American Chemical Society 117(30) (1995) 7853-7861.

[25] S. Chen, H. Xi, L. Yu, Cross-nucleation between ROY polymorphs, Journal of the American Chemical Society 127(49) (2005) 17439-17444.

[26] S. Boerrigter, C. Van Den Hoogenhof, H. Meekes, P. Bennema, E. Vlieg, P. Van Hoof, In situ observation of epitaxial polymorphic nucleation of the model steroid methyl analogue 17 norethindrone, The Journal of Physical Chemistry B 106(18) (2002) 4725-4731.

[27] C. Stoica, P. Tinnemans, H. Meekes, E. Vlieg, P. Van Hoof, F. Kaspersen, Epitaxial 2D nucleation of metastable polymorphs: A 2D version of Ostwald's rule of stages, Crystal growth & design 5(3) (2005) 975-981.

[28] J. Tao, K.J. Jones, L. Yu, Cross-nucleation between D-mannitol polymorphs in seeded crystallization, Crystal growth & design 7(12) (2007) 2410-2414.

[29] Y. Park, S.X. Boerrigter, J. Yeon, S.H. Lee, S.K. Kang, E.H. Lee, New metastable packing polymorph of donepezil grown on stable polymorph substrates, Crystal growth & design 16(5) (2016) 2552-2560.

[30] S. Looijmans, A. Menyhard, G.W. Peters, G.C. Alfonso, D. Cavallo, Anomalous temperature dependence of isotactic polypropylene α-on-β cross-nucleation kinetics, Crystal growth & design 17(9) (2017) 4936-4943.

[31] D. Cavallo, L. Gardella, G. Portale, A.J. Müller, G.C. Alfonso, On cross-and self-nucleation in seeded crystallization of isotactic poly (1-butene), Polymer 54(17) (2013) 4637-4644.

[32] D. Cavallo, L. Gardella, G. Portale, A.J. Müller, G.C. Alfonso, Kinetics of cross-nucleation in isotactic poly (1-butene), Macromolecules 47(2) (2014) 870-873.

[33] D. Cavallo, F. Galli, L. Yu, G.C. Alfonso, Cross-Nucleation between Concomitantly Crystallizing α-and γ-Phases in Polypivalolactone: Secondary Nucleation of One Polymorph on Another, Crystal growth & design 17(5) (2017) 2639-2645.

[34] C. Fraschini, L. Jiménez, B. Kalala, R.E. Prud'homme, Polymorphism and cross-nucleation in poly (1, 3-dioxolan), Polymer 53(1) (2012) 188-195.

[35] W. Wang, B. Wang, E. Carmeli, Z. Wang, Z. Ma, D. Cavallo, Cross-nucleation of polybutene-1 Form II on Form I seeds with different morphology, Polymer Crystallization 3(2) (2020) e210104.

[36] Y. Nozue, S. Seno, T. Nagamatsu, S. Hosoda, Y. Shinohara, Y. Amemiya, E. Berda, G. Rojas, K. Wagener, Cross nucleation in polyethylene with precisely spaced ethyl branches, ACS Macro Letters 1(6) (2012) 772-775.

[37] B. Lotz, Molecular aspects of structure and morphology of isotactic polypropylene, Journal of Macromolecular Science, Part B: Physics 41(4-6) (2002) 685-709.

[38] J. Wang, Z. Ren, X. Sun, H. Li, S. Yan, The βα growth transition of isotactic polypropylene during stepwise crystallization at elevated temperature, Colloid and Polymer Science 293(10) (2015) 2823-2830.

[39] W. Wang, C. Shao, L. Zheng, B. Wang, L. Pan, G. Ma, Y. Li, Y. Wang, C. Liu, Z. Ma, Stretching-induced phase transition of the butene-1/ethylene random copolymer: Orientation and kinetics, Journal of Polymer Science Part B: Polymer Physics 57(2) (2019) 116-126.

[40] R. Xin, J. Zhang, X. Sun, H. Li, Z. Ren, S. Yan, Polymorphic behavior and phase transition of poly (1-butene) and its copolymers, Polymers 10(5) (2018) 556.

[41] G. Natta, P. Pino, P. Corradini, F. Danusso, E. Mantica, G. Mazzanti, G. Moraglio, Crystalline high polymers of α-olefins, Journal of the American Chemical Society 77(6) (1955) 1708-1710.

[42] K. Tashiro, H. Yamamoto, K. Funaki, J. Hu, Synchrotron microbeam X-ray scattering study of the crystallite orientation in the spherulites of isotactic poly (butene-1) crystallized isothermally at different temperatures, Polymer Journal 51(2) (2019) 143-153.

[43] K. Tashiro, J. Hu, H. Wang, M. Hanesaka, A. Saiani, Refinement of the crystal structures of forms I and II of isotactic polybutene-1 and a proposal of phase transition mechanism

between them, Macromolecules 49(4) (2016) 1392-1404.

[44] J. Hu, K. Tashiro, Relation between higher-order structure and crystalline phase transition of oriented isotactic polybutene-1 investigated by temperature-dependent time-resolved simultaneous WAXD/SAXS measurements, Polymer 90 (2016) 165-177.

[45] M. Rosenthal, G. Bar, M. Burghammer, D.A. Ivanov, On the nature of chirality imparted to achiral polymers by the crystallization process, Angewandte Chemie 123(38) (2011) 9043-9047.

[46] M. Rosenthal, G. Portale, M. Burghammer, G. Bar, E.T. Samulski, D.A. Ivanov, Exploring the origin of crystalline lamella twist in semi-rigid chain polymers: The model of Keith and Padden revisited, Macromolecules 45(18) (2012) 7454-7460.

Chapter 6. Nucleation of polybutene-1 on the surface of different fibers

6.1 Introduction

Polymer/fiber composites have attracted much attention in the past few decades, as a way to improve mechanical properties of plastic materials for specific applications. These composites have been extensively used in a wide range of fields, from packaging to aerospace applications.[1-8] The performance improvements of polymer/fiber composites are attributed actually to excellent properties of the used fiber but depend strongly on the interfacial interaction between the rigid fiber and the soft matrix. Fiber-induced interfacial crystallization is recognized as a promising method to improve polymer/fiber interfacial interactions.[6, 9, 10] It effectively accelerates the nucleation kinetics of the matrix by providing more nucleation sites. A special heterogeneous nucleation morphology, termed transcrystalline layer (TCL), is produced as a result of the most important kind of interfacial interactions and has been widely reported and under focus recently.[3, 10-18] The formation of TCL is associated with an extremely high nucleating ability of the fibers, causing the crystals to grow perpendicular to the fiber axis. Many factors, such as surface chemistry[19-23] and roughness of the fiber,[3, 14, 16, 24-27] molecular weight, chain conformation and functional groups of the polymer matrix,[28-38] are believed to affect surface-induced nucleation in composites. The dominant factor is still debated.

Fiber-induced nucleation has been studied in detail in many works.[11-15, 18, 19, 25, 39-49] Among them, isotactic polypropylene (iPP) has been most frequently chosen, as a representative research system, due to its diversified structures and relatively low nucleation density. For example, Wang et al.[39] utilized in situ polarized optical microscopy (POM) and atomic force microscopy (AFM) to study the fiber-induced crystallization of iPP monoclinic crystals on the fibers of poly(butylene terephthalate) (PBT), poly(ethylene terephthalate) (PET) and poly(trimethylene terephthalate) (PTT). It was found that nucleating ability of three fibers toward iPP followed the order PBT > PET ≈ PTT, which is attributed to the possession of a large length of the ac-plane crystal surface for PBT, that is convenient for epitaxial crystallization. Moreover, they also focused on the study of nucleation ability of other fibers, such as carbon, Kevlar, and poly(*p*-phenylene benzobisoxazole) fiber. It is interesting to find that the maximum temperature for TCL formation is associated with the interfacial free energy

difference ($\Delta\sigma$), which determines the free energy barrier for nucleation.[11-15, 18] On the other hand, poly(l-lactide) (PLLA)/fiber composites have also been the subject of nucleation studies. Wen et al.[40] studied the crystallization phenomenon of SC (stereocomplex) and PLLA fibers toward a PLLA matrix. They found that the nucleating ability of the TCL layer along the PLLA fiber was much larger than that along the SC ones. Wang et al.[25] also paid attention to the nucleation ability of PLLA on various fibers, including poly(ethylene terephthalate), carbon, Kevlar, glass, hemp, linen, and cellulose. It was found that $\Delta\sigma$ decreased with an increase of surface roughness for most fibers, although SC and carbon fibers displayed relevant deviations, which means that other factors may also influence the surface-induced nucleation process of fibers, such as fiber/matrix chemical interactions.

Despite the wealth of information in fiber-induced nucleation literature, the explored systems are still rather limited, and information on other different polymers could help in drawing general conclusions. Among the diverse polyolefin materials, polybutene-1 appears to be a useful system for studying the nucleation process induced by fibers. First, PB-1 as a conventional plastic has extensive applications in high pressure tanks, pumps, and hot-water pipes. Thus, the study of the fiber-reinforced composites based on this material is of great importance. Second, the nucleation and crystal growth are comparatively slow in the bulk, at relatively high temperatures, which makes it possible to achieve real-time measurements. Finally, PB-1 is a polymorphic polymer, which has diversified crystalline modifications, forms I/I', II, and III.[50, 51] In practice, Forms I and II are the most processing-relevant modifications. Form II can be generated directly from regular melt crystallization as it is kinetically favored.[52-55] Form I is the most stable modification from a thermodynamic point of view, which is generally transformed from Form II through quiescent aging at room temperature.[56-65] Therefore, it arouses our interest to design a fibrous Form I substrate with a higher melting temperature, to tailor the crystallization and morphology of Form II for high-performance all-PB-1 composites. Meanwhile, other fibers are also included in the study.

6.2 Experimental

6.2.1 PLOM analysis

The PB-1 homopolymer used in this chapter was kindly provided by Lyondell-Basell Industries, with trade name PB0300M. The details of this polymer are listed in Table 3.1. PB-1 films were prepared through manual compression molding between glass slides, above the equilibrium melting temperature (e.g., 180 °C) and the average thickness was about 50-70 μm.

The fibers used in the present work were kindly provided by various research institutions and companies. For instance, the PLLA, SC (stereocomplex) and PB-1 Form I fibers were supplied by the Institute of Chemistry of the Chinese Academy of Science in Beijing and have been used in previous studies.[25, 45] And some commercial fibers (i.e., carbon, glass and PP fibers) were kindly provided by Borealis and used as received.

For the in-situ PLOM characterization during isothermal crystallization, the employed technique was described in section 3.2.1. The temperature protocol adopted for sample preparation and crystallization experiments is schematized in Figure 6.1, and mainly consisted of the following steps. Step a: one piece of a PB-1 film was heated from room temperature to 180 °C (T_m). Step b: held at T_m for 5 min to erase the thermal history. Step c: cooled at 20 °C/min down to the selected temperature (T_i =150 °C). A single fiber was introduced manually into the film and the single-fiber polymer composite was covered with a microscope cover glass.[25, 66] In the case of the PB-1 Form I fiber, a lower T_i of 130 °C was necessarily used, due to the lower melting point. Step d: induced stress was relaxed at T_i for t_i = 30 min. Step e: cooled at 20 °C/min down to the selected isothermal crystallization temperature T_c. Step f: isothermal crystallization was performed at T_c for t_c (subjected to the actual experimental time) and PLOM data acquisition was performed with a collection time of 5 s for each profile.

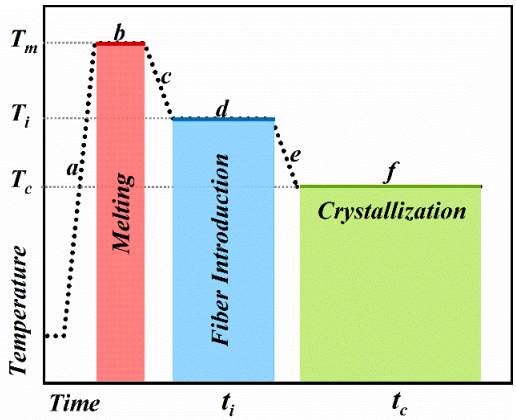

Figure 6.1 Schematic diagram of the applied thermal history.

6.2.2 AFM analysis

The quantitative analysis of investigated fibers' topography via AFM was performed on the surface of different fibers as described in section 3.2.3.

6.3 Results and discussions

6.3.1 Morphologies induced by the different fibers

Figure 6.2 shows four typical examples of the time-resolved polarized optical microscopy images obtained during isothermal crystallization of PB-1 Form II onto different fibers. The selection of isothermal crystallization temperatures between 91 and 101 °C follows from the fact that such temperatures are low enough to ensure fast isothermal crystallization but high enough to prevent the occurrence of non-isothermal crystallization during cooling. It should be noted that the exact polymorph formed on the surface of fibers can be easily identified by a melting experiment with optical microscopy (see Appendix C1), where the crystal completely disappears within melting range of Form II (about 105-120 °C).

In Figure 6.2b, a clear sporadic nucleation process with crystallization time, an indication of a very low density of nucleation sites, is observed for carbon fiber. The typical hybrid shish–calabash structure can be observed in PB-1/carbon composite, in which carbon fiber serves as shish and Form II spherulites serves as calabash.[30, 31, 67, 68] On the contrary, the PB-1 Form I fiber shows the peculiar transcrystalline layer morphology due to a very high density of nucleation sites and the absence of lateral separation between the individual growing spherulites.[69-73] This transcrystalline morphology has been highlighted also for iPP fiber/PP matrix homo-composites and scanning electron microscopy observations revealed that it is composed of mostly edge-on α-phase lamellae with their growth direction perpendicular to the fiber axis.[66] An analogous morphology is expected for this all-PB-1 composite. Obviously, the PP and glass fibers display intermediate nucleation density between that of carbon and Form I fibers. A similar nucleation process is also observed for the other two fibers shown in Appendix C2.

It is apparent that the nucleating ability of glass, carbon, PP, PLLA and SC fibers is exceedingly low with respect to Form I fiber. The low nucleation density enables us to observe readily the morphology of the crystallites and count directly the amount of spherulites (nuclei), to calculate precisely the nucleation rate. More interestingly, the morphology for Form II crystallization on the glass, PP, PLLA and SC fibers cannot be easily defined as HSC or TCL. This is because the density of active nuclei on these fibers' surface is not so low that each nucleus will grow in a radial pattern, neither so high that nuclei can grow just along the direction perpendicular to the fiber, and thus violates the rule of TCL. On the other hand, the HSC structure is described as few nuclei developing into large separated spherulites at the

interface of polymer/filler composites without hindrance.[9, 30] For these four fibers in this chapter, we can find collision and impingement between these deformed spherulites. Therefore, the morphology should be defined as an intermediate state of HSC and TCL. However, for the sake of convenience, we can refer to this morphology as HSC in the following section.

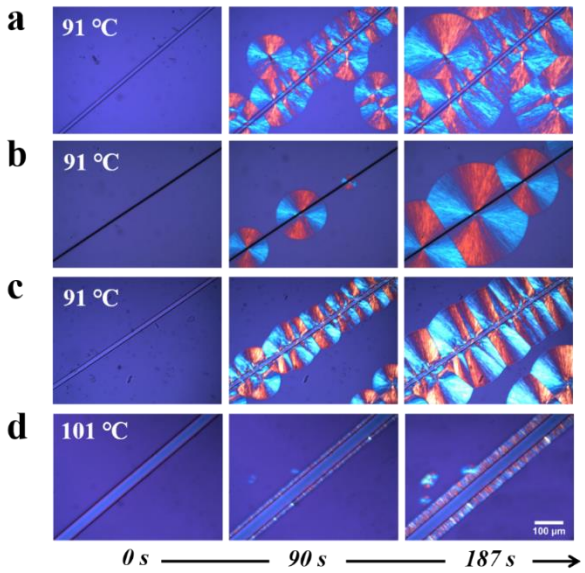

Figure 6.2 Polarized optical micrographs of PB-1 matrix crystallized on the surface of (a) glass, (b) carbon, (c) PP and (d) PB-1 Form I fibers during isothermal crystallization at selected T_c values.

Figure 6.3 shows the difference of PB-1 Form II crystallization at different crystallization temperatures, which can be deduced by comparing the morphology developed on the fiber surface after a given holding time at different undercoolings. First, it is easy to find that the number of crystallized spherulites on the fiber surface at the same time decreased with increasing crystallization temperature, even if the temperature difference is just 1 °C in Figures 6.3a and b (more data are displayed in Appendix C3). While the sporadic nucleation process on glass and carbon fibers is beneficial for morphological observation and counting the number of nuclei, for the Form I fiber it is hard to observe the change of number of nuclei by the naked eye, due to the TCL structure (Figure 6.3c). This is a consequence of the high nucleation density and lack of lateral separation between the individual growing spherulites on the fiber surface, causing the crystals to grow crowded together. It is observed that Form II always nucleates on the surface of the Form I fiber with a transcrystalline morphology, even near the Form II melting temperature (melting peak range of 105-120 °C). This observation is different from the

previous work of surface-induced nucleation of SC fiber toward PLLA.[25] For instance, when the crystallization temperature of PLLA is increased by 5 °C from 142.5 to 147.5 °C, a morphological change from TCL to sporadic spherulites is observed. Moreover, the crystalline morphology of PB-1 matrix on the surface of the other fibers is always HSC, even though the temperature varied by 4 °C, as shown in Figures 6.3a,b and Appendix C3. The particular morphological changes of PB-1 Form II crystallized on different fibers will be discussed in detail below.

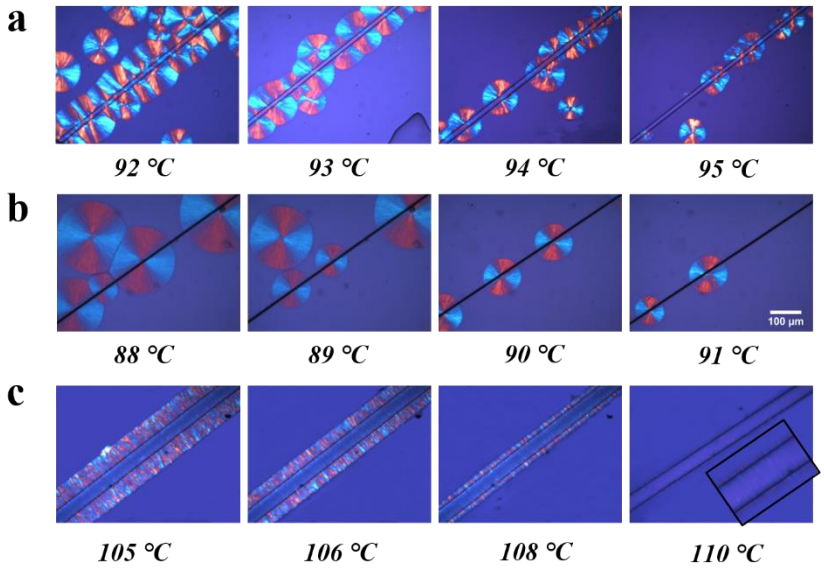

Figure 6.3 Morphological changes of PB-1 matrix crystallized on the surface of (a) glass and (b) carbon fibers for 90 s and of (c) Form I fiber for 920 s at selected T_c values. The inset of (c) is a close-up showing a very thin TCL.

Despite the above results, the difference in nucleation ability of various fibers is still far from being understood, because both fiber diameter and the elapsed time for the surface-induced nucleation are different. In the following sections, we will compare quantitatively the nucleation kinetics and focus on which major factor is controlling fiber-induced nucleation.

6.3.2 Nucleation kinetics of PB-1 on different fibers

To quantitatively evaluate the nucleation capacity of various fibers toward PB-1, a direct counting method was employed to obtain the amount of nuclei at various undercoolings. It is reasonable to derive the nucleation density (i.e., number of nuclei per unit area) using the total number of nuclei counted from the whole micrograph divided by the overall lateral surface of

the fiber. Unfortunately, this method is applicable only for relatively low nucleation density of the matrix on the surface of the fiber: the greater the nucleation density, the more difficult the counting of the number of nuclei. In particular it cannot be adopted for the TCL structure.

Figure 6.4 summarizes the evolution of the nucleation density of PB-1 on PP and PLLA fibers as a function of time at different undercoolings. The displayed fibers are selected as representative examples of the nucleation experiments, while all of the results for the other fibers are shown in Appendix C4. In Figure 6.4a,b, a linear increase of nucleation density is observed with time, and the different nucleation rates can be derived by the slope of the fitting lines at various T_c values. Moreover, with the increase of T_c values, the nucleation rate significantly decreased no matter which fiber was employed (see Appendix C4). This is in line with the nucleation process occurring in iPP/fiber and PLLA/fiber composites,[11, 12, 18, 25] as expected from the classical nucleation theory.

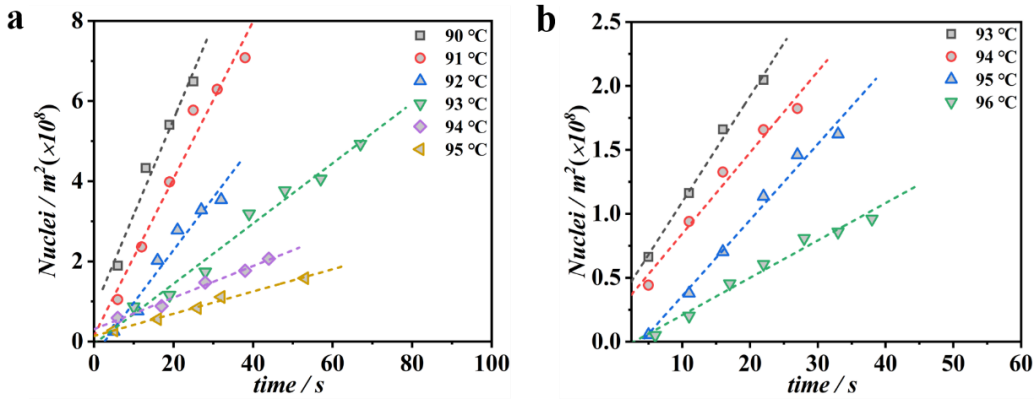

Figure 6.4 Nucleation density of PB-1 Form II on the surface of (a) PP and (b) PLLA fibers as a function of time for specimens crystallized at selected T_c values.

It should be noted that the Form I fiber always induces the formation of the Form II TCL structure in the investigated temperature range, as shown in Figure 6.3c; therefore, the direct counting of the number of nuclei is obviously not possible. As such, a different method is employed to quantitatively determine the nucleation kinetics on such fibers. Figure 6.5a shows the evolution of the light intensity of the Form I fiber-induced PB-1 Form II nucleation process as a function of time during crystallization at different temperatures. A rectangular region including the TCL area is selected, as shown in Appendix C5. The mean light intensity is calculated for the same selected area in each acquired frame with the use of ImageJ software. It is possible to easily derive the induction time, which is defined as the point of increase of the luminous flux from the initial plateau to a fast growth stage. The exact value of the induction

time is indicated by the corresponding colored arrows for the various T_c values in Figure 6.5a.

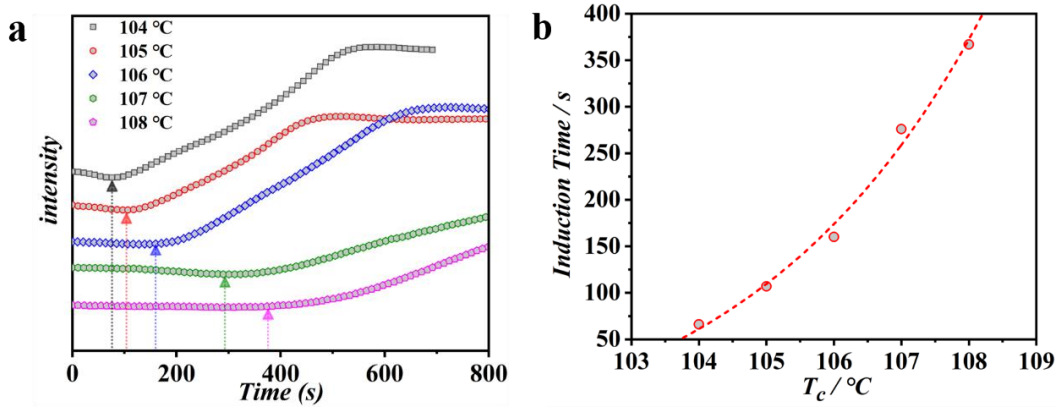

Figure 6.5 (a) Evolution of light intensity as a function of crystallization time during isothermal crystallization for Form II nucleation on the surface of Form I fiber at selected T_c values. The induction times are indicated by the corresponding colored arrows at various T_c. (b) Induction time for Form I fiber induced nucleation toward PB-1 matrix as a function of T_c.

To clearly compare the effect of T_c on the nucleation of Form II on the Form I fiber, the evolution of induction time as a function of Tc is reported in Figure 6.5b. As expected, strong dependence of nucleation kinetics (induction time) on crystallization temperature is observed, with an exponential relationship. This is consistent with the result of our work,[45] noting that the nucleation rate of Form II of the high-molecular-weight matrix (PB0110, used in Chapter 4) is slightly faster than that of the low-molecular-weight matrix (PB0300) on the same surface of the Form I fiber.

In terms of the nucleation kinetics of Form II on different fibers, it is essential to introduce a quantitative parameter $\Delta\sigma$, which represents the nucleating ability of the surface toward the polymer matrix.[74-76] Being directly proportional to the nucleation free-energy barrier, the lower the $\Delta\sigma$, the faster the nucleation. Some studies have proved the effectiveness of this parameter for characterizing the nucleation activity of fibers, such as in PE, PP, PCL, and PLLA composites.[11-15, 18, 25, 39, 41, 42]Accordingly, all nucleation density data could be analyzed based on the theory of heterogeneous nucleation, which expresses the nucleation rate I as [76]

$$I = I_0 \exp\left(-\frac{U^*}{R(T-T_\infty)}\right) \exp\left(-\frac{16\sigma\sigma_e\Delta\sigma T_m^{0^2}}{kTf^2\Delta T^2\Delta h_0^2}\right) \quad (6.1)$$

where I_0 is a constant independent of temperature, U^* is the activation energy related to the

transport of chain segments across the phase boundary, R is the gas constant, T_∞ is the temperature below which all motions associated with viscous flow cease (= $T_g - 30$), Δh_0 is the enthalpy of fusion per unit volume of bulk crystal at T_m^0, f is a correction factor (= $2T_c / (T_c + T_m^0)$) that describes the temperature dependence of the fusion enthalpy and k is the boltzmann constant. σ and σ_e are the free energies of the lateral and fold surfaces in contact with the supercooled melt.[45, 77] However, induction time data of Form II nucleation on the surface of Form I fiber are not suitable for equation (6.1). Based on the assumption that the product between I and t_i at a given temperature is constant,[42] induction time data can be analyzed using the following equation.

$$\frac{1}{t_i} = I_0 \exp\left(-\frac{U^*}{R(T - T_\infty)}\right) \exp\left(-\frac{16\sigma\sigma_e \Delta\sigma T_m^{0^2}}{kTf^2\Delta T^2 \Delta h_0^2}\right) \tag{6.2}$$

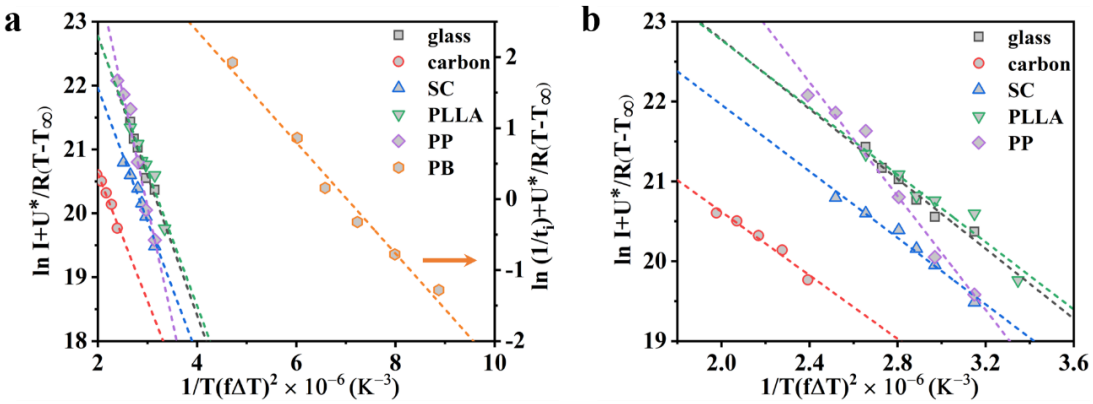

Figure 6.6 (a) Variation of nucleation rate with degree of undercooling according to equations (6.1) and (6.2) (for Form I fiber). (b) Magnification of the low crystallization temperature region.

Figure 6.6 shows the evolution of nucleation kinetics as a function of crystallization temperature for the Form I fiber according to equation (6.2) and for the other fibers according to equation (6.1). The linear fit of the nucleation rate data in the studied supercooling range clearly shows that the nucleation rate of PP and Form I fibers are considerably different from those of other fibers. More specifically, the energy barrier for the nucleation of Form II is the lowest on Form I fiber and is the highest on the PP fiber among all the fibers, just judging from the slope which is proportional to $\Delta\sigma$. On the other hand, it is apparent that the rest of the fibers presented similar $\Delta\sigma$ due to nearly parallel linear fit, although slight differences can be appreciated in Figure 6.6b. A value U^* = 6280 J/mol for the transport of chain segments to the

crystal growth front has been suggested. Bulk enthalpy of fusion Δh_0 of the Form II mesophase of 56 J/cm^3 can also be obtained from previous work.[77] From Appendix C6a, we know the equilibrium melting temperature (T_m^0 = 398.74 K) of the used PB-1 grade determined using the Hoffman–Weeks method. The glass transition temperature (T_g) for the calculation of T_∞ is 246.29 K, as measured via differential scanning calorimetry (DSC) (Appendix C6b). The value of the term $\sigma\sigma_e$ of 41.75 erg^2/cm^4 was calculated using the L-H growth model, that is, a plot of $lnG+U^*/R(T-T_\infty)$ versus $1/T\Delta Tf$ yields a straight line with a slope proportional to $\sigma\sigma_e$.[15, 78]

Table 6.1 Fiber features and measured PB-1 Form II crystal nucleation parameters [a]

Type of fiber	Diameters (μm)	Roughness, R_q (nm)	$\Delta\sigma$ (mJ/m^2)	$Ln(I_0)$ (nuclei/m^2 s)
PB Form I	47.1 ± 1.1	37.1	0.31 ± 0.02	
PP	16.8 ± 0.4	20.6	1.42 ± 0.08	30.8 ± 0.9
PLLA	68.9 ± 8.2	23.4	0.84 ± 0.08	27.0 ± 0.9
SC	62.3 ± 5.5	27.6	0.80 ± 0.06	26.3 ± 0.5
Carbon	7.2 ± 0.3	54.1	0.76 ± 0.05	24.6 ± 0.4
Glass	16.2 ± 1.0	25.0	0.85 ± 0.08	27.2 ± 0.7

[a] $\Delta\sigma$ and I_0 from equation (6.1) calculation.

In Table 6.1, all the parameters of fiber features and the surface-induced nucleation process have been summarized. Similar values of $\Delta\sigma$ ranging from about 0.76 to 0.85 mJ/m^2 were observed for most of the investigated fibers. Corresponding to minimum and maximum absolute values of the slopes of Form I and PP fiber within the nucleation rate plot in Figure 6.6, $\Delta\sigma$ values of 0.31 and 1.42 mJ/m^2 are obtained at both extremes.

6.3.3 Different factors affecting fiber-induced nucleation

The nucleating ability of various fibers toward a polymer matrix has been a subject that deserved some discussion in the past few decades. The topography of the fiber surface is widely used to account for this phenomenon.[3, 14, 15, 25, 79, 80] This is because an alternating groove and ridge morphology always exists at the fiber surface due to processing defects. Such a surface topography plays a significant role in improving the nucleation of the matrix induced by fillers in two aspects. First, an expanded lateral area may result in more efficient sites for nucleation.[15] Second, the thermal stress developed at the fiber surface might induce local

orientation of matrix chain segments, causing a lower $\Delta\sigma$.[14, 18] The roughness of the fiber surface is typically defined using the value of root-mean-square roughness (R_q), which is expected to quantify this topography.

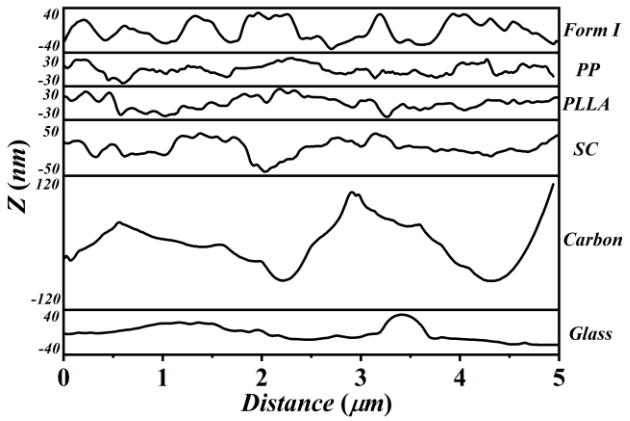

Figure 6.7 Examples of surface height profiles of all of the fibers derived from the analysis of AFM images.

Guided by the above-mentioned work, to figure out the effect of fiber surface topography on Form II nucleation in PB-1/fiber composites, AFM measurements were performed. Appendix C7 shows the three-dimensional (3D) AFM surface topography images of all the fibers, and Figure 6.7 shows the corresponding one-dimensional (1D) characteristic height profiles obtained by processing the 3D images. Groove and valley morphologies with a typical length scale of a few tens of nanometers are present at the surface of all the fibers. Therefore, the roughness (R_q) of the fiber surface, generally available by quantitative measurements of the groove height and average calculation in the AFM software, is considered to account for the surface structure and compare the differences of various fibers at the nanometer scale. From Figure 6.7, one can readily observe the difference between the fibers' roughness, by looking at the adopted height scale. For example, the roughness of the carbon fiber is expected to be the largest, while that of PP and PLLA should be the smallest, as judged from the y-axis scale. The exact values of the root-mean-square roughness parameter for all the fibers have been calculated and are summarized in Table 6.1.

The evolution of interfacial free-energy difference ($\Delta\sigma$) as a function of roughness (R_q) for the fibers is presented in Figure 6.8. Although a general trend cannot be recognized, the value of $\Delta\sigma$ decreases in an exponential manner with the increase of the roughness (see the dashed line), when the PB-1 Form I fiber is excluded. On the other hand, an almost linear decrease of the interfacial free-energy difference with roughness is found, if the data of the

carbon fiber are neglected (oval area). This means that, in general terms, the nucleation process is favored by the rough surface of fibers in the polymer/fiber composites. This finding is in agreement with various systems.[15, 25, 81] For example, Lin et al. found that rougher copper substrates led to smaller values of the interfacial free-energy difference for iPP nucleation. Wang et al. also reported a similar trend of $\Delta\sigma$ as the roughness of the fibers increases in the PLLA/fiber composites. Despite this rather general conclusion, the fact that the entire data set cannot be described by a single relationship indicates that roughness is not the sole parameter that characterizes the nucleation free-energy barrier.

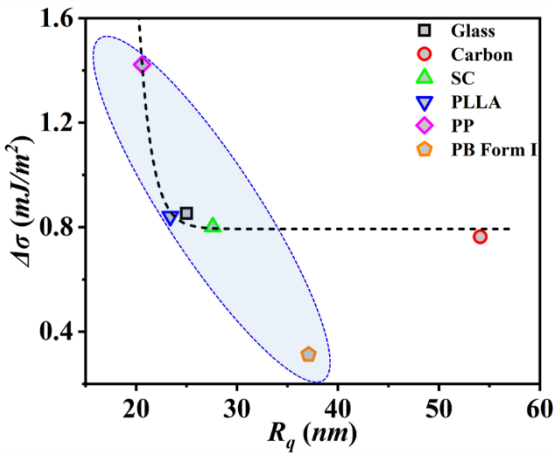

Figure 6.8 Plot of the interfacial free-energy difference ($\Delta\sigma$) as a function of roughness (R_q) for all of the investigated fibers.

It should be noted that the $\Delta\sigma$ of the Form I PB-1 fiber is extremely low, in comparison with other fibers, if its specific roughness is taken into account. We can attribute it to the cross-nucleation of the PB-1 Form II fiber onto the Form I fiber occurring via an epitaxial mechanism, which has been proved in Chapters 4 and 5. Another widely studied factor is the intrinsic surface chemical characteristic of the various fibers, which plays an important role in the interfacial nucleation activation of a given polymer matrix on the surface of fibers. For example, Maiti et al.[44] studied the crystallization behavior of nylon-6/clay nanocomposites. They found that the formation of hydrogen bonds between the clay and nylon-6 on the interface could promote the formation of a γ-form crystal of nylon-6 on the surface of clay and accelerate the nucleation rate.

In this chapter, we adopted two different systems that should provide evidence on the role of surface chemistry, being chemically identical in pairs. The first system is PLLA/SC fibers. Although stereocomplex (SC) is prepared through the blend of the two different enantiomeric

forms of PLLA and PDLA, the chemical characteristic is the same for SC and PLLA. If chemical structure plays a dominant role in nucleation, these PB-1/fiber composites will present the same $\Delta\sigma$. This is actually the case, as can be seen in Figure 6.8 and Table 6.1, despite the difference in surface roughness of about 15%. However, the second example contradicts this finding. In fact, if we consider the chemically similar PP and PB-1, the greatest difference in $\Delta\sigma$ among all the systems is observed, despite the fact that they only differ in one methyl group. This notwithstanding, as previously discussed, Form I PB-1 fibers are anomalously efficient in nucleating Form II, due to the existence of an epitaxial relationship. Therefore, chemical structure could actually influence nucleation on fibers, as demonstrated by PLLA and SC, but its effect could be overwhelmed by more specific interactions, such as epitaxy. We note that the specific surface chemistry might play a role in nucleation on the surface of fibers, mainly through the formation of intermolecular interaction, like hydrogen bonds or polar interactions.

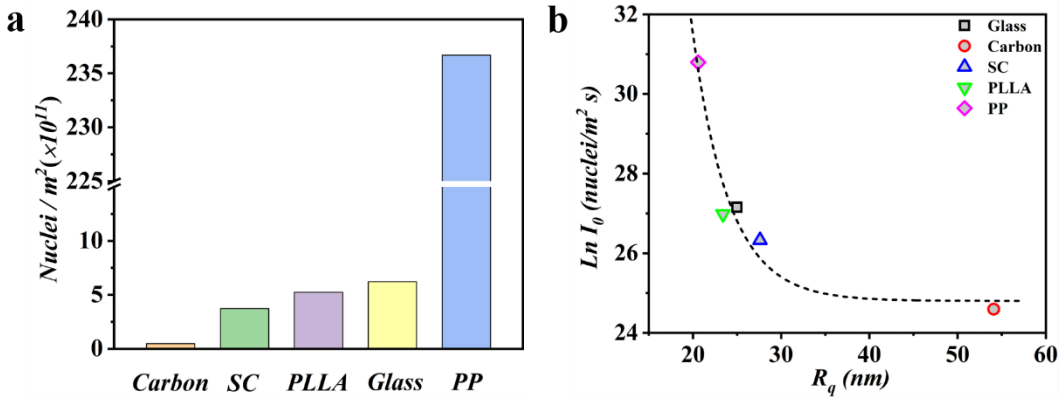

Figure 6.9 (a) Specific number of nuclei of different fibers in the surface-induced nucleation process. (b) Plot of the logarithm of potential nucleation sites ($Ln(I_0)$) as a function of the roughness (R_q) for different fibers.

Classical nucleation theory (CNT) expresses the nucleation rate per unit volume or area as the product of a double-exponential factor and a pre-exponential factor, as in equation (6.1). The double-exponential factor is $\exp\left(-\frac{U^*}{R(T-T_\infty)}\right)\exp\left(-\frac{16\sigma\sigma_e\Delta\sigma T_m^{0^2}}{kTf^2\Delta T^2\Delta h_0^2}\right)$, which has been used to define the probability of PB-1 Form II nucleation on the fiber surface taking into account the free-energy cost for nucleus formation. However, no in-depth discussion about the pre-exponential (I_0) and its physical meaning has been provided in the literature. In the case of homogeneous (volume) nucleation, the pre-exponential factor is the product of three terms (I_0

= ρjZ): the number density of molecules ρ, the rate at which molecules attach to the nucleus causing it to grow, j, and the Zeldovich factor Z, which is a probabilistic term. The number density of molecules ρ is essentially the number of possible nucleation sites per unit volume since in homogeneous nucleation, the nucleus can form around any of the molecules. However, in classical heterogeneous nucleation, the pre-exponential factor I_0 does not contain the number density of molecules ρ, but rather the number density of sites for heterogeneous nucleation, ρ_i, given by the number density of impurities times the number of places where a critical nucleus can form on each impurity.[82-84] Therefore, it is plausible to consider this pre-exponential factor (I_0) as representative of the possible nucleating sites on the fiber surface area.

To understand the difference in the calculated potential nucleation sites on the different types of fiber, we compare these values in detail in Figure 6.9a. For the sake of comparison, the rate constant in I_0 (i.e., j) has been considered to be equal to one, being a characteristic of the polymer and equal for every system, in principle. The standard HSC structure in the PB-1/carbon composites possesses the minimum of nucleation sites with 0.4×10^{11} nuclei/m^2 s. However, for most of the fibers (PLLA, SC and glass fibers), the value of I_0 is largely constant on the order of 10^{11} nuclei/m^2 s, which is one order of magnitude bigger than that of carbon fiber. Remarkably, the number of nucleation sites on the PP fiber is far greater than that of all the other fibers, being two or three orders of magnitude higher. The amount of nucleation sites of the Form I fiber which cannot be easily compared with other fibers due to the different estimation parameters used in equations (6.1) and (6.2), but it could be deduced that the effective sites must be several orders of magnitude larger than that of PP fiber, based on the TCL morphology shown in Figure 6.2.

Figure 6.9b shows the evolution of potential nucleation sites as a function of the roughness for different fibers. It is noteworthy to observe an inverse relationship between the $Ln(I_0)$ and roughness (R_q), with the number of nucleation sites per unit area decreasing exponentially with increasing roughness. Wang et al. have identified the potential nucleation sites to the groove structure of a fiber's surface topography, with the requirement that, for heterogeneous nucleation to take place, the dimensions of the groove should be sufficient to host the stable nuclei.[15, 25] A certain degree of commensurability between valley/ridges size and nuclei dimensions might explain the higher number of nucleation sites for lower roughness values. To explain the inverse relationship in Figure 6.9b, we can make some rough assumptions. At a first approximation, the number of effective nucleation sites (I_0) approximately equals the concentration of grooves satisfying the above size criteria. Considering a continuous

alternating groove and ridge topography, the number of grooves will be related both to the average height of valleys and the width of the grooves. For the sake of simplicity, the topography is represented as upward triangles in Appendix C8 and the number of grooves over the unit length is equal to the reciprocal of the valley width ($2l$). With reference to the scheme of Appendix C8, this is given by $2R_q/tan\theta$, where θ is the internal angle between the fiber surface and the groove. Thus, I_0 is proportional to $tan\theta/2R_q$. This function explains at least the general trend observed in Figure 6.9b, although the precise relationship between I_0 and roughness cannot be captured by such a simple and schematic model.

We highlight that a high number of possible nucleation sites does not necessarily mean a high nucleation ability. In fact, besides the number of available sites, the free-energy barrier for nucleus formation (i.e., $\Delta\sigma$) is of importance. Interestingly, as deduced from Figures 6.8 and 6.9b, a connection between the free-energy difference ($\Delta\sigma$) and the effective nucleation sites (I_0) is expected. In Appendix C9, we can find empirically a positive correlation between the free-energy barrier and the number of available nucleation sites. The physical reason for such a dependency is unclear, but it can be tentatively linked to the scale of the roughness, as a working hypothesis. In fact, from Figure 6.9b, we can see that the highest number of nucleation sites is associated with the lowest R_q values. Assuming again that groove and ridge structures alternate in succession, if there are many nucleation sites on the surface of the fiber, such as in the PP fiber, the space between two grooves will become very narrow. It can thus be assumed that the polymer matrix is able to wet less efficiently a substrate with this type of topography since the diffusion of chain segments to the inner part of the grooves will be hindered, similar to the situation that occurs during the infiltration of a polymer into anodic aluminum oxide (AAO) templates, which becomes increasingly slow with a decrease in pore size.[85] Therefore, this partial wetting would cause a higher apparent $\Delta\sigma$, although the interactions of the polymer with an ideally flat substrate of the fiber would be more favorable. On the contrary, most or all the large-sized grooves are easy locations to induce nucleation, for instance, in the case of the carbon fiber, due to the higher wettability of the fiber surface. We note that this discussion on roughness and available nucleation sites does not apply to the PB-1 Form I fiber, for which any point of the surface is a potential nucleation site, due to the occurrence of epitaxial match with Form II.

Now that the details of fiber-induced nucleation toward PB-1 have been elucidated, the origin of TCL morphology in this polymer can be discussed, with particular emphasis on the relationship between potential nucleation sites and transcrystalline layer formation.

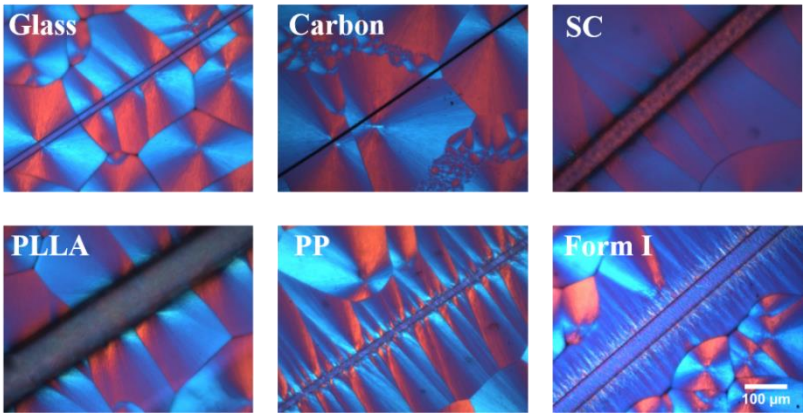

Figure 6.10 Crystallization morphology of various PB-1/fiber composites after cooling to room temperature.

Figure 6.10 shows the morphology of PB-1 Form II crystallizing on the surface of different fibers after cooling from the melt to room temperature at 20 °C/min (i.e., non-isothermal nucleation and growth). An evident TCL structure is observed in the composite with the Form I fiber, which is consistent with that observed during isothermal crystallization. Interestingly, TCL morphology is also found to appear on the surface of the PP fiber, although the linear density of the crystals is not as high as that on the Form I fiber. For carbon fiber, the standard HSC structure is still obtained during non-isothermal crystallization, while a relatively dense HSC morphology appears in the three composites, including PLLA, SC, and glass fibers. It is easily confirmed that the different morphologies are in line with the number of potential nucleation sites as determined from the nucleation kinetics measurement via equation (6.1). In fact, this number is the highest for PP, of the same order of magnitude for PLLA, SC, and glass, and the lowest in the case of carbon fibers. A clear link is established for the first time. We note that the free-energy barrier for critical nucleus formation decreases with the increasing of the supercooling.

At this stage, the different PB-1 nucleation processes and morphologies on the various fibers can be explained through the schematic of Figure 6.11. In most of the fibers (PLLA, SC, carbon, and glass), there is enough space between two adjacent nucleation grooves, which have a relatively low density. Thus, the crystals that initially develop on these fibers are allowed to grow along any direction, until they impinge on each other, forming the hybrid “shish–calabash” structure (HSC). Next, the PP fiber possesses the highest content of nucleation sites in Figure 6.9, on the basis of a surface roughness measurement, so that the adjacent space between them is small. Therefore, individual Form II crystallites that developed in these nucleation sites are forced to grow along the direction perpendicular to the fiber due to the spatial constraint.

Correspondingly, TCL morphology with relatively wide Form II crystals can be observed. In the case of the Form I fiber, although the amount of grooves is expected to be at the intermediate level, as inferred from the value of roughness, the more obvious TCL structure with very narrowly spaced Form II crystals is present on the interface. This reveals that the interaction between the PB-1 matrix and the Form I fiber is much stronger than that between PB-1 and other fibers, even though only relatively few grooves are available on the fiber surface. This is reasonably attributed, as previously discussed in Chapters 4 and 5, to the existence of cross-nucleation between the PB-1 Form II and Form I fibers, linked to epitaxial crystallization.[45] As shown in the bottom row of Figure 6.11, nucleation sites are not limited to the grooves and any position of the fiber surface that satisfies the epitaxial condition is an effective nucleation site. This is in accordance, for instance, with the result of the work of Hu et al., who studied the nucleation of PCL films in contact with PE and iPP substrates. They demonstrated much higher nucleation ability of PE with respect to iPP for PCL because the better lattice matching between PCL and PE resulted in the existence of a much larger number of active nucleation sites.[86]

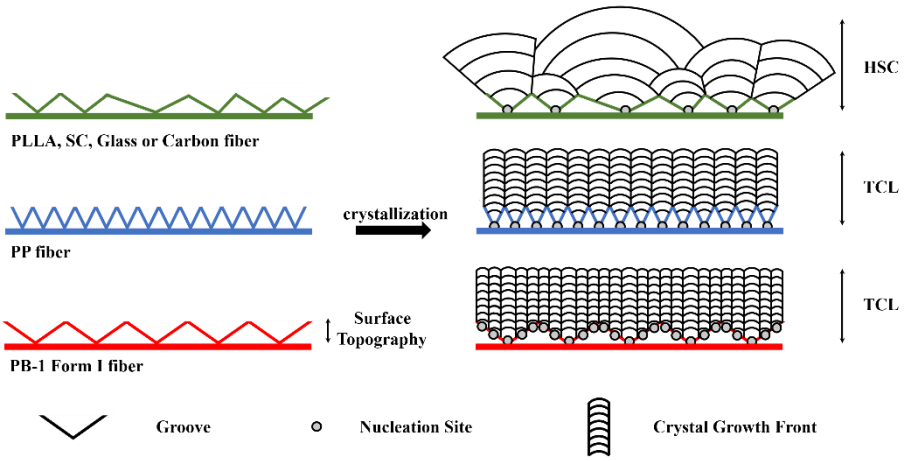

Figure 6.11 Schematic illustration of the nucleation of PB-1 Form II onto different fibers.

It is thus apparent that possessing a low energy barrier alone is not enough to lead to TCL formation. In fact, judging from the $\Delta\sigma$, the ability of the carbon fiber to induce nucleation would be the best, whereas the PP fiber should exhibit the weakest nucleation ability toward PB-1. However, HSC and TCL morphologies are respectively observed in the two fibers during cooling, contrary to the expectation based on $\Delta\sigma$. In these examples, the large difference of available nucleation sites (about three orders of magnitude) completely overwhelms the contribution from the free-energy barrier, leading to unexpected morphologies.

6.4 Conclusion

The present chapter focused on the nucleation process of PB-1 at the surface of various fibers. Direct evidence was obtained via PLOM observations and revealed that a transcrystalline layer is induced by the PB-1 Form I fiber, and a hybrid shish–calabash structure is induced by other carbon, glass, PP, PLLA, and stereocomplex fibers during isothermal crystallization.

Based on a quantitative analysis of the nucleation kinetics, it was found that the nucleation free-energy barrier is affected by surface roughness, surface chemistry and specific interactions, such as epitaxy. Moreover, the observed different crystalline morphologies on the various fibers are proposed to be linked to the number of available nucleation sites on the rough surface (grooves). In particular, it is shown for the first time that regardless of the height of the free-energy barrier, the presence of a high density of nucleation sites along the fiber is mandatory to obtain a transcrystalline morphology.

References

[1] T. Kwei, H. Schonhorn, H. Frisch, Dynamic mechanical properties of the transcrystalline regions in two polyolefins, Journal of Applied Physics 38(6) (1967) 2512-2516.

[2] M. Folkes, S. Hardwick, The mechanical properties of glass/polypropylene multilayer laminates, Journal of Materials Science 25(5) (1990) 2598-2606.

[3] T. Hata, K. Ohsaka, T. Yamada, K. Nakamae, N. Shibata, T. Matsumoto, Transcrystalline region of polypropylene: its formation, structure and mechanical properties, The Journal of Adhesion 45(1-4) (1994) 125-135.

[4] S. Saeidlou, M.A. Huneault, H. Li, P. Sammut, C.B. Park, Evidence of a dual network/spherulitic crystalline morphology in PLA stereocomplexes, Polymer 53(25) (2012) 5816-5824.

[5] Y. Qin, Y. Xu, L. Zhang, G. Zheng, K. Dai, C. Liu, X. Yan, J. Guo, Z. Guo, Shear-induced interfacial sheath structure in isotactic polypropylene/glass fiber composites, Polymer 70 (2015) 326-335.

[6] Y. Qin, Y. Xu, L. Zhang, G. Zheng, X. Yan, K. Dai, C. Liu, C. Shen, Z. Guo, Interfacial interaction enhancement by shear-induced β-cylindrite in isotactic polypropylene/glass fiber composites, Polymer 100 (2016) 111-118.

[7] T. Gao, Z.M. Zhang, L. Li, R.Y. Bao, Z.Y. Liu, B.H. Xie, M.B. Yang, W. Yang, Tailoring crystalline morphology by high-efficiency nucleating fiber: toward high-performance poly (l-

lactide) biocomposites, ACS applied materials & interfaces 10(23) (2018) 20044-20054.
[8] T. Gao, S.J. Zhao, R.Y. Bao, G.J. Zhong, Z.M. Li, M.B. Yang, W. Yang, Constructing sandwich-architectured poly (l-lactide)/high-melting-point poly (l-lactide) nonwoven fabrics: toward heat-resistant poly (l-lactide) barrier biocomposites with full biodegradability, ACS Applied Bio Materials 2(3) (2019) 1357-1367.
[9] N. Ning, S. Fu, W. Zhang, F. Chen, K. Wang, H. Deng, Q. Zhang, Q. Fu, Realizing the enhancement of interfacial interaction in semicrystalline polymer/filler composites via interfacial crystallization, Progress in Polymer Science 37(10) (2012) 1425-1455.
[10] H. Quan, Z.M. Li, M.B. Yang, R. Huang, On transcrystallinity in semi-crystalline polymer composites, Composites Science and Technology 65(7-8) (2005) 999-1021.
[11] C. Wang, L. Hwang, Transcrystallization of PTFE fiber/PP composites (I) crystallization kinetics and morphology, Journal of Polymer Science Part B: Polymer Physics 34(1) (1996) 47-56.
[12] C. Wang, C. Liu, Transcrystallization of polypropylene on carbon fibres, Polymer 38(18) (1997) 4715-4718.
[13] C. Wang, Y.J. Wu, C.Y. Fang, C.W. Tsai, Electrospun nanofiber-reinforced polypropylene composites: nucleating ability of nanofibers, Composites Science and Technology 126 (2016) 1-8.
[14] C. Wang, C.R. Liu, Transcrystallization of polypropylene composites: nucleating ability of fibres, Polymer 40(2) (1999) 289-298.
[15] C. Wang, F.H. Liu, W.H. Huang, Electrospun-fiber induced transcrystallization of isotactic polypropylene matrix, Polymer 52(5) (2011) 1326-1336.
[16] C. He, X. Dong, X. Zhang, D. Wang, D. Xu, Morphology investigation of transcrystallinity at polyamide 66/aramid fiber interface, Journal of Applied Polymer Science 91(5) (2004) 2980-2983.
[17] H. Shi, Y. Zhao, X. Dong, C. He, D. Wang, D. Xu, Transcrystalline morphology of nylon 6 on the surface of aramid fibers, Polymer International 53(11) (2004) 1672-1676.
[18] C. Wang, C. Liu, C. Chen, L. Hawang, Transcrystallinity in PTFE fiber/PP composites, The Journal of Adhesion 67(1-4) (1998) 167-180.
[19] T. Wen, G. Liu, Y. Zhou, X. Zhang, F. Wang, H. Chen, J. Loos, D. Wang, Epitaxy-induced crystallization of olefin block copolymers, Macromolecules 45(15) (2012) 5979-5985.
[20] Z. Guo, S. Li, X. Liu, J. Zhang, H. Li, X. Sun, Z. Ren, S. Yan, Epitaxial crystallization of isotactic poly (methyl methacrylate) from different states on highly oriented polyethylene thin film, The Journal of Physical Chemistry B 122(40) (2018) 9425-9433.

[21] J. Liu, J. Wang, H. Li, D. Shen, J. Zhang, Y. Ozaki, S. Yan, Epitaxial crystallization of isotactic poly (methyl methacrylate) on highly oriented polyethylene, The Journal of Physical Chemistry B 110(2) (2006) 738-742.

[22] N. Zafeiropoulos, C. Baillie, J. Hodgkinson, Engineering and characterisation of the interface in flax fibre/polypropylene composite materials. Part II. The effect of surface treatments on the interface, Composites part A: applied science and manufacturing 33(9) (2002) 1185-1190.

[23] M. Zhou, Y. Li, C. He, T. Jin, K. Wang, Q. Fu, Interfacial crystallization enhanced interfacial interaction of poly (butylene succinate)/ramie fiber biocomposites using dopamine as a modifier, Composites Science and Technology 91 (2014) 22-29.

[24] M. Huson, W. McGill, Transcrystallinity in polypropylene, Journal of Polymer Science: Polymer Chemistry Edition 22(11) (1984) 3571-3580.

[25] B. Wang, T. Wen, X. Zhang, A. Tercjak, X. Dong, A.J. Müller, D. Wang, D. Cavallo, Nucleation of Poly (lactide) on the Surface of Different Fibers, Macromolecules 52(16) (2019) 6274-6284.

[26] C. Lin, S. Ding, Y. Hwang, Interfacial crystallization of isotactic polypropylene molded against the copper surface with various surface roughnesses prepared by an electrochemical process, Journal of materials science 36(20) (2001) 4943-4948.

[27] C. Lin, Y. Lai, S. Liu, Effect of the surface roughness of sulfuric acid-anodized aluminum mold on the interfacial crystallization behavior of isotactic polypropylene, Journal of Adhesion Science and Technology 15(8) (2001) 929-944.

[28] N. Ning, F. Luo, K. Wang, Q. Zhang, F. Chen, R. Du, C. An, B. Pan, Q. Fu, Molecular weight dependence of hybrid shish kebab structure in injection molded bar of polyethylene/inorganic whisker composites, The Journal of Physical Chemistry B 112(45) (2008) 14140-14148.

[29] N. Ning, H. Deng, F. Luo, K. Wang, Q. Zhang, F. Chen, Q. Fu, Effect of whiskers nucleation ability and shearing function on the interfacial crystal morphology of polyethylene (PE)/raw whiskers composites, Composites Part B: Engineering 42(4) (2011) 631-637.

[30] N. Ning, F. Luo, K. Wang, R. Du, Q. Zhang, F. Chen, Q. Fu, Interfacial enhancement by shish–calabash crystal structure in polypropylene/inorganic whisker composites, Polymer 50(15) (2009) 3851-3856.

[31] N. Ning, H. Deng, F. Luo, Q. Zhang, K. Wang, F. Chen, Q. Fu, The interfacial enhancement of LLDPE/whisker composites via interfacial crystallization, Polymers for Advanced Technologies 23(3) (2012) 431-440.

[32] M. Folkes, S. Hardwick, The molecular weight dependence of transcrystallinity in fibre reinforced thermoplastics, Journal of Materials Science Letters 3(12) (1984) 1071-1073.
[33] C.k. Moon, Effect of molecular weight and fiber diameter on the interfacial behavior in glass fiber/PP composites, Journal of Applied Polymer Science 67(7) (1998) 1191-1197.
[34] T. Bessell, J. Shortall, The crystallization and interfacial bond strength of nylon 6 at carbon and glass fibre surfaces, Journal of materials science 10(12) (1975) 2035-2043.
[35] P. Frayer, J. Lando, Polymerization in electric fields of hexanethylene diammonium adipate crystallized on graphite fibers, Journal of Polymer Science Part B: Polymer Letters 10(1) (1972) 29-34.
[36] Y. Cai, J. Petermann, H. Wittich, Transcrystallization in fiber-reinforced isotactic polypropylene composites in a temperature gradient, Journal of Applied Polymer Science 65(1) (1997) 67-75.
[37] A.C. Brosse, S. Tencé-Girault, P.M. Piccione, L. Leibler, Effect of multi-walled carbon nanotubes on the lamellae morphology of polyamide-6, Polymer 49(21) (2008) 4680-4686.
[38] C.Y. Li, L. Li, W. Cai, S.L. Kodjie, K.K. Tenneti, Nanohybrid shish-kebabs: Periodically functionalized carbon nanotubes, Advanced Materials 17(9) (2005) 1198-1202.
[39] C. Wang, C.Y. Fang, C.Y. Wang, Electrospun poly (butylene terephthalate) fibers: Entanglement density effect on fiber diameter and fiber nucleating ability towards isotactic polypropylene, Polymer 72 (2015) 21-29.
[40] T. Wen, Z. Xiong, G. Liu, X. Zhang, S. de Vos, R. Wang, C.A. Joziasse, F. Wang, D. Wang, The inexistence of epitaxial relationship between stereocomplex and α crystal of poly (lactic acid): Direct experimental evidence, Polymer 54(7) (2013) 1923-1929.
[41] H. Ishida, P. Bussi, Induction time approach to surface induced crystallization in polyethylene/poly (ε-caprolactone) melt, Journal of Materials Science 26(23) (1991) 6373-6382.
[42] H. Ishida, P. Bussi, Surface induced crystallization in ultrahigh-modulus polyethylene fiber-reinforced polyethylene composites, Macromolecules 24(12) (1991) 3569-3577.
[43] X. Zheng, Q. Xu, Comparison study of morphology and crystallization behavior of polyethylene and poly (ethylene oxide) on single-walled carbon nanotubes, The Journal of Physical Chemistry B 114(29) (2010) 9435-9444.
[44] P. Maiti, M. Okamoto, Crystallization controlled by silicate surfaces in nylon 6-clay nanocomposites, Macromolecular Materials and Engineering 288(5) (2003) 440-445.
[45] W. Wang, B. Wang, E. Carmeli, Z. Wang, Z. Ma, D. Cavallo, Cross-nucleation of polybutene-1 Form II on Form I seeds with different morphology, Polymer Crystallization 3(2)

(2020) e210104.

[46] H.Y. Yu, H. Zhang, M.L. Song, Y. Zhou, J. Yao, Q.Q. Ni, From cellulose nanospheres, nanorods to nanofibers: various aspect ratio induced nucleation/reinforcing effects on polylactic acid for robust-barrier food packaging, ACS applied materials & interfaces 9(50) (2017) 43920-43938.

[47] E.J. Chen, B.S. Hsiao, The effects of transcrystalline interphase in advanced polymer composites, Polymer Engineering & Science 32(4) (1992) 280-286.

[48] K. Cho, D. Kim, S. Yoon, Effect of substrate surface energy on transcrystalline growth and its effect on interfacial adhesion of semicrystalline polymers, Macromolecules 36(20) (2003) 7652-7660.

[49] A. Gati, H. Wagner, Stress transfer efficiency in semicrystalline-based composites comprising transcrystalline interlayers, Macromolecules 30(13) (1997) 3933-3935.

[50] G. Natta, P. Pino, P. Corradini, F. Danusso, E. Mantica, G. Mazzanti, G. Moraglio, Crystalline high polymers of α-olefins, Journal of the American Chemical Society 77(6) (1955) 1708-1710.

[51] R. Xin, J. Zhang, X. Sun, H. Li, Z. Ren, S. Yan, Polymorphic behavior and phase transition of poly (1-butene) and its copolymers, Polymers 10(5) (2018) 556.

[52] A.T. Jones, Polybutene-1–type II crystalline form, Journal of Polymer Science Part B: Polymer Letters 1(8) (1963) 455-456.

[53] V. Holland, R.L. Miller, Isotactic polybutene-1 single crystals: morphology, Journal of Applied Physics 35(11) (1964) 3241-3248.

[54] K. Tashiro, J. Hu, H. Wang, M. Hanesaka, A. Saiani, Refinement of the crystal structures of forms I and II of isotactic polybutene-1 and a proposal of phase transition mechanism between them, Macromolecules 49(4) (2016) 1392-1404.

[55] F. Danusso, G. Gianotti, Isotactic polybutene-1: Formation and transformation of modification 2, Die Makromolekulare Chemie: Macromolecular Chemistry and Physics 88(1) (1965) 149-158.

[56] B. Wang, T. Wen, X. Zhang, A. Tercjak, X. Dong, A.J. Müller, D. Wang, D. Cavallo, Nucleation of Poly (lactide) on the Surface of Different Fibers, Macromolecules 52(16) (2019) 6274-6284.

[57] W. Wang, L. Zheng, L. Liu, W. Li, Y. Li, Z. Ma, Stretching behavior of the butene-1/ethylene random copolymer: A direct correspondence between triggering of II-I phase transition and mechanical yielding, Polymer Crystallization 2(2) (2019) e10052.

[58] L. Zheng, L. Liu, C. Shao, W. Wang, B. Wang, L. Pan, Y. Li, Z. Ma, Phase transition from

tetragonal form II to hexagonal form I of butene-1/4-methyl-1-pentene random copolymers: Molecular factor versus stretching stimuli, Macromolecules 52(3) (2019) 1188-1199.

[59] W. Wang, C. Shao, L. Zheng, B. Wang, L. Pan, G. Ma, Y. Li, Y. Wang, C. Liu, Z. Ma, Stretching-induced phase transition of the butene-1/ethylene random copolymer: Orientation and kinetics, Journal of Polymer Science Part B: Polymer Physics 57(2) (2019) 116-126.

[60] W. Li, L. Liu, L. Zheng, Y. Lou, Z. Ma, Y. Li, Interplay between Macroscopic Stretching and Microscopic Phase Transition Revealed in Butene-1/1, 5-Hexadiene Random Copolymers, Macromolecules 53(6) (2020) 2145-2156.

[61] F. Azzurri, A. Flores, G. Alfonso, F. Baltá Calleja, Polymorphism of isotactic poly (1-butene) as revealed by microindentation hardness. 1. Kinetics of the transformation, Macromolecules 35(24) (2002) 9069-9073.

[62] Y. Qiao, Y. Men, Intercrystalline links determined kinetics of form II to I polymorphic transition in polybutene-1, Macromolecules 50(14) (2017) 5490-5497.

[63] F. Azzurri, A. Flores, G. Alfonso, I. Sics, B. Hsiao, F.B. Calleja, Polymorphism of isotactic polybutene-1 as revealed by microindentation hardness. Part II: correlations to microstructure, Polymer 44(5) (2003) 1641-1645.

[64] Y. Wang, Y. Lu, J. Zhao, Z. Jiang, Y. Men, Direct formation of different crystalline forms in butene-1/ethylene copolymer via manipulating melt temperature, Macromolecules 47(24) (2014) 8653-8662.

[65] Y.T. Wang, P.R. Liu, Y. Lu, Y.F. Men, Mechanism of polymorph selection during crystallization of random butene-1/ethylene copolymer, Chinese Journal of Polymer Science 34(8) (2016) 1014-1020.

[66] H. Li, X. Zhang, X. Kuang, J. Wang, D. Wang, L. Li, S. Yan, A scanning electron microscopy study on the morphologies of isotactic polypropylene induced by its own fibers, Macromolecules 37(8) (2004) 2847-2853.

[67] W. Wang, Z. Qi, G. Jeronimidis, Studies on interface structure and crystal texture of poly (ether-ether-ketone)-carbon fibre composite, Journal of materials science 26(21) (1991) 5915-5920.

[68] S. Machida, Y. Matsuda, S. Tasaka, Gelation of a composite of ceramic fibers and polypropylene modified with maleic anhydrate in naphthenic oil, Chemistry Letters 38(1) (2009) 70-71.

[69] C.C. Jeng, M. Chen, Flexural failure mechanisms in injection-moulded carbon fibre/PEEK composites, Composites Science and Technology 60(9) (2000) 1863-1872.

[70] R. Zhang, Y. Huang, M. Min, Y. Gao, X. Yu, A. Lu, Z. Lu, Isothermal crystallization of

pure and glass fiber reinforced poly (phenylene sulfide) composites, Polymer Composites 30(4) (2009) 460-466.

[71] A. Choudhury, Isothermal crystallization and mechanical behavior of ionomer treated sisal/HDPE composites, Materials Science and Engineering: A 491(1-2) (2008) 492-500.

[72] H.C. Cartledge, C.A. Baillie, Studies of microstructural and mechanical properties of nylon/glass composite Part I The effect of thermal processing on crystallinity, transcrystallinity and crystal phases, Journal of materials science 34(20) (1999) 5099-5111.

[73] B. Yan, H. Wu, G. Jiang, S. Guo, J. Huang, Interfacial crystalline structures in injection over-molded polypropylene and bond strength, ACS applied materials & interfaces 2(11) (2010) 3023-3036.

[74] A. Chatterjee, F. Price, S. Newman, Heterogeneous nucleation of crystallization of high polymers from the melt. II. Aspects of transcrystallinity and nucleation density, Journal of Polymer Science: Polymer Physics Edition 13(12) (1975) 2385-2390.

[75] A. Chatterjee, F. Price, S. Newman, Heterogeneous nucleation of crystallization of high polymers from the melt. III. Nucleation kinetics and interfacial energies, Journal of Polymer Science: Polymer Physics Edition 13(12) (1975) 2391-2400.

[76] F. Binsbergen, Heterogeneous nucleation in the crystallization of polyolefins. III. Theory and mechansim, Journal of Polymer Science: Polymer Physics Edition 11(1) (1973) 117-135.

[77] I. Stolte, R. Androsch, M.L. Di Lorenzo, Spherulite growth rate and fold surface free energy of the form II mesophase in isotactic polybutene-1 and random butene-1/ethylene copolymers, Colloid and Polymer Science 292(6) (2014) 1479-1485.

[78] E.J. Clark, J.D. Hoffman, Regime III crystallization in polypropylene, Macromolecules 17(4) (1984) 878-885.

[79] T. Sukhanova, F. Lednický, J. Urban, Y. Baklagina, G. Mikhailov, V. Kudryavtsev, Morphology of melt crystallized polypropylene in the presence of polyimide fibres, Journal of materials science 30(9) (1995) 2201-2214.

[80] C. Wang, C.R. Liu, Transcrystallization of PTFE fiber/PP composites—III. Effect of fiber pulling on the crystallization kinetics, Journal of Polymer Science Part B: Polymer Physics 36(8) (1998) 1361-1370.

[81] C. Lin, Y. Du, Effect of surface topographies of PTFE and polyimide as characterized by atomic force microscopy on the heterogeneous nucleation of isotactic polypropylene, Materials chemistry and physics 58(3) (1999) 268-275.

[82] D.W. Oxtoby, Homogeneous nucleation: theory and experiment, Journal of Physics: Condensed Matter 4(38) (1992) 7627.

[83] J.M. Garcıa-Ruiz, Nucleation of protein crystals, Journal of Structural Biology 142(1) (2003) 22-31.

[84] D.W. Oxtoby, Nucleation of first-order phase transitions, Accounts of Chemical Research 31(2) (1998) 91-97.

[85] C.H. Tu, M. Steinhart, H.J. Butt, G. Floudas, In Situ Monitoring of the Imbibition of Poly (n-butyl methacrylates) in Nanoporous Alumina by Dielectric Spectroscopy, Macromolecules 52(21) (2019) 8167-8176.

[86] J. Hu, R. Xin, C.Y. Hou, S.K. Yan, J.C. Liu, Direct comparison of crystal nucleation activity of PCL on patterned substrates, Chinese Journal of Polymer Science 37(7) (2019) 693-699.

Chapter 7. Rigid amorphous fraction in polymorphic polybutene-1

7.1 Introduction

Most semicrystalline polymers have a three-phase structure made of crystals and amorphous regions with different mobility.[1, 2] The nanometer-scale arrangement of polymer crystals involves chain folding, since the polymer molecules are much longer than the crystal nanophases. The partially immobilized amorphous chain portions coupled to the crystals are named rigid amorphous fraction (RAF), because of the reduced number of their possible conformational arrangements. The amorphous regions decoupled from the crystals, named mobile amorphous fraction (MAF), can be easily recognized and quantified by temperature-dependent analysis, being associated to a sharp change of material properties, like heat capacity, elastic modulus, etc., which occur in a relatively narrow temperature range of about 20-40 °C, and is identified with a characteristic temperature, named glass transition temperature (T_g).[3, 4] Most commonly, the MAF is quantified by comparing the heat capacity (C_p) step at T_g, with the C_p step of the fully amorphous polymer.[4] The RAF, instead, does not contribute to the increase in heat capacity at T_g, remaining glassy above this temperature. However, the similarity to the MAF is that the RAF also largely affects material properties. Unfortunately, its vitrification/devitrification does not occur within an easily identifiable temperature range. For this reason, the amount of RAF (w_{RAF}) is generally quantified by difference, once the amount of crystalline (w_C) and mobile amorphous (w_{MAF}) fractions are known, being $w_{RAF} + w_{MAF} + w_C = 1$.[5] Moreover, despite RAF has been identified in almost all semicrystalline polymers, its vitrification/devitrification range is known only for a limited number of polymers.

The rigid amorphous fraction is established at the crystal basal planes.[6] The size of amorphous layer with limited mobility may largely vary from polymer to polymer, being controlled by chain architecture, i.e., by the inherent flexibility of the macromolecule,[2, 7, 8] by crystal fraction, structure and morphology,[5] which usually vary with thermal history. The relationship between crystal growth and rigid amorphous fraction development has been detailed in the literature for several semicrystalline polymers,[2] with quantitative data on kinetics of vitrification of the RAF in dependence of crystal growth now available for a variety of systems.[5, 9-27] Besides the differences due to the specific features of each polymer, literature data agree on the establishment of a large RAF upon fast crystallization, or upon

crystallization at low temperature, where chain mobility is reduced, i.e., when internal stresses are not released during crystal growth, and concentrate at the interface between the crystal and the amorphous phases.[5]

Controversial data appeared in the literature on the kinetics of RAF mobilization, and its relation to crystal melting. Mobilization of the rigid amorphous fraction often overlaps melting of the coupled crystals, but can occur also in a well separated temperature range.[28-30] In isothermally crystallized samples, a small endotherm (sometimes called "annealing peak") is often observed during heating at about 10-30 °C above the crystallization temperature. This small thermal event has been identified in a number of polymers, including poly(phenylene sulfide),[31] poly(ethylene terephthalate),[32, 33] polyamide 6,[34] bisphenol A polycarbonate,[12, 35] poly(3-hydroxybutyrate),[12] but its nature is still under debate; some authors associate it to melting of secondary, or more defective/thinner crystals,[36-38] others link it to enthalpy recovery of the RAF.[33, 39, 40]

Being for most polymers the vitrification and the devitrification range of the RAF unknown, doubts may remain whether at the temperature of the annealing peak, RAF portions are still vitrified, thus really contributing to the annealing peak. On the other hand, quantitative data on the physical aging of the RAF, to our knowledge, are available to date only for poly(3-hexylthiophene)[41] and poly(L-lactic acid)[42], despite aging in semicrystalline polymers at temperatures below T_g is known since the late 1970s and 80s.[43-45] Aging of a glass is understood by considering the change in its enthalpic state, which decreases towards the (metastable equilibrium) enthalpy value of the supercooled liquid at that temperature, as shown in Appendix D1.

As an effort to contribute to a deeper understanding of the RAF and its relationship with thermal properties of the coupled crystals, data on physical aging of the RAF of PB-1 are presented and discussed in this chapter. PB-1 represents an ideal candidate for the study of physical aging of the RAF, because this polymer presents crystal polymorphism, which sizably affects also vitrification of the coupled RAF, and quantitative data are available in the literature on the thermal stability of the RAF coupled to each specific crystal form.[28, 29, 46]

Upon cooling from the melt, PB-1 develops a conformationally disordered (condis) crystal structure, named Form II, with a tetragonal crystalline lattice.[47, 48] Form II condis crystals are metastable and spontaneously transform to a twinned trigonal structure (Form I) with a change in molecular conformation from the 11_3 helix in Form II to the 3_1 helix structure in Form I.[49-52] Transformation of the condis crystals into the stable trigonal modification affects the amorphous segments, as the increased density and thermal stability of the crystals

cause a higher rigidity of the coupled amorphous areas, which also affects T_g of the MAF.[29] A higher RAF content is coupled more strongly to the rigid Form I crystals and relaxes at higher temperatures compared with the polymer containing modification II crystals.[29] The RAF coupled to Form II is completely devitrified around 50 °C, well below the onset of melting of Form II crystals, which implies that any endothermic peak measured at temperatures higher than 50 °C in a sample containing only Form II crystals can be ascribed only to thermal events involving the crystals, and not the RAF. On the other hand, the RAF coupled to Form I crystals devitrifies at higher temperatures, with complete mobilization only around 100 °C, i.e., close to the onset of crystal melting, and annealing at higher temperatures can only lead to crystal perfection/thickening.[29]

The present study focuses on the difference of physical aging of PB-1 RAF coupled with either Form II or Form I crystals in a wide temperature range. It aims to confirm the earlier literature information on the influence of crystal modification of PB-1 on thermal properties of the RAF, but also to provide important information on a deeper understanding of the possible nature of the annealing peak, commonly observed in semicrystalline polymers.

7.2 Experimental

7.2.1 Sample preparation

The isotactic polybutene-1 employed in this work is a commercial material PB0110M and its detailed molecular characteristics are given in Table 3.1. The received PB-1 pellets were compressed into films with a thickness of about 0.20 mm under the pressure of 20 bar for 5 min after complete melting at 180 °C. Successively, the compression-molded films were quickly cooled to room temperature with cold water circulating in the hydraulic press plates. Finally, all samples were stored at room temperature for a long time (more than two months), sufficient to ensure completion of the transformation of Form II to I [43, 46], before being subjected to thermal analysis.

7.2.2 DSC analysis

With the aim of analyzing the possible RAF aging for the two different structures, different thermal processes were carried out by DSC (see section 3.2.4). The initial pure Form I sample was heated to 100 °C, which is a temperature high enough to erase RAF thermal history,[29] but low enough to prevent significant melting of the Form I crystals. For Form II, PB-1 sample was heated from 25 to 180 °C and held at this temperature for 5 min to erase previous thermal

history. Subsequently, it was cooled to 90 °C at a rate of 30 °C/min and kept at this temperature for 20 min, to allow Form II isothermal crystallization. As a general rule, the RAF content increases with the crystallization rate,[5] so the selection of this isothermal temperature is made in order to obtain simultaneously pure Form II crystal and a high RAF content.

For the measurements of the enthalpy relaxation after aging, the annealing of the samples was carried out at a given aging temperature (T_a), 0-50 °C for Form II and 10-95 °C for Form I, for 300 and 30 minutes (aging time, t_a), respectively. Afterwards, the samples were cooled to -60 °C at a rate of 30 °C/min and heated to 180 °C at a rate of 10 °C/min for data recording. The experimental reproducibility of the obtained endothermic peaks has been verified for both samples, as shown in the Supporting Information (Appendix D2). The same thermal history, just without the aging step, was also used for the two polymorphic forms for obtaining unaged sample as a reference which ensures that the observed changes are related to the aging process alone. The thermal protocols adopted for the specific crystallization/aging experiments are schematized in Figure 7.1.

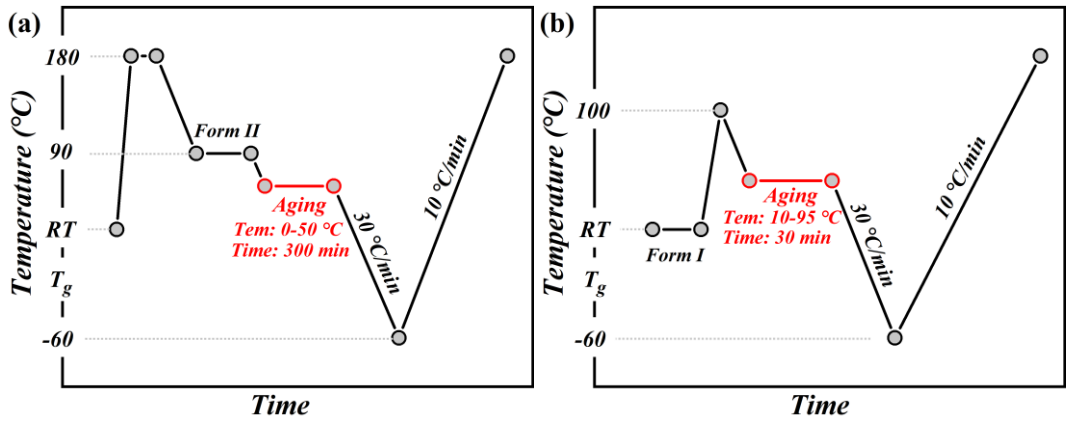

Figure 7.1 Schematic diagrams of the applied thermal history for DSC measurements of samples containing (a) Form II and (b) Form I crystals.

7.3 Results and discussions

7.3.1 Calorimetric response upon aging of PB-1 with only Form I crystals

In order to get an overview on the enthalpy relaxation of the RAF of PB-1, samples with Form I crystals were annealed at various temperatures ranging from 10 to 95 °C for 30 min. Because the DSC heating scans of the aging experiments are extremely similar, a single selected calorimetric result after aging at 40 °C is shown in full scale as an example (Figure 7.2a). The curve evidences the typical calorimetric signature of a semicrystalline PB-1, that is,

the specific heat flow step at about -27 °C, associated with the T_g of MAF, and the melting peak of Form I crystals at around 126 °C. From the literature,[29] we know that RAF coupled to Form I crystals devitrifies with complete mobilization only around 100 °C, i.e., close to the onset of crystal melting. Therefore, the temperature range between the T_g and 100 °C is the most suitable choice for studying the aging of the RAF linked to Form I crystals. Conceptually, the experiment can be schematized as follows. Upon initial heating to 100 °C the RAF is mobilized and ideally reaches the enthalpic state of the equilibrium liquid. By cooling from 100 °C to the aging temperature (T_a) the RAF will vitrify when the temperature falls below its glass transition, giving rise to a non-equilibrium glass. Eventually, upon holding the sample at T_a, the non-equilibrium glass will tend towards the equilibrium liquid state at that temperature, thus undergoing physical aging (see Appendix D1). The results of thermal analysis of annealed samples are reported in Figure 7.2b, where the heating scans at 10 °C/min after annealing at selected temperatures from 40 to 95 °C are shown. With respect to the unaged sample, i.e., the sample heated to 100 °C but not submitted to aging, one small endothermic peak appears in the temperature region between the T_g of the MAF and melting point after aging for 30 min at different temperatures. Such an overshoot shifts to higher temperatures with increasing T_a as noticed in Figure 7.2b and is generally located about 10 °C above T_a. Moreover, despite being very small, the area of the annealing endotherm appears to go through a maximum when aging temperature is varied. Such maximum, at about 60 °C, can be evidenced by curve subtraction after superposition of the annealed and the unaged curves, as it will be discussed further on.

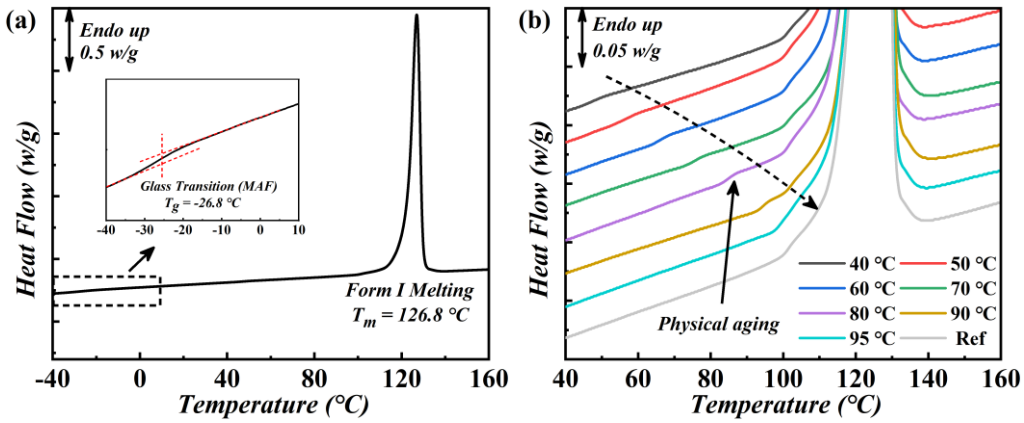

Figure 7.2 (a) Heat flow rate scan at 10 °C/min after aging PB-1 with Form I crystals at 40 °C for 30 min. (b) Enlarged heating scans after aging at the indicated temperatures for PB-1 containing only Form I crystals.

Considering the changes of heat capacity (ΔC_p) at T_g and the values of melting enthalpy

(ΔH_m) of the unaged PB-1 sample with Form I crystals, the content of rigid amorphous fraction can be quantified using the equation $w_{RAF} + w_{MAF} + w_C = 1$. Comparison of ΔC_p at T_g with the heat capacity step of fully amorphous PB-1, taken from the ATHAS Data Bank, provides a mobile amorphous content $w_{MAF} = 0.26$. The crystalline fraction (w_C) was determined by the ratio of melting enthalpy of DSC curve and $\Delta H^0_{m,I}$ (141 J/g) of the ideal crystal of modifications I, that is $w_c = 0.52$. Thus, the content of rigid amorphous phase (w_{RAF}) is about 0.22.

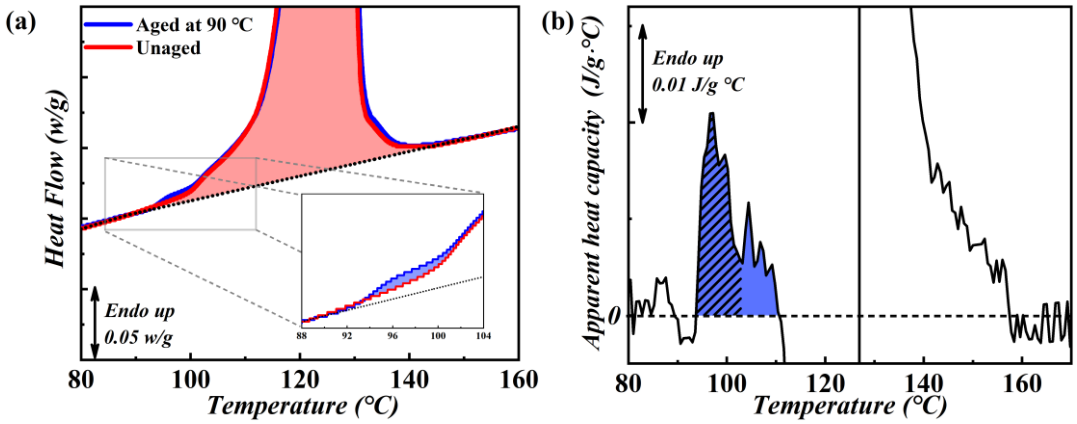

Figure 7.3 (a) Procedure employed to calculate the recovered enthalpy as a showcase for annealing at 90 °C for 30 min, based on the subtraction between the annealed curve and the unaged curve. Blue area: enthalpy difference between both curves. Red area: enthalpy of melting related to the original crystal. (b) Heat capacity difference curve for PB-1 containing only Form I crystals and the hatched area is interpreted as the enthalpy related to the physical aging of the RAF.

In order to clarify the effect of annealing on crystals and both amorphous fractions, the evolution of the three-phase structure of PB-1 as function of annealing is presented in Appendix D3. Panel a of this figure shows that both the specific heat capacity step (ΔC_p) at the glass transition and T_g remain unaltered with respect to those of the unaged sample (within the experimental error), after annealing PB-1 containing Form I crystals at different temperatures for 30 min. This means that, as expected, annealing above T_g has no effect on the MAF, i.e., no additional crystals grew, or if they did their quantity is insufficient to cause a sizable decrease of ΔC_p. From Appendix D3b, it is easy to observe that both melting enthalpy (ΔH_m) and temperature (T_m) do not change after annealing at $T_a \leq 90$ °C, with a minor increase of ΔH_m measurable only at higher aging temperatures and, in any case, smaller than 3%. Combined with the analysis in Appendix D3a, the slight increase of ΔH_m at $T_a > 90$ °C may be attributed to a perfection/re-crystallization phenomena occurring at high annealing temperatures, whereas

re-crystallization does not apparently happen for the annealing experiments below 90 ºC, as typical for PB-1 containing Form I crystals. More discussion will be provided hereinafter.

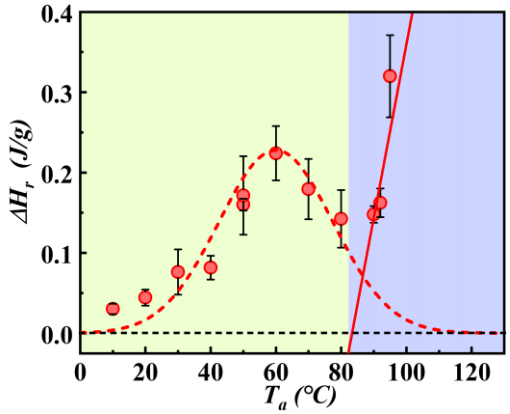

Figure 7.4 Recovered enthalpy as a function of aging temperatures for PB-1 containing only Form I crystals after annealing for 30 min.

In the hypothesis that the small endothermic peak appearing 10 °C above T_a is related to the aging of RAF linked to the Form I crystals, the recovered enthalpy (ΔH_r) was determined as function of the annealing temperature. Details regarding the calculation of recovered enthalpy are reported and discussed in the Figure 7.3. Based on the superposition of the annealed and the unaged curves, a difference curve is obtained by curve subtraction (see Figure 7.3a). The recovered enthalpy associated with the physical aging of the RAF is obtained from the hatched area in Figure 7.3b. The reason for the hatched area not to be equal to the blue area, representing the total excess heat capacity, is because the step-like change in specific heat after the enthalpy relaxation peak (see Figure 7.2) is purposely omitted from the integration. In fact, this observed change is not univocally attributed to a given phenomenon, as the specific heat should come back to the values pertinent to the RAF glass after the enthalpy relaxation. Therefore, this ill-defined phenomenon is not included in the integration, and we only consider the enthalpy relaxation peak unambiguously related to the RAF aging (the hatched area in Figure 7.3b).

The evolution of recovered enthalpy is shown in Figure 7.4 for PB-1 in the presence of Form I crystals after annealing at various temperatures for 30 min. For the higher annealing temperatures ($T_a > 90$ °C), ΔH_r increases with T_a, and is most likely linked to perfection of the original Form I crystals, as shown by combined analysis of Appendix D3b. Instead, at lower annealing temperatures ($T_a < 90$ °C), a typical bell-shaped curve can be observed, which also can be appreciated by the raw heat capacity difference curves shown in Appendix D4. Based

on the above discussion, aging of glasses at temperatures well below the glass transition is marked by the evolution towards an equilibrium state, as shown in Appendix D1. With the decrease of temperature from T_g, the quantity of recoverable enthalpy increases. On the other hand, the time scales for glass aging rapidly increases with decreasing the aging temperature. As such, due to the slower segmental dynamics, for lower temperatures the given aging time is not enough to recover a large amount of enthalpy, despite the larger driving force. Therefore, the bell-shaped curve and the position of the maximum of recovered enthalpy is determined by the balance of these two competing effects. Through the evolution of both ranges of data of recovered enthalpy in Figure 7.4, two interesting results can be found. First, the bell-shaped curve reaches zero recovered enthalpy at around 100-110 °C. Not only a decrease of the enthalpy with the annealing temperature for T_a > 60 °C would not be expected if it was associated to melting of small crystals, which excludes a possible link to fusion, but the temperature where $\Delta H_r = 0$ is about 100 °C, which coincides with the complete mobilization of the RAF coupled to Form I crystals of PB-1, reported in Ref [29]. This supports the hypothesis that the small endotherm at $T = T_a + 10$ °C is linked to aging of the RAF. Moreover, the recovered enthalpy tends to zero at lower temperatures as expected from the curve, due to the exceedingly slow relaxation dynamics. Second, two temperature regions are delimited by the intersection point of the bell-shaped ΔH_r curve and the linear fitting to the high temperature data. The first one can be ascribed to the region where an independent contribution of RAF aging to the recovered enthalpy is expected (green part), and the second one is the region where the excess heat endotherm is contributed by both RAF aging and crystal perfection (blue part). Specifically, the endothermic peaks in PB-1 may originate from the enthalpy relaxation of the RAF linked to the original Form I crystals when the annealing temperature is below about 85 °C. With the increase of temperature, crystal perfection starts appearing; in this case the endotherm originates from two different processes. In fact, the non-monotonic trend of ΔH_r with aging temperature clearly points towards the superposition of different competing effects, namely, enthalpy relaxation of the RAF and crystal perfectioning.

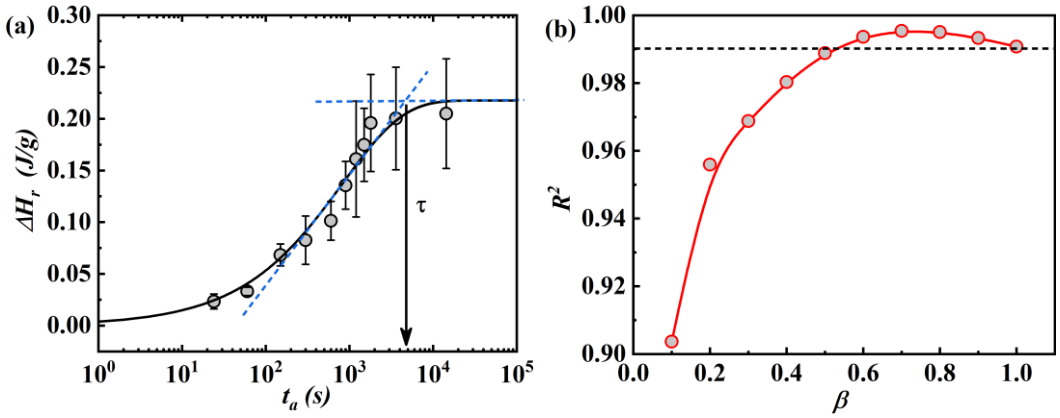

Figure 7.5 (a) Evolution of the recovered enthalpy of Form I RAF with time after annealing at 60 °C. Vertical arrow indicates the values of τ, the timescale to reach a plateau in the recovered enthalpy. (b) Evolution of the coefficient of determination (R^2) with the stretching exponent (β) from the KWW fitting. The dashed line represents a correlation coefficient of 0.99.

In order to substantiate this hypothesis, the kinetics of RAF aging was traced by varying the annealing time at a constant temperature of 60 °C. Figure 7.5a shows the time evolution of the recovered enthalpy after annealing for the original films containing Form I crystals. Data shows nonexponential and nonlinear behavior, as typical of aging (relaxation) processes.[53] A common way to describe this phenomenology, which for simplicity incorporates the nonlinear behavior into the nonexponential one, relies on the empirical Kohlrausch-Williams-Watts (KWW) equation.[54, 55] This equation, having the analytical expression of equation (7.1), contains two adjustable parameters, τ and β, which are, respectively, a characteristic relaxation time and a dimensionless parameter often known as the stretching exponent.

$$\Delta H(t) = \Delta H_{tot}\left(1 - e^{\left(-\frac{t}{\tau}\right)^{\beta}}\right) \tag{7.1}$$

ΔH_{tot} is the total amount of recoverable enthalpy. The data of Figure 7.5a were used to determine KWW parameters, with details of the fitting presented in Figure 7.5b. The coefficient of determination (R^2) with the stretching exponent β in the range 0.5-1 reveals a value of 0.99, probing excellent fitting of experimental data with the KWW function, which supports the hypothesis that the small endotherm measured just above T_a is linked to relaxation of amorphous parts. As it can be observed, the time scale to reach the plateau of the RAF physical aging, τ (black arrow), is about 4500 s for segments directly linked to the Form I crystalline stems annealing at 60 °C. It is worth noting that β is commonly smaller than unity for the fitting of relaxation data in the glassy state.[42, 55] In Figure 7.5a an exponent of β = 0.6 is obtained, which also suggests that aging of RAF of PB-1 in the presence of Form I crystals actually

follows a glassy dynamics behavior, because of the excellent KWW fitting ($R^2 > 0.99$) when $\beta < 1$. Additional support of this hypothesis is provided by analysis of annealing of PB-1 containing Form II condis crystals, presented here below.

7.3.2 Calorimetric response upon aging of PB-1 with Form II crystals

The DSC plots of PB-1 containing Form II crystals, annealed at various temperatures, are compared in Figure 7.6 with that of unaged polymer. As shown in Figure 7.6a, all heating curves display two major endotherms, the one centered at 116 °C is due to melting of Form II crystal, and the smaller endotherm at higher temperatures is due to melting of Form I crystals, attained upon spontaneous transformation of the original Form II modification that occurs simultaneously with annealing.[42, 55] An overview of the enlarged calorimetric responses of original PB-1 containing Form II crystals upon annealing is shown in Figure 7.6b, where the heating scans after aging at different temperatures for 300 min are shown. A small endothermic peak can be observed after annealing between T_g and T_m with respect to the unaged scan, although this is much broader than the one attained after annealing of samples with Form I crystals (Figure 7.2b). For this reason, it is less visible and more difficult to integrate if an aging time of 30 minutes is chosen. Therefore, a longer aging time of 300 minutes was selected. The endotherm shifts to higher temperature with increasing T_a, as indicated by the dashed line in Figure 7.6b. This endothermic peak becomes gradually weaker with increasing aging temperature, until it disappears at around 50 °C, as also seen upon aging of Form I PB-1 at $T_a < 100$ °C. Indeed, for both crystal modifications, a decrease of the endotherm with T_a excludes a possible link to mere melting of small crystals developed at T_a, but rather it conforms to an endothermic overshoot resulting from physical aging and its dependence on the aging temperature, as it vanishes well below T_m.[56-58]

The applied thermal protocol also results in an expected partial transformation of Form II to Form I crystals, as revealed by the melting peak of Form I, visible also in the unaged curve in Figure 7.6a. Therefore, it is not possible to observe the aging of RAF combined with a pure Form II during annealing. The amount of Form I fractions of PB-1 developed upon annealing temperatures is quantified in Figure 7.7. The content of Form I reaches a maximum of about 20% of the total crystallinity (meaning an absolute content of about 10-12%) at $T_a = 10$ °C, in agreement with literature data.[59, 60] At higher annealing temperature, lower amounts of Form I crystals develop. Unaged sample has an initial content of Form I of only 4 % resulting from the non-isothermal steps. It is therefore possible that Form I influences the further analysis of enthalpy relaxation of Form II RAF, due to the simultaneous existence of both polymorphs

in the same sample, albeit with largely different contents. However, we can judge such influence referring to Form I experiments at low aging temperatures (10-30 °C, i.e., aging temperatures relevant for Form II samples), from which it is deduced that the RAF coupled with Form I does not to contribute substantially to further aging, due to its exceedingly long structural relaxation time scales at these temperatures (see Figure 7.4). Therefore, the recovered enthalpy of the RAF discussed below is related for the large majority to the enthalpic overshoot few degrees above T_a of Form II, considering the low content and low expected recovered enthalpy of Form I at low T_a.

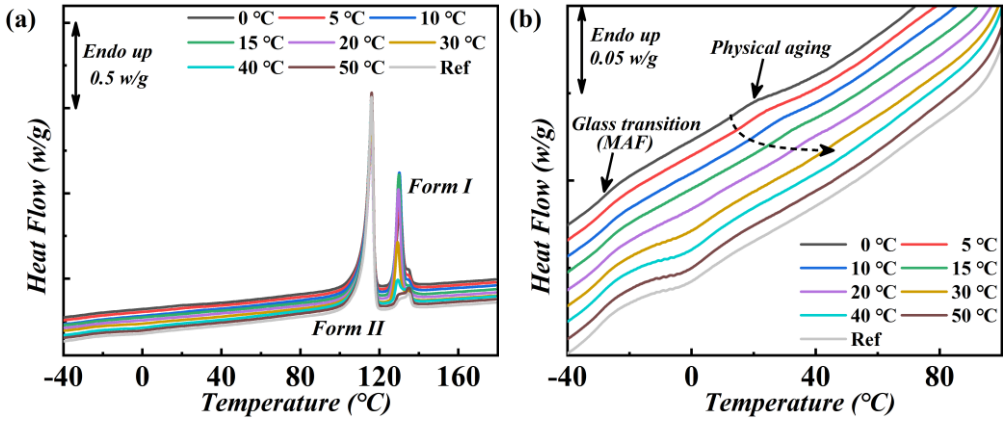

Figure 7.6 (a) Heat flow rate scans at 10 °C/min after aging PB-1 containing Form II crystals at different temperatures for 300 min. (b) Enlarged heating scans after aging at the indicated temperatures.

An additional thermal event, centered around 0 °C, is also observed in some plots of Figure 7.6b, and it is linked to the solid-solid Form II to Form I transformation.[60] Being very close to T_g of the MAF, it complicates quantitative analysis of the C_p increment at the glass transition as a function of the aging temperature, but does not hinder analysis of the influence of the annealing process on melting of the crystalline phase.

Figure 7.8 shows the variation of ΔH_m of Form II, Form I and total crystals with annealing temperature for original sample with Form II crystals. The overall melting enthalpy goes through a maximum around 10 °C, which is to be linked to the higher melting enthalpy of Form I, which reaches its maximum value after annealing at the same temperature. However, the total crystallinity of the sample is practically constant with respect to that of unaged PB-1 upon aging at different temperatures, as shown in Appendix D5, which confirms that the Form II to Form I transformation occurs without variation of overall crystallinity, in agreement with literature data.[61] Integration of the melting endotherms and comparison with the heat of

fusion of the ideal crystals of Form I (141 J/g) and Form II (62 J/g), respectively, provide a crystal fraction of $w_C = 0.60$ for unaged sample. The heat capacity step at T_g of the unaged PB-1 with Form II crystals is used to estimate a mobile amorphous fraction equal to 0.23. Therefore, a rigid amorphous fraction which amounts to $w_{RAF} = 0.17$ is obtained.

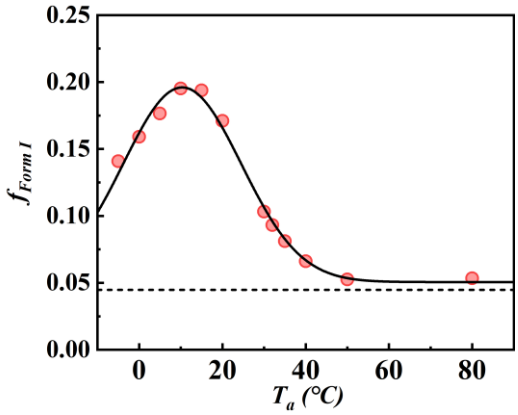

Figure 7.7 Evolution of Form I fraction of PB-1 after annealing at different temperatures for 300 min, followed by cooling to -60 °C at 30 °C/min and heating to 180 °C at 10 °C/min, where the black dashed line represents the Form I content of unaged sample.

The evolution of recovered enthalpy values as a function of aging temperatures, for samples with Form II crystals, is presented in Figure 7.9. At low temperatures, ΔH_r increases with T_a, to reach a maximum at 10 °C, then the calculated recovered enthalpy gradually reduces until it disappears at 40-50 °C. The DSC scans of the unaged sample and samples annealed at $T_a > 40$ °C perfectly overlap above T_a, as can be observed by the data shown in Figure 7.6b. Annealing at these temperatures might lead to additional crystal growth/perfection, as crystallization of Form II is known to be fastest at 40-50 °C.[62, 63] Actually, no annealing endotherm around $T_a + 10$ °C can be detected in the DSC plots of Figure 7.6 after prolonged permanence at 40 and 50 °C, which excludes contributions from crystal growth/perfection to ΔH_r. This result suggests that the observed endothermic peak in the temperature range below 40 °C is not dominated by crystallization effects, but rather results from the enthalpy relaxation of the amorphous regions constrained at the boundary with Form II crystals. Additional support to this hypothesis is provided by a specific thermal protocol including a multistep aging experiment with results presented and discussed in the Supporting Information (Appendix D6). These data confirm that the nature of the excess endotherms is enthalpy relaxation of Form II RAF.

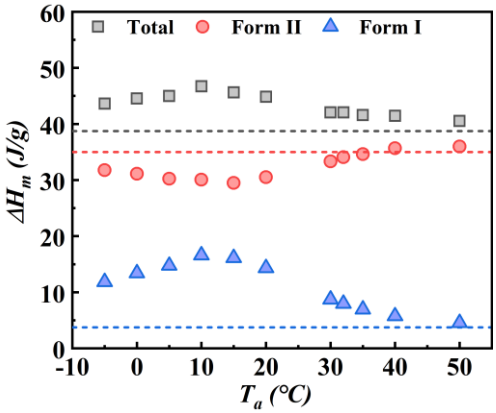

Figure 7.8 Variation of crystals' melting enthalpy (ΔH_m) with annealing temperature. The dashed lines of various colors represent the corresponding properties of the unaged sample.

The data of Figure 7.9 can be exploited to perform a more quantitative analysis of the aging behavior of the RAF linked with Form II crystals. T_g of the RAF constrained at the boundary with Form II crystals, based on the onset of aging effects (complete mobilization of RAF) is defined as the temperature where the recovered enthalpy reaches zero in Figure 7.9. The calculated value of $T_g \approx 50$ °C for the Form II RAF crystals coincides the value reported in Ref [28].

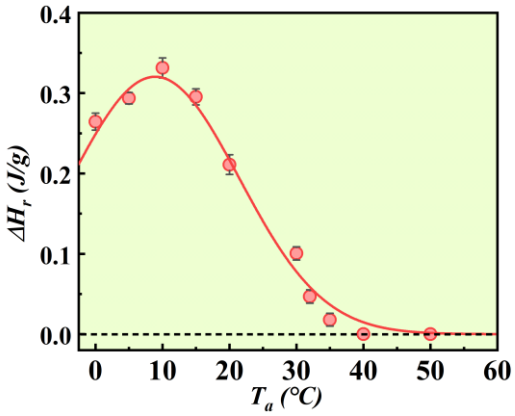

Figure 7.9 Evolution of recovered enthalpy as a function of aging temperatures for original PB-1 in the presence of Form II crystals after annealing for 300 min.

To provide further insight into the aging process of RAF coupled to Form II crystals, the influence of aging time (t_a) at 10 °C was determined, with results detailed in Figure 7.10. Heat flow rate plots after selected aging times at 10 °C are shown in Figure 7.10a. A change in the area of the endotherm with increasing aging time is evident, by comparison to the unaged sample. The recovered enthalpy of RAF was quantified taking into account that the

transformation from Form II to Form I always takes place during aging and continues with time, with results presented in Figure 7.10b. Two different kinetics processes connected with RAF mobilization can be clearly identified, with the fraction of Form I at the corresponding demarcation point equals to a fraction of about 0.2. Obviously, the lower the content of transformed Form I, the more reasonable the analysis of the aging process of RAF coupled to Form II crystals is. By fitting the evolution of the recovered enthalpy with time when the fraction of Form I is below 0.2 using the KWW law (red line), a stretching exponent $\beta = 0.64$ is obtained, which is typical of glassy dynamics, as also detailed above for RAF coupled with Form I. Therefore, the analysis of the evolution of enthalpy recovery of Form II RAF after annealing at various temperatures is reliable due to the low transformed Form I fraction (see Figure 7.7). However, with annealing for longer times, no plateau of recovered enthalpy of RAF coupled with Form II can be observed, different from the case of the RAF coupled with Form I (shown in Figure 7.5a). Instead, in this case the mobilization kinetics of the RAF linked to the Form II crystals with time becomes faster when the fraction of Form I is above 0.2.

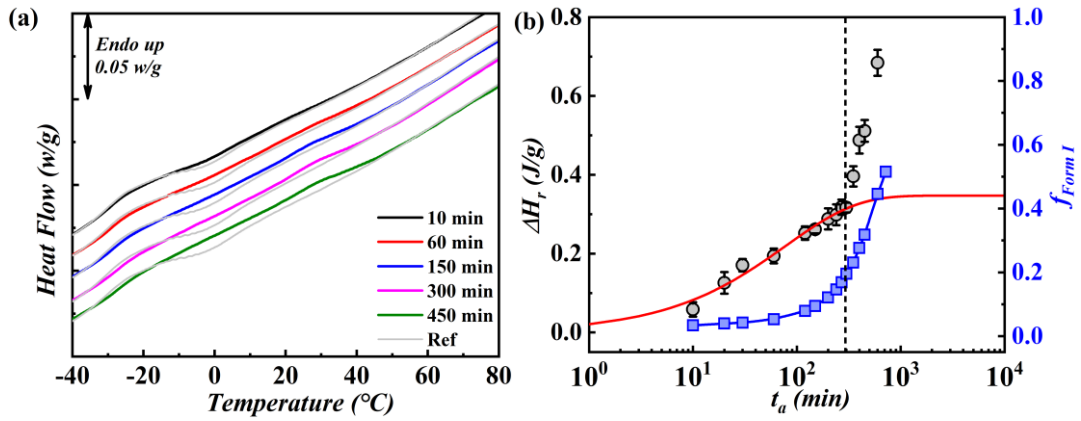

Figure 7.10 (a) Enlarged heat flow rate scans at 10 °C/min after aging at 10 °C for the indicated times for PB-1 containing Form II crystals, compared to the unaged polymer (Ref curve). (b) Evolution of the recovered enthalpy of Form II RAF and the fraction of transformed Form I with annealing time after annealing at 10 °C. Two different aging kinetics were distinguished by the vertical black dashed line.

To understand the reasons behind this trend, we can consider how the crystalline phases are expected to affect the mobility of the coupled amorphous parts, particularly in the process of transformation from Form II to Form I.

The long-range order of the helical conformation of Form I modification strongly hinders chain motions in the crystals and causes tight constraints within the coupled amorphous phase.

Conversely, the conformational disorder of Form II helices allows large movement of the chain backbone, which gives rise to a decreased stress imparted to the amorphous parts linked with the crystals. Indeed, such chain dynamics within PB-1 crystals dependent on the crystalline modification has been studied by nuclear magnetic resonance.[47, 64-66] Therefore, the amorphous segments of the rigid amorphous fraction of Form II crystals are much easier to mobilize compared with the sample with Form I crystals.

During the process of transformation from Form II to Form I the decrease of specific volume of the crystal phase may cause an increase of the local stress at the interface of crystal and amorphous fractions, which results in a higher amount of RAF with an additionally reduced mobility.[29]

The dependence of the aging of the RAF coupled to Form II on the transformed Form I fraction can be justified by considering the concomitant solid-solid transformation. When the Form I fraction is below 0.2, the aging involves RAF coupled with the original Form II crystals, while when Form I modification content is above this point, RAF linked to Form I crystals could start to dominate the enthalpy relaxation. Transformation of Form II to Form I, which starts most likely at the side surfaces of the crystals,[67] strengthens the constraints on the adjacent amorphous region, but also increases the RAF content due to additional stress caused by volume shrinkage, with the result that the measured recovered enthalpy is found to increase more rapidly.

7.4 Conclusion

The present work focuses on identifying the glass transition of the RAF of PB-1 containing Form II or Form I crystals. The advantage of using a polymorphic system is found in the fact that the two crystals have largely different RAF mobilization (glass transition) temperatures, as extensively documented in the literature, enabling to study separately the RAF aging behavior for the two structures. For both structures, a small endothermic peak is observed when the sample is aged at temperatures between the glass transition and the melting temperature. For the RAF linked to Form I crystals, enthalpy relaxation is clearly identified for annealing below 90 °C, and complete devitrification of RAF occurs at 100-110 °C, as estimated through the trend of isochronous recovered enthalpy as a function of aging temperature. For the aging experiment of RAF coupled with Form II crystals, the vitrification temperature of the RAF was estimated as 40-50 °C using the same method. Both temperatures match well with the values obtained independently by modulated calorimetry in the previous literature. Thus,

by the strategy of using a polymorphic sample with different RAF mobility, depending on the crystalline structure, this research provides convincing evidence that the nature of endothermic peak in aged polybutene-1 is related to structural recovery of the RAF. Incidentally, the concomitant transformation of Form II to Form I during annealing influences the RAF glassy dynamics due to variation in the conformational structure of the chain and in the content of rigid amorphous fraction.

References

[1] H. Suzuki, J. Grebowicz, B. Wunderlich, Glass-Transition of Poly(Oxymethylene), British polymer journal 17(1) (1985) 1-3.

[2] B. Wunderlich, Reversible crystallization and the rigid–amorphous phase in semicrystalline macromolecules, Progress in polymer science 28(3) (2003) 383-450.

[3] B. Wunderlich, A classification of molecules, phases, and transitions as recognized by thermal analysis, Thermochimica Acta 340 (1999) 37-52.

[4] B. Wunderlich, Thermal analysis of polymeric materials, Springer 2005.

[5] M.L. Di Lorenzo, M.C. Righetti, Crystallization-induced formation of rigid amorphous fraction, Polymer Crystallization 1(2) (2018) e10023.

[6] Q. Zia, D. Mileva, R. Androsch, Rigid amorphous fraction in isotactic polypropylene, Macromolecules 41(21) (2008) 8095-8102.

[7] P.A. Klonos, L. Papadopoulos, M. Kasimatis, H. Iatrou, A. Kyritsis, D.N. Bikiaris, Synthesis, Crystallization, Structure Memory Effects, and Molecular Dynamics of Biobased and Renewable Poly (n-alkylene succinate) s with n from 2 to 10, Macromolecules 54(3) (2021) 1106-1119.

[8] G. Papamokos, T. Dimitriadis, D.N. Bikiaris, G.Z. Papageorgiou, G. Floudas, Chain conformation, molecular dynamics, and thermal properties of poly (n-methylene 2, 5-furanoates) as a function of methylene unit sequence length, Macromolecules 52(17) (2019) 6533-6546.

[9] P. Huo, P. Cebe, Dielectric relaxation of poly (phenylene sulfide) containing a fraction of rigid amorphous phase, Journal of Polymer Science Part B: Polymer Physics 30(3) (1992) 239-250.

[10] A. Wurm, M. Merzlyakov, C. Schick, Isothermal crystallisation of PCL studied by temperature modulated dynamic mechanical and TMDSC analysis, Journal of Thermal Analysis and Calorimetry 56(3) (1999) 1155-1161.

[11] C. Schick, M. Merzlyakov, A. Minakov, A. Wurm, Crystallization of polymers studied by temperature modulated calorimetric measurements at different frequencies, Journal of Thermal Analysis and Calorimetry 59(1-2) (2000) 279-288.

[12] C. Schick, A. Wurm, A. Mohamed, Vitrification and devitrification of the rigid amorphous fraction of semicrystalline polymers revealed from frequency-dependent heat capacity, Colloid and Polymer Science 279(8) (2001) 800-806.

[13] C. Schick, A. Wurm, A. Mohamed, Dynamics of reversible melting revealed from frequency dependent heat capacity, Thermochimica Acta 392 (2002) 303-313.

[14] C. Schick, A. Wurm, A. Mohammed, Formation and disappearance of the rigid amorphous fraction in semicrystalline polymers revealed from frequency dependent heat capacity, Thermochimica Acta 396(1-2) (2003) 119-132.

[15] R. Androsch, B. Wunderlich, The link between rigid amorphous fraction and crystal perfection in cold-crystallized poly (ethylene terephthalate), Polymer 46(26) (2005) 12556-12566.

[16] Q. Ma, G. Georgiev, P. Cebe, Constraints in semicrystalline polymers: using quasi-isothermal analysis to investigate the mechanisms of formation and loss of the rigid amorphous fraction, Polymer 52(20) (2011) 4562-4570.

[17] M.L. Di Lorenzo, M. Cocca, M. Malinconico, Crystal polymorphism of poly (l-lactic acid) and its influence on thermal properties, Thermochimica Acta 522(1-2) (2011) 110-117.

[18] E. Zhuravlev, J.W. Schmelzer, B. Wunderlich, C. Schick, Kinetics of nucleation and crystallization in poly (ε-caprolactone)(PCL), Polymer 52(9) (2011) 1983-1997.

[19] M.L. Di Lorenzo, M. Gazzano, M.C. Righetti, The role of the rigid amorphous fraction on cold crystallization of poly (3-hydroxybutyrate), Macromolecules 45(14) (2012) 5684-5691.

[20] I. Kolesov, R. Androsch, The rigid amorphous fraction of cold-crystallized polyamide 6, Polymer 53(21) (2012) 4770-4777.

[21] M.L. Di Lorenzo, M.C. Righetti, Effect of thermal history on the evolution of crystal and amorphous fractions of poly [(R)-3-hydroxybutyrate] upon storage at ambient temperature, European Polymer Journal 49(2) (2013) 510-517.

[22] M.C. Righetti, E. Tombari, M.L. Di Lorenzo, The role of the crystallization temperature on the nanophase structure evolution of poly [(R)-3-hydroxybutyrate], Journal of Physical Chemistry B 117(40) (2013) 12303-12311.

[23] I. Kolesov, D. Mileva, R. Androsch, Mechanical behavior and optical transparency of polyamide 6 of different morphology formed by variation of the pathway of crystallization, Polymer Bulletin 71(3) (2014) 581-593.

[24] M.C. Righetti, M. Laus, M.L. Di Lorenzo, Temperature dependence of the rigid amorphous fraction in poly (ethylene terephthalate), European Polymer Journal 58 (2014) 60-68.

[25] M.C. Righetti, D. Prevosto, E. Tombari, Time and temperature evolution of the rigid amorphous fraction and differently constrained amorphous fractions in PLLA, Macromolecular Chemistry and Physics 217(18) (2016) 2013-2026.

[26] M.C. Righetti, M. Gazzano, N. Delpouve, A. Saiter, Contribution of the rigid amorphous fraction to physical ageing of semi-crystalline PLLA, Polymer 125 (2017) 241-253.

[27] E. Parodi, L. Govaert, G. Peters, Glass transition temperature versus structure of polyamide 6: A flash-DSC study, Thermochimica Acta 657 (2017) 110-122.

[28] M.L. Di Lorenzo, M.C. Righetti, The three-phase structure of isotactic poly (1-butene), Polymer 49(5) (2008) 1323-1331.

[29] M.L. Di Lorenzo, M.C. Righetti, B. Wunderlich, Influence of crystal polymorphism on the three-phase structure and on the thermal properties of isotactic poly (1-butene), Macromolecules 42(23) (2009) 9312-9320.

[30] J. Pak, M. Pyda, B. Wunderlich, Rigid amorphous fractions and glass transitions in poly (oxy-2, 6-dimethyl-1, 4-phenylene), Macromolecules 36(2) (2003) 495-499.

[31] S.X. Lu, P. Cebe, Effects of annealing on the disappearance and creation of constrained amorphous phase, Polymer 37(21) (1996) 4857-4863.

[32] M.L. Di Lorenzo, M.C. Righetti, M. Cocca, B. Wunderlich, Coupling between crystal melting and rigid amorphous fraction mobilization in poly (ethylene terephthalate), Macromolecules 43(18) (2010) 7689-7694.

[33] M.C. Righetti, M.L. Di Lorenzo, E. Tombari, M. Angiuli, The low-temperature endotherm in poly (ethylene terephthalate): Partial melting and rigid amorphous fraction mobilization, The Journal of Physical Chemistry B 112(14) (2008) 4233-4241.

[34] H. Chen, P. Cebe, Investigation of the rigid amorphous fraction in Nylon-6, Journal of Thermal Analysis and Calorimetry 89(2) (2007) 417-425.

[35] S. Sohn, A. Alizadeh, H. Marand, On the multiple melting behavior of bisphenol-A polycarbonate, Polymer 41(25) (2000) 8879-8886.

[36] Z.-G. Wang, B. Hsiao, B. Sauer, W. Kampert, The nature of secondary crystallization in poly (ethylene terephthalate), Polymer 40(16) (1999) 4615-4627.

[37] Y. Kong, J. Hay, Multiple melting behaviour of poly (ethylene terephthalate), Polymer 44(3) (2003) 623-633.

[38] C. Schick, R. Androsch, The Origin of Annealing Peaks in Semicrystalline Polymers:

Enthalpy Recovery or Melting?, Macromolecules 53(20) (2020) 8751-8756.
[39] H. Xu, P. Cebe, Heat capacity study of isotactic polystyrene: dual reversible crystal melting and relaxation of rigid amorphous fraction, Macromolecules 37(8) (2004) 2797-2806.
[40] M. Song, Rigid amorphous phase and low temperature melting endotherm of poly (ethylene terephthalate) studied by modulated differential scanning calorimetry, Journal of Applied Polymer Science 81(11) (2001) 2779-2785.
[41] J. Martín, N. Stingelin, D. Cangialosi, Direct calorimetric observation of the rigid amorphous fraction in a semiconducting polymer, Journal of physical chemistry letters 9(5) (2018) 990-995.
[42] X. Monnier, D. Cavallo, M.C. Righetti, M.L. Di Lorenzo, S. Marina, J. Martin, D. Cangialosi, Physical aging and glass transition of the rigid amorphous fraction in poly (L-lactic acid), Macromolecules 53(20) (2020) 8741-8750.
[43] L.C.E. Struik, Physical aging in amorphous polymers and other materials, Elsevier, NewYork (1978).
[44] L.C.E. Struik, The mechanical and physical ageing of semicrystalline polymers: 1, Polymer 28(9) (1987) 1521-1533.
[45] L.C.E. Struik, The mechanical behaviour and physical ageing of semicrystalline polymers: 2, Polymer 28(9) (1987) 1534-1542.
[46] M. Cocca, R. Androsch, M.C. Righetti, M. Malinconico, M.L. Di Lorenzo, Conformationally disordered crystals and their influence on material properties: the cases of isotactic polypropylene, isotactic poly (1-butene), and poly (l-lactic acid), Journal of Molecular Structure 1078 (2014) 114-132.
[47] D. Maring, M. Wilhelm, H.W. Spiess, B. Meurer, G. Weill, Dynamics in the crystalline polymorphic forms I and II and form III of isotactic poly-1-butene, Journal of Polymer Science Part B: Polymer Physics 38(20) (2000) 2611-2624.
[48] L. Liu, Z. Chu, Y. Liao, Z. Ma, Y. Li, Flow-Induced Crystallization in Butene-1/1, 5-Hexadiene Copolymers: Mutual Effects of Molecular Factor and Flow Stimuli, Macromolecules 53(19) (2020) 8476-8486.
[49] A.T. Jones, Cocrystallization in copolymers of α-olefins II—Butene-1 copolymers and polybutene type II/I crystal phase transition, Polymer 7(1) (1966) 23-59.
[50] Y. Wang, Z. Jiang, Z. Wu, Y. Men, Tensile deformation of polybutene-1 with stable form I at elevated temperature, Macromolecules 46(2) (2013) 518-522.
[51] Y. Liao, L. Liu, Z. Ma, Y. Li, Influence of steric norbornene co-units on the crystallization and memory effect of polybutene-1 copolymers, Macromolecules 53(6) (2020) 2088-2100.

[52] W. Wang, C. Shao, L. Zheng, B. Wang, L. Pan, G. Ma, Y. Li, Y. Wang, C. Liu, Z. Ma, Stretching-induced phase transition of the butene-1/ethylene random copolymer: Orientation and kinetics, Journal of Polymer Science Part B: Polymer Physics 57(2) (2019) 116-126.

[53] D. Cangialosi, V.M. Boucher, A. Alegría, J. Colmenero, Physical aging in polymers and polymer nanocomposites: recent results and open questions, Soft Matter 9(36) (2013) 8619-8630.

[54] G. Williams, D.C. Watts, Non-symmetrical dielectric relaxation behaviour arising from a simple empirical decay function, Transactions of the Faraday society 66 (1970) 80-85.

[55] D. Cangialosi, Dynamics and thermodynamics of polymer glasses, Journal of Physics: Condensed Matter 26(15) (2014) 153101.

[56] A.R. Berens, I. Hodge, Effects of annealing and prior history on enthalpy relaxation in glassy polymers. 1. Experimental study on poly (vinyl chloride), Macromolecules 15(3) (1982) 756-761.

[57] N.G. Perez-de-Eulate, M. Sferrazza, D. Cangialosi, S. Napolitano, Irreversible Adsorption Erases the Free Surface Effect on the T g of Supported Films of Poly (4-tert-butylstyrene), ACS Macro Letters 6(4) (2017) 354-358.

[58] V.M. Boucher, D. Cangialosi, A. Alegría, J. Colmenero, Reaching the ideal glass transition by aging polymer films, Physical Chemistry Chemical Physics 19(2) (2017) 961-965.

[59] Y. Qiao, Q. Wang, Y. Men, Kinetics of nucleation and growth of form II to I polymorphic transition in polybutene-1 as revealed by stepwise annealing, Macromolecules 49(14) (2016) 5126-5136.

[60] M.L. Di Lorenzo, R. Androsch, M.C. Righetti, The irreversible Form II to Form I transformation in random butene-1/ethylene copolymers, European Polymer Journal 67 (2015) 264-273.

[61] Y. Wang, Z. Jiang, L. Fu, Y. Lu, Y. Men, Stretching temperature dependency of lamellar thickness in stress-induced localized melting and recrystallized polybutene-1, Macromolecules 46(19) (2013) 7874-7879.

[62] I. Stolte, R. Androsch, M.L. Di Lorenzo, C. Schick, Effect of aging the glass of isotactic polybutene-1 on form II nucleation and cold crystallization, The Journal of Physical Chemistry B 117(48) (2013) 15196-15203.

[63] P. Liu, Y. Xue, Y. Men, Formation and stabilization of crystal nuclei in isotactic polybutene-1 aged below glass transition temperature, Polymer 192 (2020) 122293.

[64] H.W. Beckham, K. Schmidt-Rohr, H.W. Spiess, Conformational disorder and its dynamics within the crystalline phase of the form ii polymorph of isotactic poly (1-butene), ACS. Symp.

Ser 598 (1995) 242-253.
[65] T. Miyoshi, S. Hayashi, F. Imashiro, A. Kaito, Side-chain conformation and dynamics for the form II polymorph of isotactic poly (1-butene) investigated by high-resolution solid-state 13C NMR spectroscopy, Macromolecules 35(15) (2002) 6060-6063.
[66] D. Maring, B. Meurer, G. Weill, 1H NMR studies of molecular relaxations of poly-1-butene, Journal of Polymer Science Part B: Polymer Physics 33(8) (1995) 1235-1247.
[67] R. Xin, Z. Guo, Y. Li, X. Sun, M. Xue, J. Zhang, S. Yan, Morphological evidence for the two-step II–I phase transition of isotactic polybutene-1, Macromolecules 52(19) (2019) 7175-7182.

Chapter 8. General conclusions and perspectives

8.1 Conclusions

This thesis is devoted to gain a deeper understanding on particular crystallization phenomena of the polymorphic polybutene-1. Several aspects were tackled, including heterogeneous nucleation (both on Form I crystal seeds and on various solid substrates) and the rigid amorphous fraction.

The topic of cross-nucleation between Form II and Form I was studied in Chapters 4 and 5. Using Form I seeds possessing a different morphology as substrates, we could unveil that the cross-nucleation ability toward Form II dependent on the type of substrate (spherulitic, hedritic, fiber-like). The observed different efficiencies of the seeds are tentatively attributed to differences in the Form I lamellar thickness, on the basis of the hypothesized epitaxy and heterogeneous nucleation mechanism. The cross-nucleation energy barrier obtained from the quantitative analysis of the induction time could be reasonably described with classical models. The results confirmed that the rate determining step in the attainment of the nucleus critical size is the addition of several crystalline layers, rather than the formation of the first crystalline layer on the substrate. The cross-nucleation behavior of Form II on the surface of Form I in PB-1 was further investigated by nano-focused synchrotron X-ray diffraction. We obtained a preferred mutual orientation of the two polymorphs, with the $(200)_{II}$ plane aligned ~8.5º apart from the $(110)_{I}$ plane, meaning a parallel (110) plane between two modifications during cross-nucleation. In view of the degree of lattice mismatch along various directions (about 3.9% between the inter-chain distances and 9.7% along the chain axes), we proposed that cross-nucleation of Form II on Form I occurs at the (110) contact planes through epitaxial nucleation.

In Chapter 6, the nucleation process of PB-1 on the surface of various fibers was investigated. Direct observation via polarized optical microscopy revealed two morphologies, a transcrystalline layer (TCL) induced by PB-1 Form I fiber and hybrid shish–calabash structure (HSC) induced by other fibers, namely carbon, glass, PP, PLLA homocrystal and stereocomplex. The effect of fiber characteristics, including roughness, surface chemistry and specific interactions (epitaxy), on heterogeneous nucleation kinetics were considered. Moreover, the observed different crystalline morphologies on the various fibers are proposed to be linked to the number of potential nucleation sites on the rough surface. In particular, it is shown for the first time that, regardless of the height of the free energy barrier, the presence of

a high density of nucleation sites along the fiber is mandatory to obtain a transcrystalline morphology.

Besides investigating the heterogeneous nucleation behavior of PB-1, in Chapter 7 we focused on the understanding of the effect of different crystalline modification on the relaxation behavior of the rigid amorphous fraction. A small endothermic peak representing the structural recovery of RAF glass was observed when the sample was aged at temperatures between the glass transition and the melting temperature. Through analyzing the trends of isochronous recovered enthalpy as a function of aging temperature, the vitrification temperature of RAF was estimated as 100-110 °C and 40-50 °C, for samples with Form I and Form II crystals, respectively. By using a multiple approach (glassy dynamics model, crystallization kinetics and a multistep aging experiment), compelling evidences are provided that the nature of endothermic peak in aged PB-1 is related to structural recovery of the RAF. Moreover, the concomitant transformation of Form II to Form I during annealing influences the RAF glassy dynamics due to variation in the conformational structure of the chain and in the content of rigid amorphous fraction.

8.2 Perspectives

In this work, we have addressed the mechanism of epitaxy for cross-nucleation of Form II on Form I in polybutene-1, however, we have not commented on the possibility of epitaxial crystallization in this process for other polymorphic polymers. Therefore, the investigation of the cross-nucleation behavior of different polymers by the method of nano-focused synchrotron X-ray diffraction could be of interest. We expect epitaxy to be a general mechanism of cross-nucleation process appearing in different polymers, although nucleation via “simple” heterogeneous nucleation is also possible.

Our approach for the crystallization in PB-1/fiber composites has a great potential in fundamental research, especially since commercial fibers were used, which may be attractive for various applications. However, the systematic research by varying roughness and chemical structure of the polymeric fibers is still incomplete. Therefore, the study of crystallization in polymer/fiber composites through the production of a regular fiber surface roughness or tuning chemical composition can be proposed as a follow-up of the present research. The type of polymeric matrix can also be changed, to examine the different crystallization behavior and mechanical response.

For the study of RAF aging, we have studied the effect of polymorphism on the relaxation

behavior of the rigid amorphous fraction of a PB-1 homopolymer. In future work copolymers of polybutene-1 with different types and contents of monomer can be selected. Eventually, diagram including the comonomer content and glass transition temperature of RAF will be established to provide the necessary reference for the three-phase structure of polybutene-1.

Appendix

Appendix A

The following is the supplementary data to Chapter 4

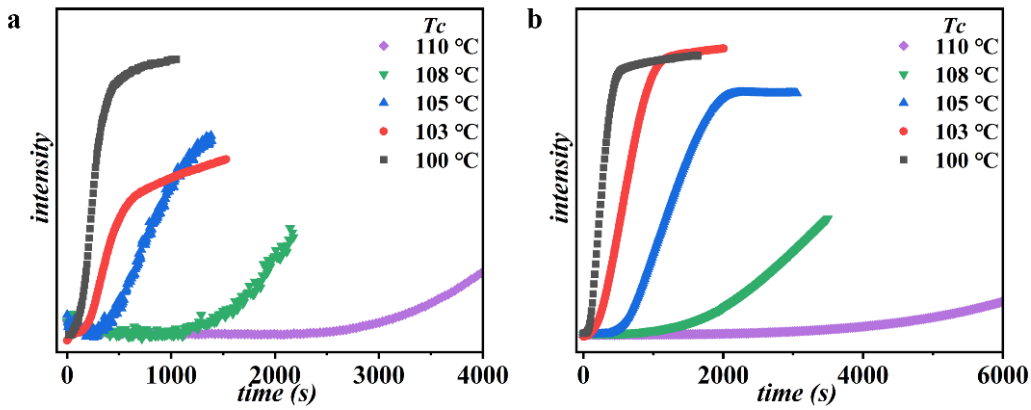

Figure A1 Evolution of light intensity as a function of crystallization time during isothermal crystallization at different temperatures for (a) spherulitic and (b) hedritic Form I substrate.

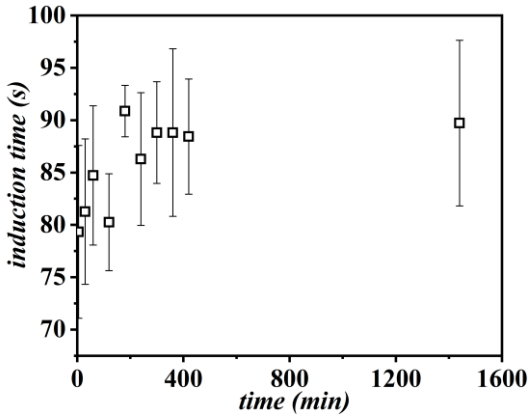

Figure A2 Measured induction time during crystallization at 105 °C after different annealing times at 124 °C subsequently to Form I fiber insertion.

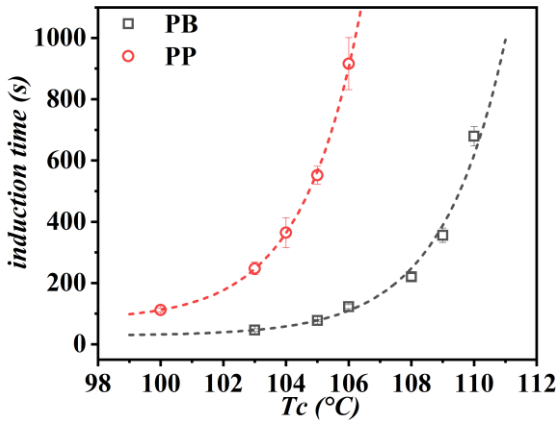

Figure A3 Induction time as a function of TC for Form II PB-1 nucleation on Form I PB-1 and iPP fiber after manual insertion and annealing at 124 °C for 5 min, before crystallization.

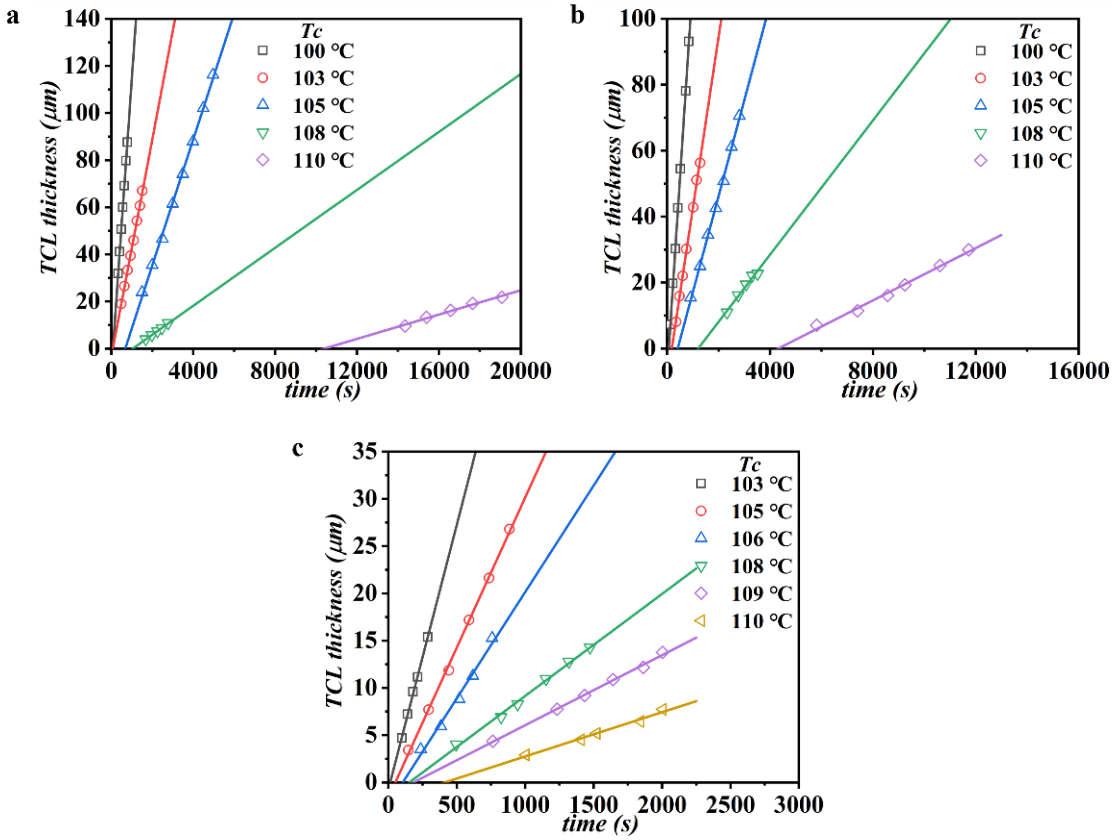

Figure A4 Thickness of the transcrystalline layer growing on Form I seeds with (a) spherulitic, (b) hedritic and (c) fibrous morphology, as a function of time during isothermal crystallization at various T_c.

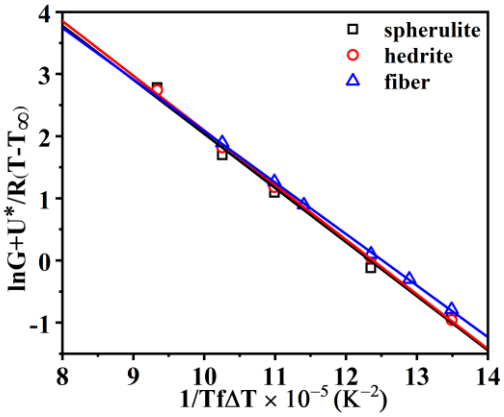

Figure A5 The plot of *lnG+U*/R(T-T∞)* versus *1/(TΔTf)* for crystallization on various substrates during isothermal crystallization after annealing at 124 °C.

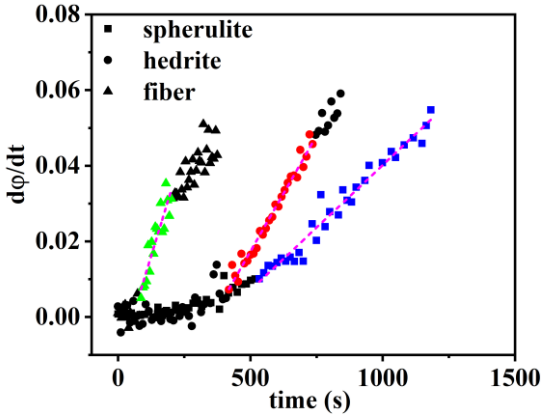

Figure A6 Time dependence of the rate of the light intensity evolution for crystallization on various substrates at 105 °C.

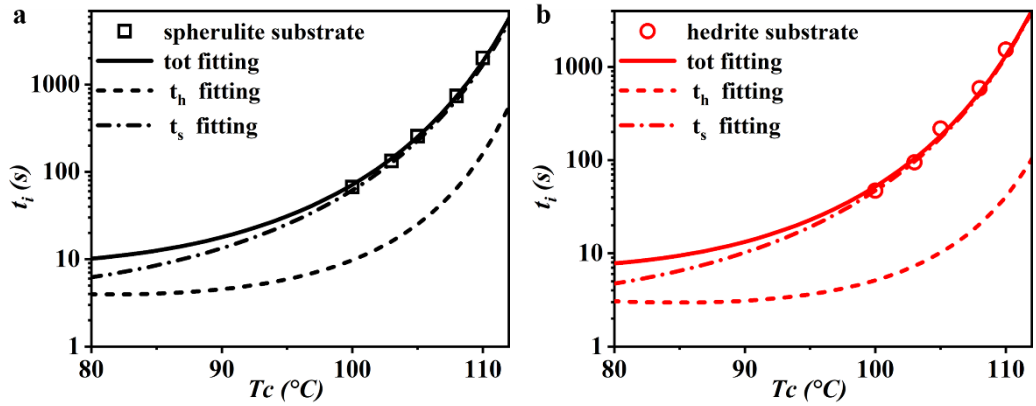

Figure A7 Induction time data of (a) spherulitic and (b) hedritic Form I substrates and corresponding fitting according to the detailed (total time) model. The dashed curves represent the contributions of the first and further layers formation (t_h and t_s models).

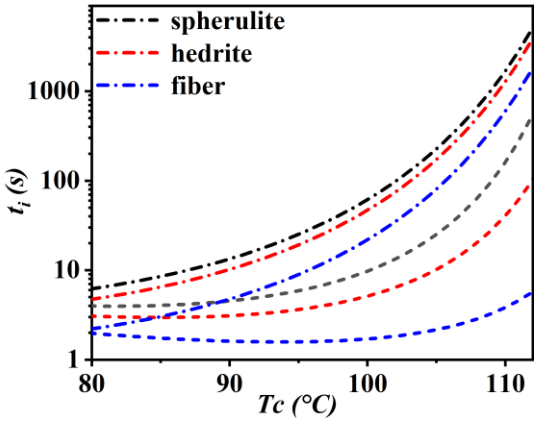

Figure A8 Plot of the fitting of first layer model (t_h) and further layer model (t_s) of the induction time for Form I substrates with varying morphology.

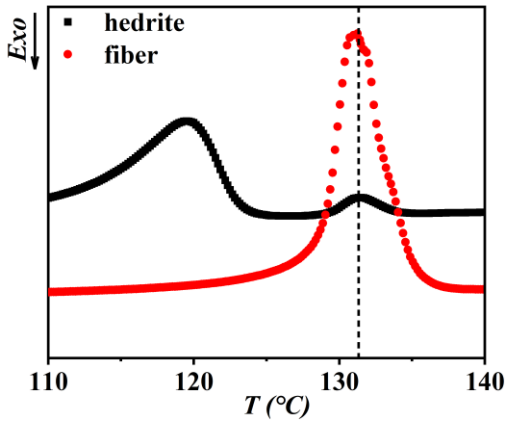

Figure A9 DSC first heating curves of hedrite and fiber after aging at room temperature for more than one month.

Appendix B

The following is the supplementary data to Chapter 5

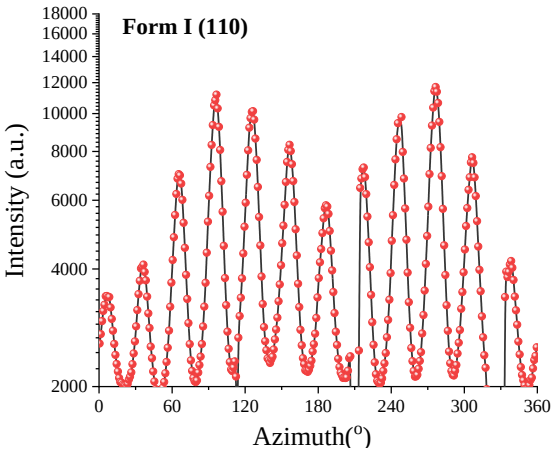

Figure B1. Azimuthal profile of the $(110)_I$ reflection of Form I of the accumulated pattern shown in Figure 5.2(a).

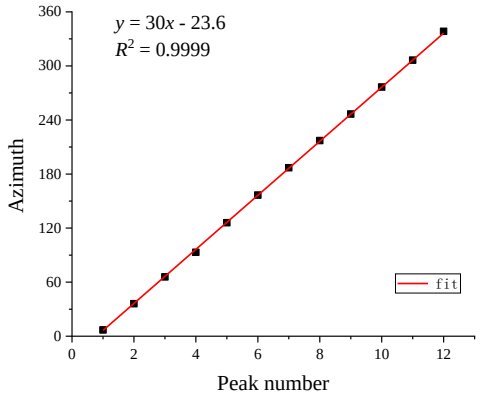

Figure B2. Plot and linear fit of maxima in azimuthal profile of the $(110)_I$ reflection of Form I as shown in Figure B1.

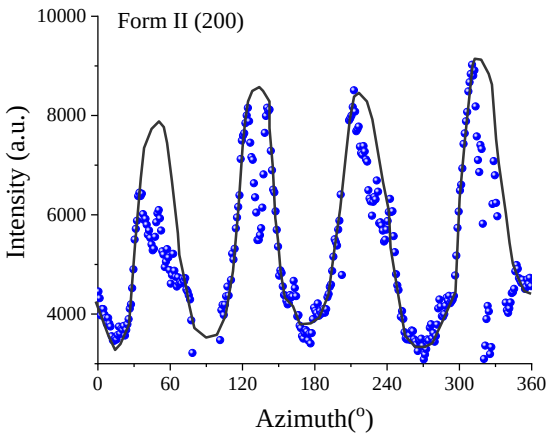

Figure B3 Azimuthal profile of the $(200)_{II}$ reflection of Form II of the accumulated pattern shown in Figure 5.2(a).

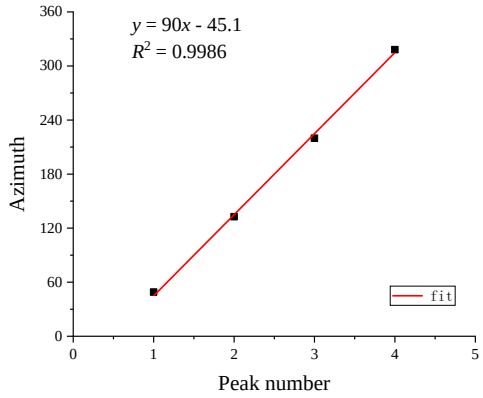

Figure B4 Plot and linear fit of maxima in azimuthal profile of the $(200)_{II}$ reflection of Form II as shown in Figure B3.

Appendix C

The following is the supplementary data to Chapter 6

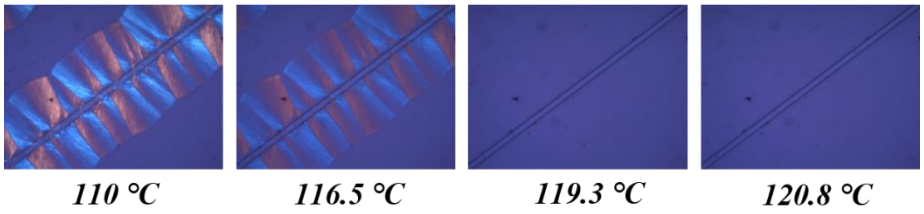

Figure C1 Polarized optical micrographs acquired during heating for PB-1 crystals formed on the surface of PP fiber at 91 °C.

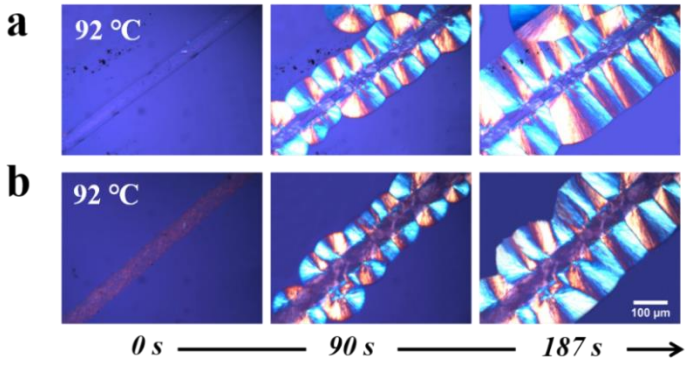

Figure C2 Polarized optical micrographs of PB-1 form II crystallized on the surface of (a) PLLA and (b) SC fibers during isothermal crystallization at 92 °C.

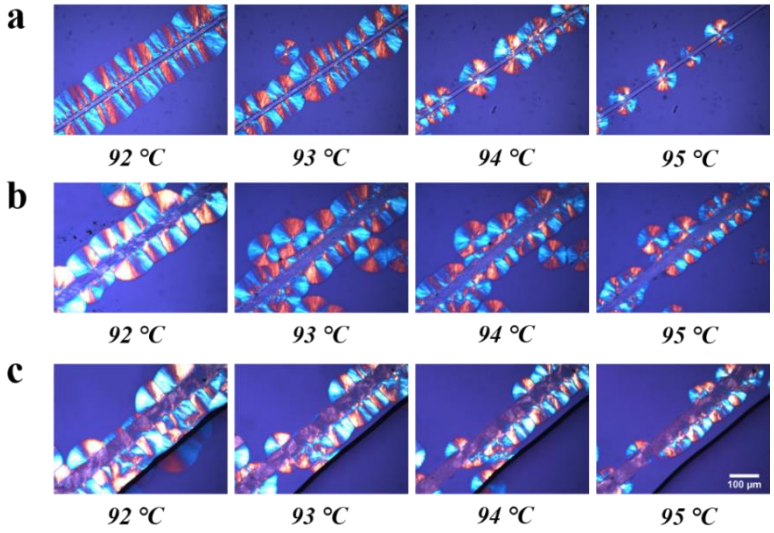

Figure C3 Morphological changes of PB-1 matrix crystallized on the surface of (a) PP, (b) PLLA and (c) SC fibers for 90 s at selected T_c values.

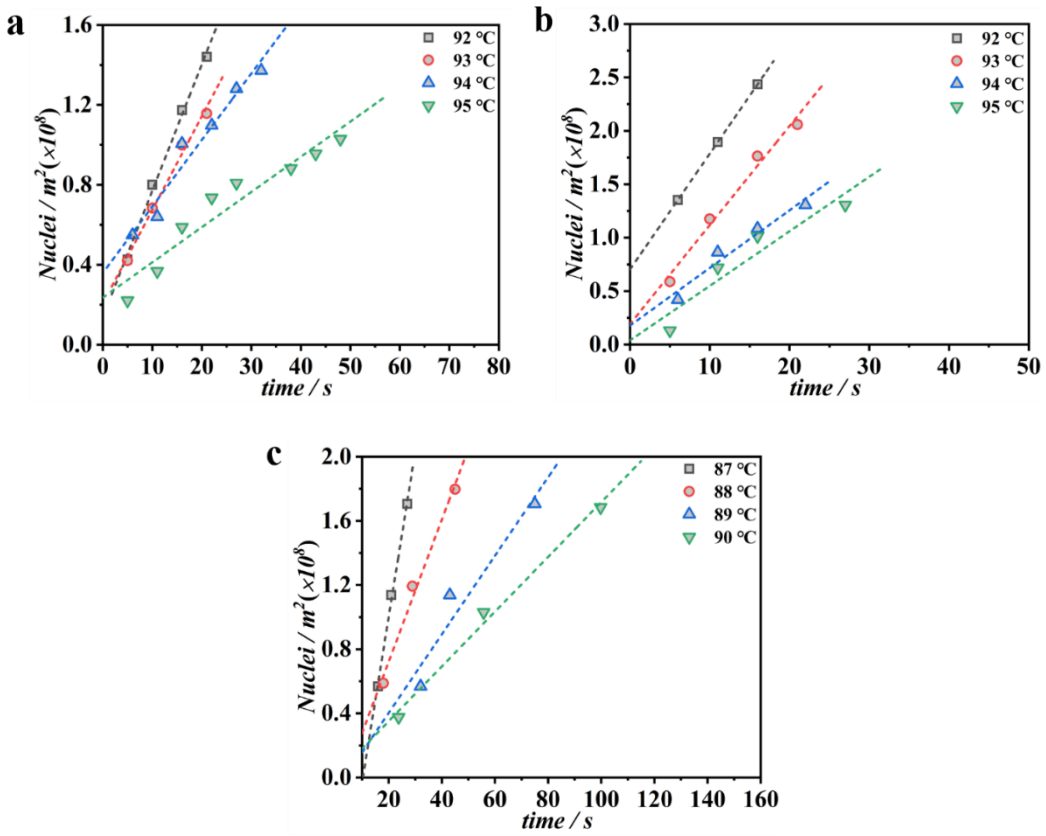

Figure C4 Nucleation density of PB-1 Form II on the surface of (a) SC, (b) glass and (c) carbon fibers as a function of time for specimens crystallized at selected T_c values.

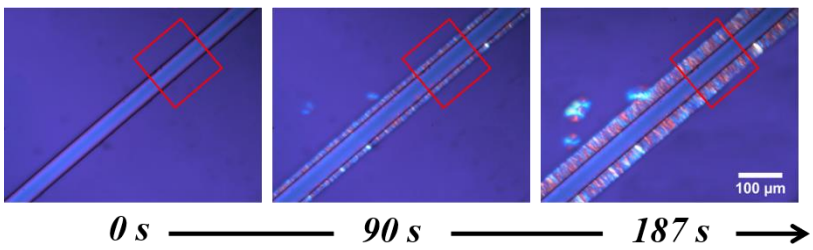

Figure C5 Polarized optical micrographs of PB-1 nucleated on the surface of the Form I fiber at different times during crystallization at 101 °C. The red rectangular region is the selected area for light intensity calculation.

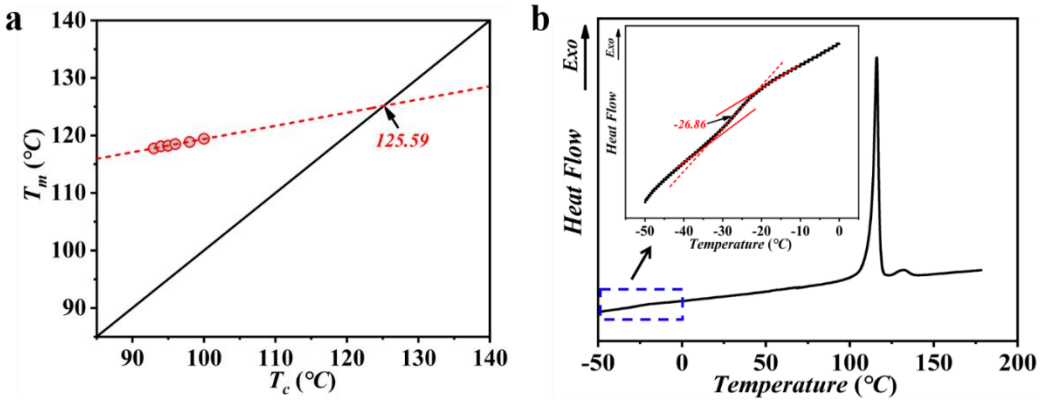

Figure C6 (a) Equilibrium melting point derived from the Hoffman-Weeks methods and (b) glass transition temperature of PB-1.

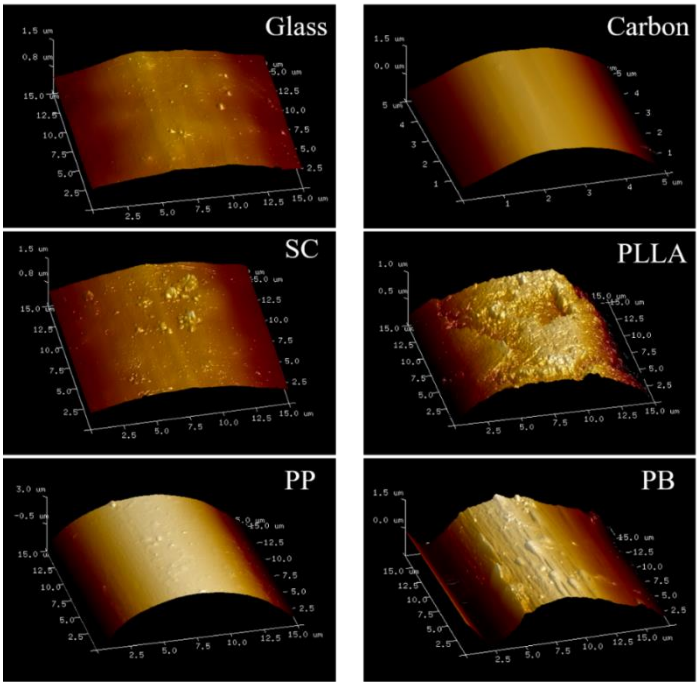

Figure C7 AFM height images of different fiber surfaces.

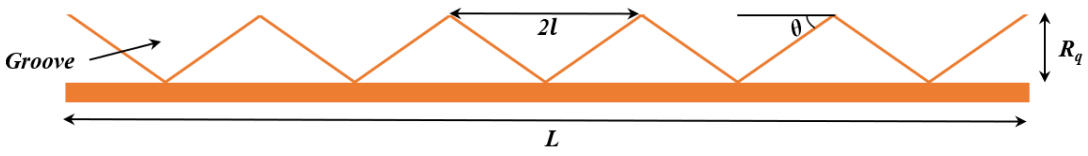

Figure C8 Schematic of parameters used for calculation of the number of the potential nucleation sites of fiber.

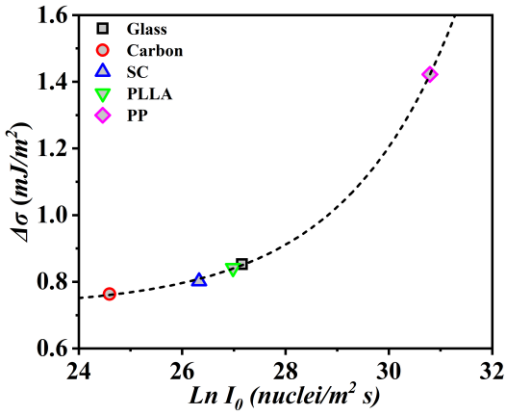

Figure C9 Plot of interfacial free energy difference ($\Delta\sigma$) as a function of the logarithm of potential nucleation sites ($Ln(I_0)$) for most fibers.

Appendix D

The following is the supplementary data to Chapter 7

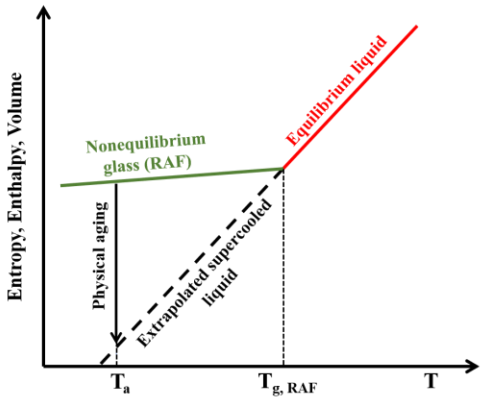

Figure D1 Schematic plot showing the thermodynamic conditions upon aging glassy RAF obtained when cooling from the equilibrium liquid.

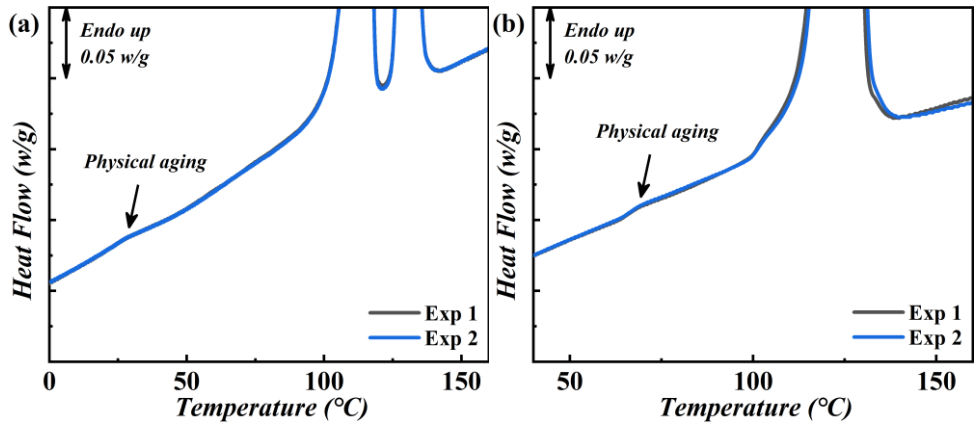

Figure D2 Enlarged heating scans after aging PB-1 at 10 °C for 300 min (Form II, a) and 60 °C for 30 min (Form I, b). Every experiment was repeated three times.

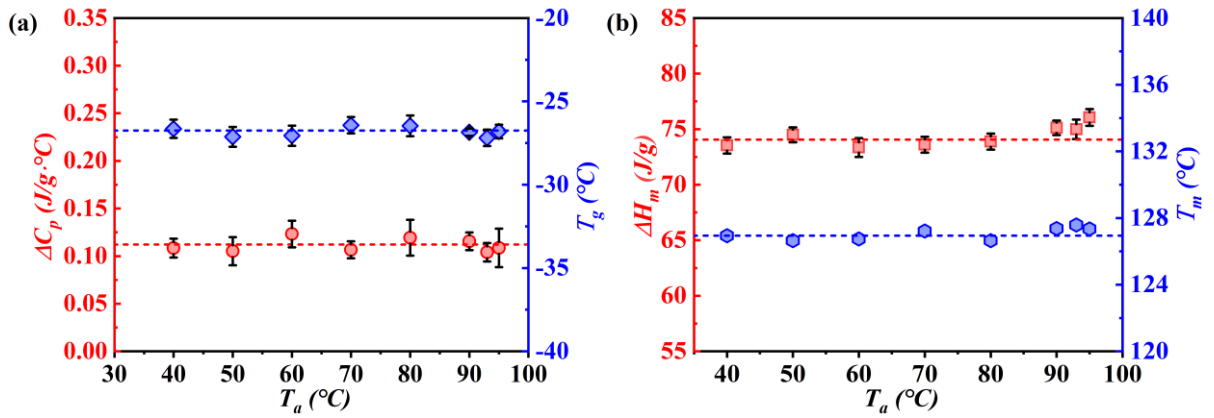

Figure D3 (a) Variation of specific heat-capacity (ΔC_p) and glass transition temperature (T_g) with annealing temperature. (b) Variation of crystals' melting enthalpy (ΔH_m) and melting temperature (T_m) with annealing temperature for PB-1 sample with Form I crystals. The red and blue dashed lines represent the corresponding properties of the unaged sample. Error bars indicate multiple evaluation on the same curve.

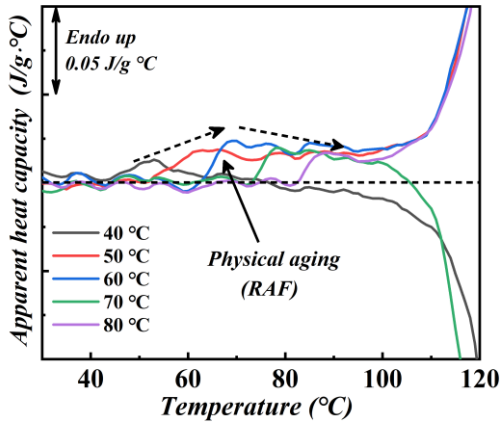

Figure D4 Heat capacity difference curves for PB-1 containing only Form I crystals annealed at indicated temperatures for 30 min.

Figure D4 shows selected difference curves of heat capacity after annealing at different temperatures based on the method of Figure 7.3. It can be appreciated that the excess enthalpy, i.e., the area of the annealing peak, goes through a maximum located at around 60 °C.

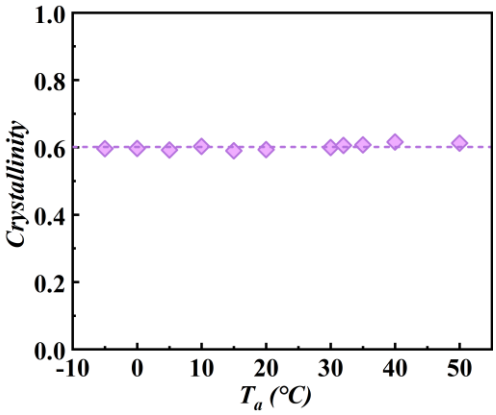

Figure D5 Variation of total crystallinity with annealing temperature for PB-1 with Form II crystals. The purple dashed line represents the corresponding crystallinity of the unaged sample.

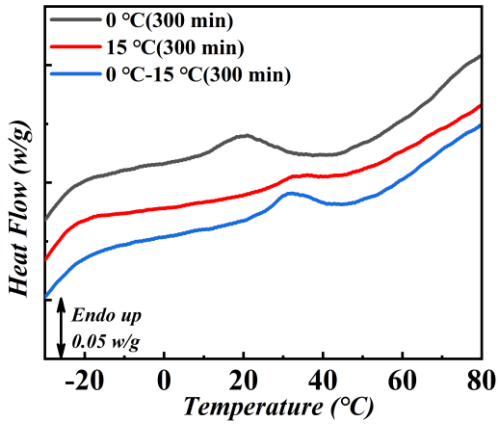

Figure D6 Enlarged heating scans after the indicated thermal protocols. The black and red solid lines represent the heat flow of Form II PB-1 after aging either at 0 °C or at 15 °C for 300 min, respectively. The blue line is the heat flow of aged Form II PB-1 with multistep aging experiments, i.e., a first aging step at 0 °C followed by aging at 15 °C, for 300 min.

To determine the origin of the enthalpy overshoot observed in Figure 7.6b, we considered a specific thermal protocol including a multistep aging experiment at different temperatures, which was recently proposed by Androsch and Schick[1] and implemented for the RAF by Monnier et al.[2] The heat flow rate scans after the indicated thermal protocols are shown in Figure D6. When the sample is submitted to multistep aging, just one endothermic peak is observed, which can be assigned to the influence of the annealing at 15 °C through comparison with the upper heat flow scan after aging at a single temperature. The drastic reduction of the characteristic peak aging at around 0 °C when a further aging is performed at 15 °C can hardly be ascribed to the melting of small crystallites, because the aging temperature (15 °C) is located

just in the low temperature tail of the endotherm. Therefore, we may conclude that it is the enthalpy relaxation of Form II RAF that is more likely to cause the endothermic peak.

References

[1] R. Androsch, K. Jariyavidyanont, C. Schick, Enthalpy relaxation of polyamide 11 of different morphology far below the glass transition temperature, Entropy 21(10) (2019) 984.

[2] X. Monnier, D. Cavallo, M.C. Righetti, M.L. Di Lorenzo, S. Marina, J. Martin, D. Cangialosi, Physical Aging and Glass Transition of the Rigid Amorphous Fraction in Poly (l-lactic acid), Macromolecules 53(20) (2020) 8741-8750.

Acknowledgments

I would like to offer my deepest gratitude to my supervisor, Prof. Dr. Dario Cavallo, for his continuous guidance, support and encouragement during my time as PhD student in his group at the University of Genova. I appreciate him for his interest in the subject and for the time he spent in correcting my articles and my thesis. His passion and dedication to research have continuously inspired me. I really appreciate his training during the past few years. I have learned a lot from him about how to become an excellent scientist, not only the professional knowledge, but also the attitude towards science.

I wish to thank Prof. Alejandro Müller, Prof. Dujin Wang, Prof. Xia Dong, Prof. Guoming Liu, Prof. Zhe Ma, Prof. Daniele Cangialosi, Prof. Maria Cristina Righetti, Prof Maria Laura Di Lorenzo and Prof. Martin Rosenthal for the wonderful collaboration and for the time they spent in correcting my articles.

I am grateful to Enrico Carmeli, Fenni Seif Eddine and Bao Wang for giving me warm experiences and kind helps. They made me feel like at home in the office. I also pass my sincere thanks to all of my colleagues at University of Genova who assisted me get through all these years: Andrea Costanzo, Magdalena Góra, Kasha, and Angelo Saperdi.

Thanks to the friends I have in Genova: Kun Li, Tao Li, Tianwen Qi, Lvye Lin, Jining Bao, Lianfeng Yang, and Dongxu Zhu, et al., It is very nice to meet you out of China. Thank you very much for the company and making my life wonderful.

I want to thank the China Scholarship Council (CSC) for the financial support during my doctoral research at the University of Genova.

Finally, I dedicate this thesis to my my parents. I would like to express my deepest appreciation to my family for their continuous support in my life.

Publications

This thesis has resulted in the following publications:

1. **Wei Wang,** Bao Wang, Agnieszka Tercjak, Alejandro J. Müller, Zhe Ma, Dario Cavallo, Origin of transcrystallinity and nucleation kinetics in polybutene-1/fiber composites, ***Macromolecules*** 53(20) (2020) 8940-8950.

2. **Wei Wang,** Bao Wang, Enrico Carmeli, Zefan Wang, Zhe Ma, Dario Cavallo, Cross-nucleation of polybutene-1 Form II on Form I seeds with different morphology, ***Polymer Crystallization*** 3(2) (2020) e210104.

3. **Wei Wang,** Seif Eddine Fenni, Zhe Ma, Maria Cristina Righetti, Daniele Cangialosi, Maria Laura Di Lorenzo, Dario Cavallo, Glass transition and aging of the rigid amorphous fraction in polymorphic poly(butene-1). ***Polymer*** (2021) 123830.

4. **Wei Wang,** Bao Wang, Stan F.S.P. Looijmans, Enrico Carmeli, Martin Rosenthal, Guoming Liu, Dario Cavallo, Epitaxy in polybutene-1 Form II-on-Form I cross-nucleation revealed by nanofocused X-ray diffraction on ad hoc morphology. ***Macromolecules*** 54(20) (2021) 9663-9669.

The author contributed to one publication outside the scope of this thesis:

1. **Wei Wang,** Angelo Saperdi, Andrea Dodero, Maila Castellano, Alejandro J. Müller, Xia Dong, Dujin Wang, Cavallo Dario, Crystallization of a self-assembling nucleator in poly(L-lactide) melt. ***Crystal Growth & Design*** 21(10) (2021) 5880–5888.